Institut für Kern- und Teilchenphysik
TU Dresden

Relative Luminosity Measurement of the LHC with ATLAS FCAL HV currents

von

Frank Seifert

2008

Institut für Kern- und Teilchenphysik
Fakultät Mathematik und Naturwissenschaften
Technische Universität Dresden

Relative Luminosity Measurement of the LHC with ATLAS FCAL HV currents

Diplomarbeit
zur Erlangung des akademischen Grades
Diplom-Physiker

vorgelegt von
Frank Seifert

Dresden 2008

Eingereicht am 26.08.2008

1. Gutachter: Prof. Dr. M. Kobel

2. Gutachter: Prof. Dr. K. Zuber

Abstract

The measurement of the luminosity is an important issue in every particle collider experiment. This thesis studies the possibility of a measurement of the relative luminosity of the new proton-proton collider, the LHC, for the ATLAS experiment. The measurement is based on the readout of the high voltage return current of the electromagnetic section of the forward calorimeter FCAL1 in ATLAS.
To investigate the proportionality between the FCAL1 HV currents and the luminosity of the LHC, the participation at testbeams with a small prototype of the FCAL1 and the analysis of the testbeam data is described. These testbeams took place at the U-70 proton accelerator in Protvino, Russia. During the testbeams it was possible to vary the beam intensity and to use this for a simulation of variable luminosities.
The result is that the FCAL1 HV current depends linearly on the beam luminosity and that this relative luminosity measurement is feasible in the ATLAS experiment with non-linearities less than 0.5 %, both from a systematic and a statistical point of view.

Kurzfassung

Die Messung der Luminosität ist eine wichtige Aufgabenstellung in jedem Experiment mit kollidierenden Teilchenstrahlen. Diese Arbeit studiert die Möglichkeit einer relativen Luminositätsmessung des neuen Proton-Proton Beschleunigers, dem LHC, für das ATLAS Experiment. Diese Messung basiert auf der Auslese von nachgelieferten Hochspannungsströmen in der elektromagnetischen Sektion des Vorwärtskalorimeters FCAL1 des ATLAS Detektors.
Zur Untersuchung der Proportionalität zwischen den HV-Strömen des FCAL1 und der Luminosität ist die Teilnahme an Teststrahl-Experimenten mit einem Prototypen des FCAL1 und die Analyse der Teststrahldaten beschrieben. Die Teststrahl-Experimente fanden am U-70 Protonenbeschleuniger in Protvino, Russland statt. Bei den Experimenten war es möglich die Strahlintensität zu variieren und das für eine Simulation variabler Luminositäten zu nutzen.
Das Ergebnis besteht darin, dass die FCAL1 HV-Ströme linear von der Strahl-Luminosität abhängen und dass diese Messung der relativen Luminosität im ATLAS Experiment mit Nichtlinearitäten unterhalb von 0.5 % möglich ist, sowohl vom systematischen als auch vom statistischen Standpunkt aus.

Contents

List of Figures

List of Tables

1 Introduction

A new particle collider, the Large Hadron Collider (LHC) at CERN[1], will have its first collisions with the so far highest center-of-mass energy at the end of 2008. It is a proton-proton collider with a nominal beam energy of 7 TeV per proton beam. This way the LHC experiments will be able to analyse unexplored conditions of matter as they existed in the very early universe. A lot of fundamental questions can be studied with the LHC like the search for Supersymmetry, the existence of extra dimensions or the examination of the Quantum Chromodynamics at high energy scales. But the best known challenge of the LHC is the discovery of the Higgs-Boson, the last undiscovered particle of the Standard Model of particle physics. The Standard Model predicts a scalar field which exists everywhere in the universe and is responsible for the masses of all fundamental particles interacting with it. If this theory is realised in nature, the LHC will be able to produce quanta of this Higgs-field, the Higgs-Bosons. The discovery of the Higgs-Bosons would be possible by measuring their decay products in the detectors of the LHC.

The measurement of the luminosity is important for every particle collider experiment. The knowledge of the absolute luminosity is necessary mainly for measuring cross sections which is important to identify a signal of new physics or the type of the discovery. A relative luminosity measurement is important for an online information for the accelerator control room on the one hand and for an offline analysis for a precise study of systematic uncertainties like trigger efficiencies, reconstruction efficiencies and mis-tag rates on the other hand. In electron-positron colliders like LEP[2] or PEP[3] the luminosity could be measured very precisely via elastic electron-positron scattering processes. These so called Bhabha events are theoretical well understood and by measuring their rate the absolute luminosity of the collider could be inferred with a precision of better than 1 %.
At hadron colliders like the LHC no single process exists that would allow for the determination of the absolute luminosity over the full range of relevant luminosities .
This thesis describes the possibility of a measurement of the relative luminosity of the LHC for the ATLAS detector. This measurement is based on a readout of the high voltage return current in the forward section of the liquid argon calorimeter of ATLAS. Therefore, the electromagnetic section of the forward calorimeter FCAL is considered. The measured relative luminosity has to be calibrated to absolute values with a different luminosity monitor.

Since no measurements with colliding beams have been done at the LHC so far, the feasibility of this luminosity measuring method was verified in a testbeam. The participation

[1] Conseil Européen pour la Recherche Nucléaire
[2] The Large Electron Positron collider was in operation until 2000.
[3] An asymmetric $e^+ - e^-$ collider in Stanford, USA.

at this testbeam at the U-70 proton accelerator with a small prototype of the FCAL in Protvino, Russia is described in this thesis. The analysis of the data taken during the testbeam is explained and its results are discussed.

This thesis is structured as follows: In Chapter 2 an overview over the Standard Model of particle physics is given. The LHC, its beam parameters and the ATLAS experiment are described in Chapters 3 and 4. The configuration of the forward calorimter FCAL of ATLAS and its electromagnetic section, the FCAL1, are explained in more detail. Furthermore, the other luminosity monitors of the ATLAS detector are described in Chapter 4 and the advantages and disadvantages of the luminosity measuring method using the FCAL1 high voltage currents are explained in Chapter 5. In addition, the high voltage supply structure of the FCAL1 in ATLAS is described.
Chapter 6 describes the small prototype of the FCAL1, the testbeam in Protvino and the data taking there. The analysis of the testbeam data and its results are explained in Chapter 7. Some differences between the ATLAS FCAL1 and the FCAL1 prototype, the so called FCALchick, used in the Protvino testbeam are considered in the Chapters 6 and 8. The comparabilty between the results of the testbeam and the measurement in ATLAS is discussed in Chapter 8. Finally, a conclusion is given and the already implemented readout of the FCAL1 HV currents of all HV channels in ATLAS is described in Chapter 9.

2 The Standard Model

2.1 Overview

The best theory, we presently have for describing elementary particles and their interactions is the Standard Model of particle physics.
The Standard Model includes the three known families of quarks, the three known families of leptons (see Table 2.1) and the three forces including their force carriers, the so called gauge bosons. These are the electromagnetic force, the weak interaction and the strong force.

Family	Leptons	Quarks
1st	ν_e e	u d
2nd	ν_μ μ	c s
3rd	ν_τ τ	t b

Table 2.1: *Particle families.*

Quarks and leptons are fermions with spin $\frac{1}{2}$ and the gauge bosons have spin 1. Ordinary matter only consists of particles of the first family. The protons and neutrons forming atomic nuclei are composed of u- and d-quarks and are surrounded by electrons. Particles of the second and third family dacay into particles of the first generation within fractions of a second. Today these particles can only be produced by cosmic radiation or in particle accelerators.
The Standard Model is constructed as a local quantum field theory and can describe all known particles and their interactions with the exception of gravitation. For including gravitation into a unifying theory it is necessary to develop a quantum theory of gravitation, which has not yet been done in a consistent way. Until today the Standard Model only combines quantum mechanics with special relativity.
The best known force is the electromagnetic force, which is responsible for our view of the macroscopic world. The force carrier or gauge boson of electromagnetism is the massless photon coupling to the electric charge.
Radioactivity and particle decays can be caused by the weak interaction with its heavy W^+, W^- and Z^0 gauge bosons. They are very massive, which is the reason for the very low range of the weak force of about 10^{-18} m in contrast to the infinite range of the electromagnetic force. An unique attribute of the weak interaction is the violation of parity. An observable that changes its sign with space inversion is the helicity

$$h = \frac{\vec{s} \cdot \vec{p}}{|\vec{s}| \cdot |\vec{p}|}, \tag{2.1}$$

which is a product of an axialvector (spin) and a vector (momentum). An interaction depending on helicity is not invariant under parity transformation. Generally, an interaction described by a spin 1 particle can have vectorial or axialvectorial character.
The electromagnetic interaction is purely vectorial and therefore it conserves parity. The weak force is a vector minus axialvector interaction and therefore only couples to left chiral fermions and right chiral antifermions, which corresponds to maximum violation of parity. The charge of the weak interaction is the weak isospin I^W. But in nature the electromagnetic and weak interaction are combined to the electroweak interaction and the electrical charge and the weak charge are related by the Gell-Mann-Nishijima relation

$$I_3 = Q - \frac{Y}{2}, \tag{2.2}$$

with Y being the weak hypercharge.
Neutrinos have a very small mass and participate only in weak interactions. The other leptons e, μ and τ carry electric charge in addition (see Table 2.2).
The same applies to quarks, but in addition they carry strong color charge and interact via the strong force. The theory describes this third force as quantum chromodynamics (QCD), because its charges exist in three different types, the so called color charges red, green and blue. They have the special property, that adding all three colors together gives 0.

Particles			Q	I^W	I_3^W	Y	color charge	spin
$\begin{pmatrix} u_L \\ d_L \end{pmatrix}$	$\begin{pmatrix} c_L \\ s_L \end{pmatrix}$	$\begin{pmatrix} t_L \\ b_L \end{pmatrix}$	$+2/3$ $-1/3$	$1/2$ $1/2$	$+1/2$ $-1/2$	$+1/3$ $+1/3$	r, g, b r, g, b	$1/2$ $1/2$
$\begin{pmatrix} \nu_{eL} \\ e_L \end{pmatrix}$	$\begin{pmatrix} \nu_{\mu L} \\ \mu_L \end{pmatrix}$	$\begin{pmatrix} \nu_{\tau L} \\ \tau_L \end{pmatrix}$	0 -1	$1/2$ $1/2$	$+1/2$ $-1/2$	-1 -1	0 0	$1/2$ $1/2$
u_R	c_R	t_R	$+2/3$	0	0	$+4/3$	r, g, b	$1/2$
d_R	s_R	b_R	$-1/3$	0	0	$-2/3$	r, g, b	$1/2$
e_R	μ_R	τ_R	-1	0	0	-2	0	$1/2$
ν_{eR}	$\nu_{\mu R}$	$\nu_{\tau R}$	0	0	0	0	0	$1/2$
		γ	0	0	0	0	0	1
		g	0	0	0	0	8 different	1
		W^+	$+1$	1	$+1$	0	0	1
		W^-	-1	1	-1	0	0	1
		Z^0	0	1	0	0	0	1
		H^0	0	$1/2$	$-1/2$	1	0	0

Table 2.2: *Particles and quantum numbers. In addition for each quark and lepton an anti particle with opposite charge exist. The Higgs-Boson given in the last row is a scalar and responsible for the high mass of the gauge bosons W^+, W^- and Z^0. The eight different color charges of the gluon are combinations of the strong colors r, g, b and their anti colors $\bar{r}$, $\bar{g}$, $\bar{b}$.*

Here the force carrier is the gluon which is massless like the photon.
Nonetheless, the strong force only has a range of 10^{-15} m, because in contrast to the photon

the gluon carries color charge itself and therefore interacts with other gluons. This leads to a peculiarity of QCD, called confinement, which means that a color charged particle can never exist as a free particle. It is always bound within a color neutral meson or baryon consisting of multiple quarks and gluons. The color of the gluons is not one of the three possible quark colors but a combination of them and their anti colors.
The more massive quarks of the second and the third generation decay thtough weak interaction into quarks of the first generation. The reason for this is, that mass eigenstates of all physical quarks are a combination of the electroweak flavor eigenstates.
But it is possible to produce the quarks and leptons of the second and third generation, as well as the gauge bosons, in particle collider experiments and to measure their decays.

2.2 Gauge Theories

A very successful way to formulate a theory is to do this as a gauge theory. Quantum electrodynamic (QED) is a gauge theory verified very precisely by experiments.
The principle of least action is a fundamental principle of nature and leads to the Dirac Lagrangian of a free particle with mass m

$$\mathcal{L}_D = \bar{\psi}(i\gamma_\mu \partial^\mu - m)\psi \tag{2.3}$$

with $\psi(\vec{r}, t)$ being the wave function of a relativistic particle with mass m and charge q like the electron. The wave function

$$\psi(\vec{r}, t) \rightarrow \psi'(\vec{r}, t) = e^{iq\chi}\psi(\vec{r}, t) \tag{2.4}$$

(χ=const.) also describes the physical system because ψ itself is not a physical observable, but only its absolute square $|\psi|^2$. This transformation is called a global gauge transformation (identical at each space-time point) and is connected to the conservation of the electric charge. The Lagrangian (2.3) is invariant under a global gauge transformation. It is now possible to expand this to a local gauge transformation (not identical at different space-time points):

$$\psi(\vec{r}, t) \rightarrow \psi'(\vec{r}, t) = e^{iq\chi(\vec{r},t)}\psi(\vec{r}, t) \tag{2.5}$$

with arbitrary space-time dependence $\chi(\vec{r}, t)$. The Lagrangian (2.3) is not invariant under a local gauge transformation:

$$\begin{aligned} \mathcal{L}_D{}' &= \bar{\psi}'(i\gamma_\mu \partial^\mu - m)\psi' = e^{-iq\chi(\vec{r},t)}\bar{\psi}(\vec{r}, t)(i\gamma_\mu \partial^\mu - m)e^{iq\chi(\vec{r},t)}\psi(\vec{r}, t) \\ &= e^{-iq\chi(\vec{r},t)}\bar{\psi}(\vec{r}, t)(i\gamma_\mu \partial^\mu [e^{iq\chi(\vec{r},t)}])\psi(\vec{r}, t) + \bar{\psi}(i\gamma_\mu \partial^\mu - m)\psi \neq \mathcal{L}_D. \end{aligned} \tag{2.6}$$

The basic principle of a local gauge theory is to restore the gauge invariance. This is done by introducing a new field A^μ with the following transformation behavior:

$$A^\mu(\vec{r}, t) \rightarrow A'^\mu(\vec{r}, t) = A^\mu(\vec{r}, t) - \partial^\mu \chi(\vec{r}, t). \tag{2.7}$$

and by replacing the normal derivative by the covariant derivative:

$$D^\mu = \partial^\mu + iqA^\mu(\vec{r}, t). \tag{2.8}$$

The field A^μ can be identified with the photon. The new lagrangian

$$\mathcal{L}_D = \bar{\psi}(i\gamma_\mu D^\mu - m)\psi \tag{2.9}$$

is invariant under local gauge transformations, when applying simultaneously to (2.5), the gauge transformation of the field (2.7):

$$\begin{aligned} \mathcal{L}_D{}' &= \bar{\psi}'(i\gamma_\mu D^{\mu'} - m)\psi' = e^{-iq\chi}\bar{\psi}[i\gamma_\mu(\partial^\mu + iqA^{\mu'}) - m]e^{iq\chi}\psi \\ &= e^{-iq\chi}\bar{\psi}e^{iq\chi}(i\gamma_\mu\partial^\mu\psi) + e^{-iq\chi}\bar{\psi}[i\gamma_\mu\partial^\mu e^{iq\chi}]\psi - e^{-iq\chi}\bar{\psi}[\gamma_\mu q(A^\mu - \partial^\mu\chi) + m]e^{iq\chi}\psi \end{aligned} \tag{2.10}$$

The second term yields $-e^{-iq\chi}\bar{\psi}\gamma_\mu q(\partial^\mu\chi)e^{iq\chi}\psi$ and compensates the corresponding part in the third term and it follows

$$e^{-iq\chi}\bar{\psi}e^{iq\chi}(i\gamma_\mu[\partial^\mu + iqA^\mu] - m)\psi = e^{-iq\chi}\bar{\psi}e^{iq\chi}(i\gamma_\mu D^\mu - m)\psi \tag{2.11}$$

and with that

$$\mathcal{L}_D = \bar{\psi}(i\gamma_\mu D^\mu - m)\psi = \bar{\psi}'(i\gamma_\mu D'^\mu - m)\psi' = \mathcal{L}_D{}'. \tag{2.12}$$

The phase transformed wave function ψ' is physically identical to ψ, because the local gauge transformation of the wave function 2.5 is compensated by the gauge transformation 2.7 of the field A^μ. The requirement of local gauge invariance forces the introduction of a new field that couples to the fermion field with a strenght proportional to the fermions electric charge.
In addition the field A^μ has to be gauge invariant itself. The Maxwell-equations for the field A^μ are

$$\partial_\mu F^{\mu\nu} = j^\nu, \tag{2.13}$$

where j^ν is the gauge current and with

$$F^{\mu\nu} = \partial^\mu A^\nu - \partial^\nu A^\mu \tag{2.14}$$

follows

$$\partial_\mu\partial^\mu A^\nu - \partial_\mu\partial^\nu A^\mu = j^\nu \tag{2.15}$$

or

$$\Box A^\nu - \partial^\nu(\partial_\mu A^\mu) = j^\nu. \tag{2.16}$$

This Maxwell-equations do not change under the gauge transformation (2.7):

$$\begin{aligned} \Box A'^\nu - \partial^\nu(\partial_\mu A'^\mu) &= \Box(A^\nu - \partial^\nu\chi) - \partial^\nu(\partial_\mu[A^\mu - \partial^\mu\chi]) \\ &= \Box A^\nu - \partial^\nu(\partial_\mu A^\mu) - \Box\partial^\nu\chi + \partial^\nu(\partial_\mu\partial^\mu\chi) \\ &= \Box A^\nu - \partial^\nu(\partial_\mu A^\mu) = j^\nu. \end{aligned} \tag{2.17}$$

So $A^{\nu'}$ is the electromagnetic field, too. Choosing the Lorentz-gauge $\partial_\mu A^\mu = 0$ the Maxwell-equations simplifies to

$$\Box A^\nu = j^\nu. \tag{2.18}$$

In a local gauge theory like QED it is possible to compensate a local gauge transformation (2.5) by a gauge transformation (2.7). The fields are thereby gauge invariant.

2.3 Gauge Invariance in the Electroweak Interaction

It is known from experiment that the gauge bosons of the weak interaction the $W^\pm$- and Z^0 bosons are massive. Due to the fact that QED is a gauge theory verified very precisely by experiment, one tries to formulate the weak interaction as a gauge theory as well.
With a massive gauge boson of mass M the Maxwell equations (2.16) get an additional mass term:

$$(\Box + M^2)A^\nu - \partial^\nu(\partial_\mu A^\mu) = j^\nu. \tag{2.19}$$

With the Lorentz gauge and a free field ($j^\nu = 0$) the Proca equation for a heavy boson follows:

$$(\Box + M^2)A^\nu = 0. \tag{2.20}$$

But with $M \neq 0$ the Proca equation (2.19) is not gauge invariant under the gauge transformation 2.7:

$$\Box A^{\nu'} - \partial^\nu(\partial_\mu A^{\mu'}) + M^2 A^{\nu'} = \Box A^\nu - \partial^\nu(\partial_\mu A^\mu) + M^2 A^\nu - M^2\partial^\nu\chi = j^\nu - M^2\partial^\nu\chi \neq j^\nu, \tag{2.21}$$

because the last term does not disappear in case of $M^2 \neq 0$. That means the Proca equation (2.19) in Lorentz-gauge

$$\Box A^\nu + M^2 A^\nu = j^\nu \tag{2.22}$$

is not compatible with Equation (2.18), except if the right hand side includes a current of the form $M^2 A^\nu$ that is switched on automatically with the field A^μ. In experiments it was possible to give an upper limit on the mass of the photon of $M_\gamma < 6 \cdot 10^{-16}$ eV [12]. For this reason it is assumed that the photon is in fact massless and the gauge theory QED is realised in nature.
The theory of weak interaction is described via a SU(2) gauge group leading to global phase transformation.

$$\psi' = U\psi = e^{ig\vec{\chi}\cdot\frac{\vec{\tau}}{2}}\psi. \tag{2.23}$$

Here $\vec{I} = \vec{\tau}/2$ are the generators of SU(2) and $\vec{\tau}$ can be represented the Pauli matrices. The unitary SU(2)-operation U is a rotation around the direction $\vec{\chi}$ with angle $|\vec{\chi}|$ in isospin space. Generalising this to a local phase transformation leads to:

$$\psi' = e^{ig\vec{\chi}(\vec{r},t)\cdot\frac{\vec{\tau}}{2}}\psi. \tag{2.24}$$

Here ψ and ψ' are doublets of left chiral quarks and leptons and g is the coupling constant of the weak interaction. In contrast to the case of QED, $\vec{\tau}$ is not a scalar, but a vector with 3 components and 3 fields W_1^μ, W_2^μ and W_3^μ instead of one field are needed. With that the covariant derivative is:

$$D^\mu = \partial^\mu + ig\frac{\vec{\tau}}{2}\cdot\vec{W}^\mu. \tag{2.25}$$

The gauge fields are closely connected to the $W^\pm$- and Z^0 bosons and transform accordingly to

$$\vec{W}^\mu \rightarrow \vec{W}^{\mu'} = \vec{W}^\mu - \partial^\mu\vec{\chi} - g(\vec{\chi}\times\vec{W}^\mu). \tag{2.26}$$

These field transformations have the same form as those for QED as in Equation (2.7), with the addition of the cross product. This term is necessary, because the three generators of the SU(2) group $\vec{\tau} = (\tau_1, \tau_2, \tau_3)$ do not commute. That means this is in contrast to QED, a non-abelian gauge theory. This leads to interactions between the gauge bosons themselves. With the gauge fields for the weak interaction one can write down the Maxwell-equations for massless fields in analogy to QED:

$$\Box\vec{W}^\mu - \partial^\mu(\partial_\nu\vec{W}^\nu) = \vec{j}^\mu. \tag{2.27}$$

Now for massive fields a model is needed to generate terms in the three currents $\vec{j}^\mu$=$(j_1^\mu, j_2^\mu, j_3^\mu)$ of the type $-M^2\vec{W}^\mu$. Thus, the Proca equation for massive spin-1 bosons would result.
The strong interaction (QCD) is a non-abelian gauge theory as well. It is designed as a SU(3) group with eight generators and eight gauge fields, the 8 massless gluons.

2.4 The Higgs Theory

The Higgs theory [15, 16] (by Peter Higgs) predicts a scalar (spin 0), electrical neutral field φ with weak isospin $I^W = 1/2$. This field causes currents of the form $\vec{j}^{\mu}(\varphi)$ to act as mass terms in (2.27):

$$\Box \vec{W}^{\mu} - \partial^{\mu}(\partial_{\nu}\vec{W}^{\nu}) = \vec{j}^{\mu}(W) + \vec{j}^{\mu}(\varphi). \tag{2.28}$$

Assuming $|\varphi| = \text{constant}$, φ can be written as:

$$\varphi(\vec{r},t) = \frac{1}{\sqrt{2}}\begin{pmatrix}\varphi_1(\vec{r},t) + i\varphi_2(\vec{r},t)\\ \varphi_3(\vec{r},t) + i\varphi_4(\vec{r},t)\end{pmatrix} = e^{i\frac{\vec{\tau}}{2}\cdot\vec{\theta}(\vec{r},t)}\begin{pmatrix}0\\ v + h(\vec{r},t)\end{pmatrix} \tag{2.29}$$

with $v = \text{constant}$ and real being the vacuum expectation value and $h(\vec{r},t)$ the Higgs-field. The isospinor on the right side corresponds to a scalar field with $I_3 = -1/2$. With this Higgs-field it is possible to include the following currents by using the covariant derivative (Equation (2.25)):

$$\vec{j}^{\mu}(\varphi) = ig(\varphi^{\dagger}\frac{\vec{\tau}}{2}[D^{\mu}\varphi] - [D^{\mu}\varphi]^{\dagger}\frac{\vec{\tau}}{2}\varphi). \tag{2.30}$$

With this Klein-Gordon-currents for a spin 0 Higgs-Boson the field equations (2.28) are gauge invariant. Now choosing the gauge transformation in Equation (2.29) to have $\varphi_1 = \varphi_2 = \varphi_4 = 0$ (unitary gauge) leads to $\varphi_3 = v$ for the Higgs field (the other three degrees of freedom are then absorbed by the 3 other massive gauge fields).
Therefore the Lagrangian for the Higgs field can be written as:

$$\mathcal{L} = T - V = (\partial_{\mu}\varphi)^{\dagger}(\partial^{\mu}\varphi) - \mu^2(\varphi^{\dagger}\varphi) - \lambda(\varphi^{\dagger}\varphi)^2, \tag{2.31}$$

in which the potential V contains a mass term $\mu^2\varphi^{\dagger}\varphi$ and a term $\lambda(\varphi^{\dagger}\varphi)$ describing the selfcoupling of the Higgs field with strength λ. With $\lambda > 0$ and $\mu^2 < 0$ the potential V takes the form shown in Figure 2.1, if μ and λ are constant.
With the choice $\varphi_3 = v$, the minimum of the potential is:

$$\frac{\partial V}{\partial \varphi} = \mu^2 + 2\lambda\varphi_3 = 0 \rightarrow {\varphi_3}^2 = -\frac{\mu^2}{2\lambda} \equiv v^2. \tag{2.32}$$

The potential itself is symmetrical around 0, but its minimum is not at $\varphi = 0$. That means a vacuum state $\neq 0$ is realised and the local gauge symmetry is spontaneously broken, where v is called the vacuum expectation value. It is connected to the experimentally measured Fermi-constant G_F by

$$v^2 = \frac{\sqrt{2}}{2G_F} \tag{2.33}$$

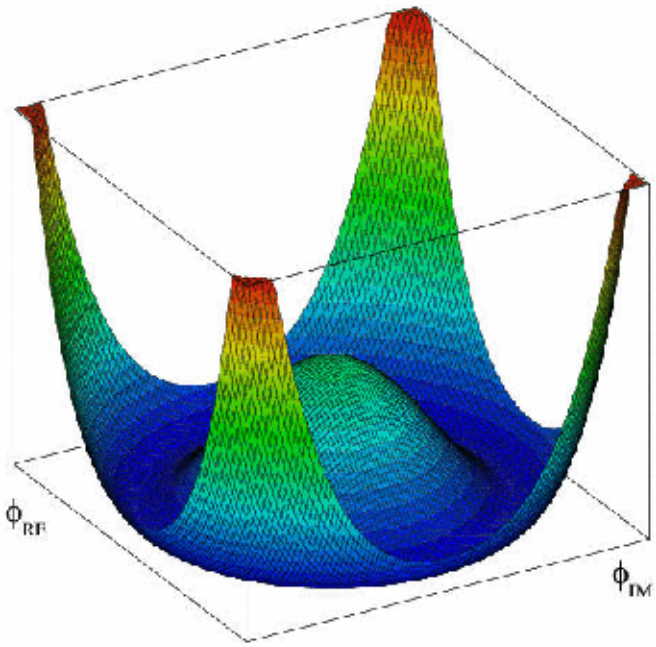

Figure 2.1: *The Higgs potential depending on the real- and imaginary part of φ [2].*

and calculated to $v = 246$ GeV.
It is possible to test this theory and the existence of the Higgs field by producing a quantum of this field, the Higgs-Boson, in a particle collider experiment and by measuring its decay. With that one can measure the mass of the Higgs-Boson (after symmetry breaking) $M_H = \sqrt{-2 \cdot \mu^2}$ and with Equation (2.32) the parameter λ would also be known.
The experiments performed at the Large Electron Positron Collider LEP were able to exclude a Standard Model Higgs-Boson with mass $M_H < 114$ GeV at 95% confidence level [4]. In addition it is observed that in the case of $W^{\pm}$-scattering the theory is consistent only up to a mass of approximately 1 TeV of the Higgs-Boson [18].
To observe a Standard Model Higgs boson with mass above 114 GeV up to 1 TeV, a new proton collider with the highest center of mass energy achieved so far, the Large-Hadron-Collider (LHC), was planned and constructed to have its first collisions this year.

2.5 Importance of Luminosity Measurements

The Standard Model is surveyed and confirmed very successfully by experiment to date. For example the masses of the $W^{\pm}$- and Z^0-Bosons were measured very precisely in the LEP (Large Electron Positron Collider) experiments: $M_{W^{\pm}} = (80.425 \pm 0.038)$ GeV [14] and $M_{Z^0} = (91.1875 \pm 0.0021)$ GeV [14]. In addition the line shape of the Z^0-Boson was measured for example for the reaction channel [8]

$$e^+e^- \longrightarrow Z^0 \longrightarrow q\bar{q}. \tag{2.34}$$

By comparing this measurement with theory predictions for the sum of the neutrino cross sections $\sigma(e^+e^- \longrightarrow Z^0 \rightarrow \nu_e\bar{\nu}_e) + \sigma(e^+e^- \longrightarrow Z^0 \rightarrow \nu_\mu\bar{\nu}_\mu) + \sigma(e^+e^- \longrightarrow Z^0 \rightarrow \nu_\tau\bar{\nu}_\tau)$ (missing cross section in the experiment) for a different number of neutrino generations, it

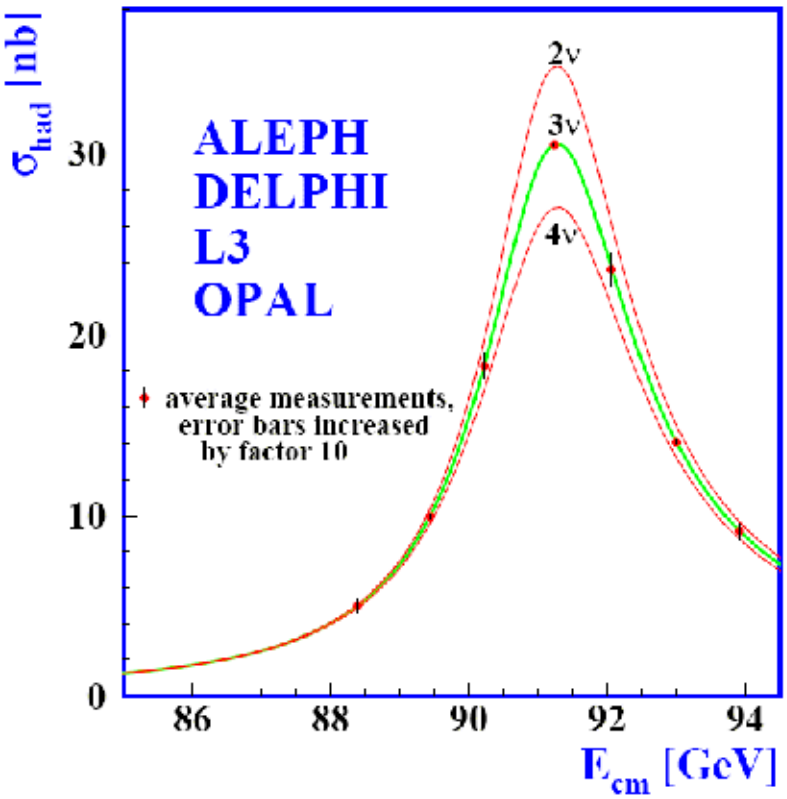

Figure 2.2: *Cross section of the reaction $e^+e^- \longrightarrow Z^0 \longrightarrow q\bar{q}$ as a function of the center of mass energy. The theoretical predictions for two, three and four neutrino generations are plotted [13].*

is possible to measure the number of neutrino generations. The result is shown in Figure 2.2 and it can be seen that the experimental data confirmes exactly with the theoretical line shape of three neutrino generations (the mass of a fourth neutrino has to be larger than half the Z^0-mass). The conclusion is that there are only three generations of particles in general, assuming only neutrinos with less than half the Z^0-mass [7].
These measurements were only possible with a precise measurement of the luminosity, because the cross section can be calculated from the measured reaction rates only by the knowledge of the luminosity. The same way, by comparing the partial decay widths of the Z^0 into quarks and into leptons it was possible to confirm the existence of exactly three different strong color charges in QCD. For this, only the knowledge of relative cross sections and with it relative luminosities was necessary.
The LEP experiments were able to measure the luminosity with a precision of 0.05 % using small-angle elastic $e^+ - e^-$ (Bhabha) scattering.
In high energy physics, the cross section is an important variable for comparing a theoretical prediction with the experiment. For example a measurement of coupling constants of the forces is possible only by measuring cross sections of particle reactions. And generally, always when one want to measure cross sections in a particle accelerator experiment, a luminosity measurement is fundamental.

3 The Large Hadron Collider

3.1 Beam Energy

Inside the tunnel of the dismantled LEP at CERN (Conseil Européen pour la Recherche Nucléaire) near Geneva, Switzerland, the Large Hadron Collider LHC is currently being installed. The tunnel has a circumference of about 27 km and thus allowing LEP to accelerate electrons up to an energy of 103 GeV per beam. In the LEP the maximum beam energy was limited by synchrotron radiation, because of the low mass of electrons and positrons. For the energy loss per circulation holds

$$E_{lost} \propto \frac{1}{r}\frac{E^4}{m^4}, \tag{3.1}$$

with r beeing the mean bending radius of the accelerator, E the energy and m the mass of the particle. Thus, the cavities of the LEP had to refeed more than 1.7 GeV to the beam per circulation.
Synchrotron radiation losses do not limit the beam energy for proton accelerators and colliders because of its 1800 times higher mass. The beam energy of the LHC will be limited by the magnetic field of the dipole magnets keeping the protons in the circular path. The higher the energy of a particle at a given accelerator radius, the higher the centrifugal force and with it the required magnetic field to keep the particle on a circular orbit:

$$p[\mathrm{GeV/c}] = 0.3 \cdot Z \cdot B[\mathrm{T}] \cdot r[\mathrm{m}]. \tag{3.2}$$

In this useful equation p is the momentum of the particle (energy and momentum are about the same size, if $p \gg m$[1]), Z is the particle's charge in units of the elementary charge (1 for electron and proton) and B is the magnetic dipole field strength. The LHC uses superconducting magnets cooled with superfluid helium at 1.9 K. These magnets reach field strengths up to 8.3 T with a bending radius of 2.8 km. This radius has to be smaller than the radius of the LHC of 4.3 km because of the distances between the magnets. The LHC houses 1232 of 14 m long dipoles and about 3700 multipole correction magnets [1]. That gives an average magnetic dipole field of about 5.4 T for the LHC acceleration. Using this field and the radius of the LHC of 4.3 km in equation 3.2 leads to the maximum energy of about 7 TeV per beam (in the LEP the average field only was 0.08 T).
The protons injected in the LHC have to be pre-accelerated in an already existing system of pre-accelerators at CERN (see Figure 3.1).
The Linac receives protons from a hydrogenic source and accelerates them to 50 MeV. Then they are injected into the Proton-Synchrotron (PS), which boosts the protons to an energy of

[1] choosing $c = 1$

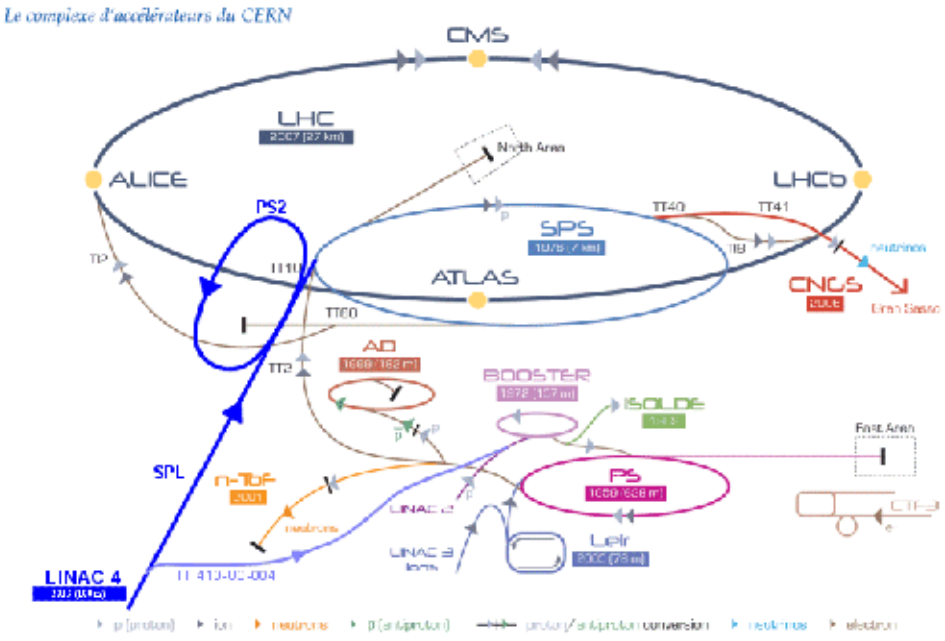

Figure 3.1: *The LHC pre-acceleration-system.*

26 GeV. With this energy the protons are injected into the final pre-accelerator, the Super-Proton-Synchrotron (SPS). It accelerates the protons to 450 GeV, the injection energy of the LHC [1]. At this point the dipole field is about 0.5 T and increases during acceleration to its maximum. The acceleration itself will be done by cavities producing an electric high-frequency field with 2 MV/m operating at 400.8 MHz. A complete fill and acceleration of the LHC will take about 260 s [1].

3.2 A Proton-Proton Collider

Unlike the LEP, the LHC will bring particles of the same charge into collision. That means different directions of the magnetic dipole fields are required for the two beams. So the LHC is constructed as two proton synchrotrons with two different vacuum pipes (one for each beam) in one cryogenic system (see Figure 3.2).

The advantages of using protons for accelerate them to high energies on the one hand bring a lot of disadvantages for the experiments on the other hand. In opposition to electrons and positrons, protons are composed objects. By colliding them, the interaction is mediated by single quarks and gluons the proton consists of. At a fixed proton energy, it is unknown what the energy-fraction of these constituents is (called partons) in the moment of collision. It can only be approximated by the energy-dependent parton distribution function (PDF). The PDFs are describing the probability to find a parton with momentum fraction x of the proton momentum in the proton. This probability is dependent on the energy transfer scale Q^2 and on the momentum fraction x. For this reason the initial energy of a single reaction is unknown at hadron colliders like the LHC.
Interactions between gluons and sea quarks will be the most important processes at the

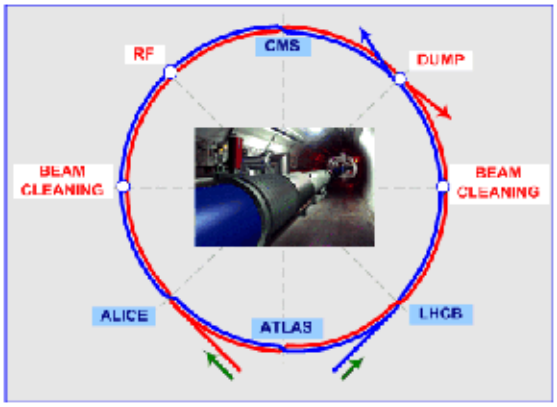

Figure 3.2: *LHC schedule.*

LHC, but as explained the initial energy and the initial quark flavours of an interaction are large sources of uncertainty for the LHC experiments. In addition, the cross sections for the relevant particle reactions will be low and the QCD-background will be large at the LHC. The only way to deal with this, is to have high statistics for data analysis of the experiments. This can only be reached with high reaction rates and for this reason a high and well known luminosity of the LHC.

3.3 Luminosity and Beam Parameters

The reaction rate R is connected to the cross section σ and the luminosity L by:

$$R = \sigma \cdot L. \tag{3.3}$$

The luminosity in units $[\,\mathrm{cm}^{-2}\,\mathrm{s}^{-1}]$ can be calculated for a collider as:

$$L = \frac{f \cdot n \cdot N_1 \cdot N_2}{4\pi \cdot \sigma_1 \cdot \sigma_2} \tag{3.4}$$

with f the circulation frequency, n the number of particle bunches, N_1 and N_2 the number of particles per bunch of beam 1 and 2, and σ_1 and σ_2 the effektive interacting areas at the collision point.
At LHC, 2808 bunches will circulate with a time delay of 25 ns and a circulating frequency of 11 kHz. The bunches are not distributed uniformly over the accelerator ring, but arranged in so called trains. The bigger time delay between two trains is necessary for powering the bunch-kicker-magnet up in case of beam ejection. So the bunch crossing frequency will be 40 MHz within the trains and each bunch will consist of $1.15 \cdot 10^{11}$ protons. With these parameters a peak luminosity of $10^{34}\ \mathrm{cm}^{-2}\,\mathrm{s}^{-1}$ is planned. But in the first years of the experiment a luminosity of $10^{33}\ \mathrm{cm}^{-2}\,\mathrm{s}^{-1}$ is expected. The cross section for proton-proton collisions at LHC is $\sigma \approx 0.1$ b at $\sqrt{s} = 14$ TeV. Thus at the peak luminosity 23 proton-proton interactions per bunch crossing and with that $R = 10^9$ events per second are expected.
Together with the high particle multiplicity of one interaction, this puts considerable demands on the detectors and their readout electronics. Also the experiments have to deal

with a huge QCD background, that has to be separated from the interesting signals. Thus precise knowledge of the luminosity is essential to interprete the reaction rates of interesting processes and compare them with known cross sections or theory predictions.

3.4 The Experiments of the LHC

At four points, both beam pipes are crossing each other as it can be seen on Figure 3.2. These four points are the interaction points of the two proton beams and 4 experiments arranged around these interaction points in the underground to measure and analyse the proton-proton interactions:

- **ATLAS** - A Toroidial LHC ApperatuS
- **CMS** - Compact Muon Solenoid
- **LHC-b** - Large Hadron Collider beauty
- **ALICE** - A Large Ion Collider Experiment

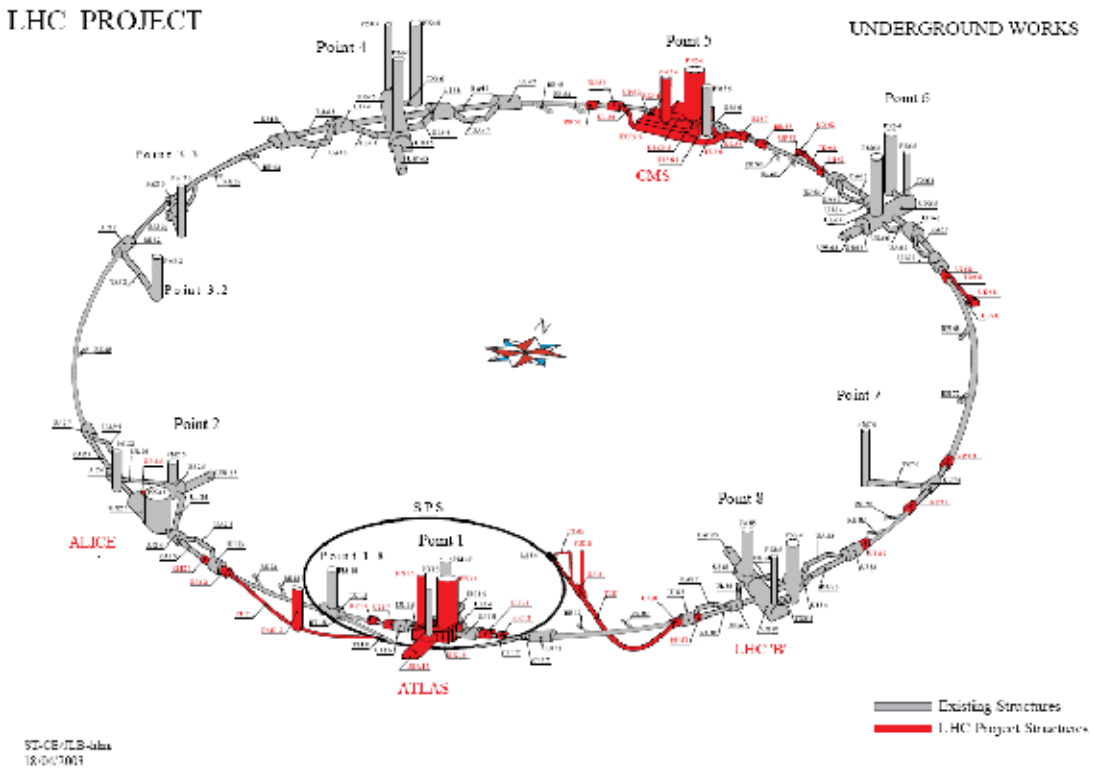

Figure 3.3: *LHC Underground constructions.*

The arrangement of the four experiments along the LHC beamline is shown in Figure 3.3.
The multi-purpose detectors ATLAS and CMS [9] are designed to search for the Standard Model Higgs-Boson, but also for physics beyond the Standard Model like Supersymmetry, extra dimensions or mini black holes. They are constructed as symmetric cylinders with onion paring structure around the interaction point and have multiple calorimeters and spectrometers.
LHC-b [5] will be able to make precise measurements of B-meson decays and CP-violation.
ALICE [3] is constructed to analyse quark-gluon plasma, when LHC will collide heavy ions instead of protons.
In the next chapters the possibility of a relative luminosity measurement with one part of the ATLAS detector - the electromagnetic section of the Forward Calorimeter FCAL - is studied.

4 The ATLAS Detector

4.1 Layout of ALTAS

The ATLAS is a cylindrical particle detector with a length of about 45 m, a diameter of about 22 m and a weight of about 7000 t. As a multi-purpose detector ATLAS has the ability to detect and reconstruct signals of all known elementary particles except neutrinos. The detector is optimized for the identification of photons, electrons and muons and a precise meassurement of the muon momenta, because they would be one of the most important decay products of the Higgs boson.
For these purposes the ATLAS includes many different systems (see Figure 4.1).

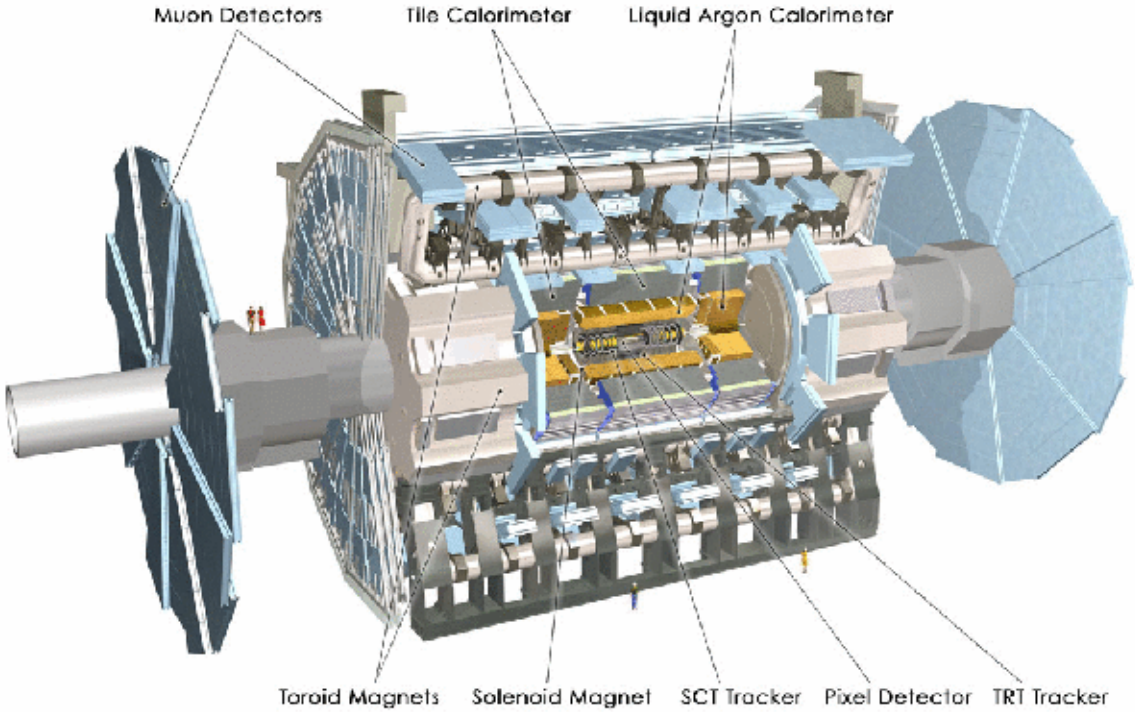

Figure 4.1: *ATLAS detector overview.*

The inner detector consists of the pixel detector, the transition radiation tracker (TRT), the semiconductor tracker (SCT) and a solenoid magnet to reconstruct the track and the charge of charged particles. The outer part of the detector consists of the Muon System with independent Toroid Magnets. This allows a high precision muon momenta measurement with a resolution of about 2% over a p_T range from 10 GeV up to 100 GeV [11]. Because of

their lifetime of $2.2 \cdot 10^{-6}$ s, their mass of 105.7 MeV and the fact that muons do not interact strongly, they can pass through the inner parts of the detector without large energy loss or absorption compared to electrons.
The calorimeter system is located between the inner detector and the muon system. It is designed to measure particle energies by the amount of energy which is deposited by particles in the sensitive detector volume during their passage or absorption. The calorimeter system consists of different parts (see Figure 4.2) to measure energy deposits of electrically interacting particles like electrons and photons on the one side and mainly strongly interacting particles like kaons, pions, neutrons and protons on the other side.

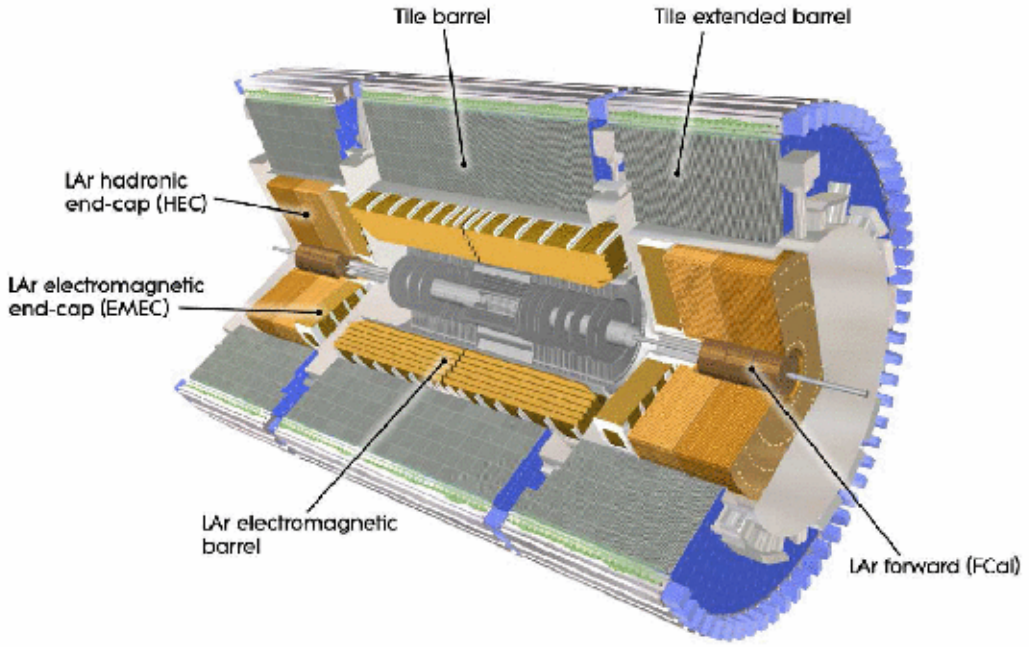

Figure 4.2: *ATLAS Calorimeter System.*

The electromagnetic (EM) barrel calorimeter builds the inner part of the calorimeter system and covers a pseudorapidity region of $|\eta| < 2.5$. The outer part is the hadronic barrel calorimeter (tile barrel) with a range of $1.5 < |\eta| < 3.2$. The endcap calorimeter includes the EM endcap calorimeter (EMEC) and the hadronic endcap calorimeter (HEC). The region under highest pseudorapidities of $3.2 < |\eta| < 4.9$ is covered by the forward calorimeter (FCAL).
The latter ATLAS subdetectors are designed as liquid argon (LAr) calorimeters. In between the absorbers, LAr gaps are located and these gaps are applied under high voltage. If a particle passes through the calorimeter, it interacts with the absorber and electromagnetic or hadronic showers are produced. Charged particles of the showers are ionising the liquid argon in the LAr-gaps instantaneously and the electrons and ions begin to drift in the argon because of the electric field. These drifting charged particles induce a current in the signal wires. Directly after ionisation the induced current has its maximum and decreases more and more, because the electrons and ions are gradually reaching the cathode and anode. In the process the ions can be neglected, because their drift velocity in LAr is about 1000-times less than that of the electrons. The induced current can be measured and the length of this

signal depends on the maximum drift time of the electrons in the LAr-gap. Figure shows 4.3 a signal shape as it is produced in the detector (triangle) and after shaping (curve with dots).

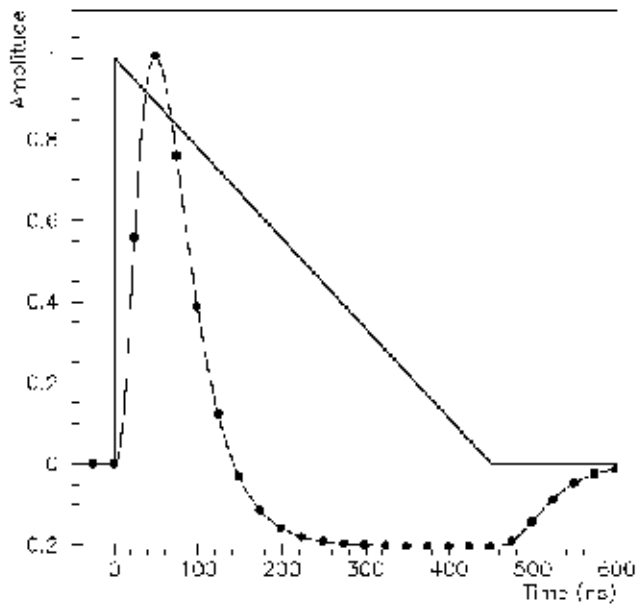

Figure 4.3: *Signal shape of one signal in the LAr calorimeter HEC [10].*

The ideal signal shape is a triangle and the signal length is typically about 400 ns for 2 mm gaps as used for example in HEC. By measuring the signal hights and summing the signals of one shower together, it is possible to calculate the deposited energy of the primary particle. Furthermore, the electrons and ions reaching the cathode or anode cause a DC-current, which has to be delivered by the HV supply system.

4.2 The Forward Calorimeter

The FCAL of the ATLAS is located next to the beam pipe and is divided into three parts as can be seen in Figure 4.2. The absorption length must be high enough to absorb all particle types except muons and neutrinos in the FCAL before the muon chambers. The first part (FCAL1) is the electromagnetic part with an electromagnetic radiation length of $\chi_0 = 29$ and a hadronic interaction length of $\lambda = 2.6$. The two other parts (FCAL2 and FCAL3) are constructed as hadronic calorimeters. This means that the energy deposited there is mainly caused by hadronic interactions of the particles. The FCAL2 covers $\chi_0 = 92$ and $\lambda = 3.5$, whereas the FCAL3 has $\chi_0 = 91$ and $\lambda = 3.4$. This sums up to a total of $\chi_0 = 212$ and $\lambda = 9.5$ for the forward calorimeter. In addition a shielding plug is installed behind FCAL in the forward tube to provide shielding for the forward muon chambers (see Figure 4.4). The dimensions of the three modules are nearly the same as it can be seen in Figure 4.4 (450 mm in z and 455 mm outer radius). In this Figure the interaction point would be at $z = 0$ and $R = 0$.

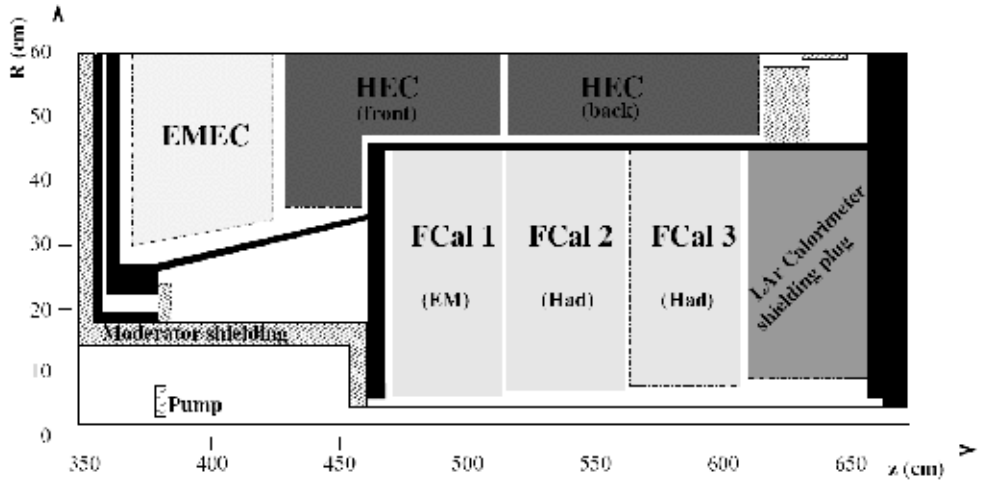

Figure 4.4: *Position of the ATLAS FCAL [10].*

The FCAL is exposed to radiation dose rates up to 10^6 Gy/yr and a neutron flux up to 10^9 cm^{-2} s^{-1} and therefore constructed using radiation damage resistant and high-Z materials. Within the absorber matrix cylindrical shell LAr gaps are located between tubular rods and tubes which are positioned parallelly to the beam pipe. The FCAL has to cover the region with the highest particle flux of minimum bias events. Thus, it was designed with small LAr gaps to minimise positive ion build up to keep the drift times short and with it the signal length. For this reason it has the ability to distinguish the signals caused by the large number of particles from one another. The FCAL1 has only 250 µm LAr gaps whereas the FCAL2 and the FCAL3 are equipped with 375 µm and 500 µm LAr gaps respectively. Thus, drift times and signal lengths are comparatively short, for example they are only 50 ns for the FCAL1.
Consequently the FCAL is constructed to detect jets and to measure their energy with a resolution of σ(E)/E < 7% and their angle with $\sigma(\theta)/\theta$ < 7% typically [10]. Further parameters of the FCAL are given in Table 4.1.

Parameter	FCAL1	FCAL2	FCAL3	FCAL(total)
dE/dx Sampling fraction (%)	1.49	1.36	1.68	
dE/dx Sampling frequency (cm^{-1})	0.59	0.36	0.34	
Depth(χ_0)	29	92	91	212
Depth(λ)	2.6	3.5	3.4	9.5
Drift time (ns)	50	75	100	
Q/E(mip)(ke^-/GeV)	297	272	337	
i_{max}/E(mip)(μA/GeV)	1.9	1.2	1.1	
Potential across gap (Volts)	250	375	500	
Electrode capacitance (pF)	379	276	27	

Table 4.1: *FCAL physical parameters [10].*

So the FCAL will be able to measure the transverse jet energy E_T with a resolution of $\sigma(E_T)/E_T < 10\%$ for $E_T > 100$ GeV [10].

4.3 The FCAL1 Module

The electromagnetic section of the FCAL is most suitable for luminosity measurements with high voltage supply currents and is therefore described in more detail in the following.
The FCAL1 module is located at a distamnce of z = 4668 *mm* to the interaction point and its cylindrical absorber matrix made of copper holds approximately 12000 tube electrodes. Each FCAL1 absorber matrix consists of nine plates of 50 mm thickness (seven absorber plates and two end plates) set up perpendicular to the z direction. A Picture of the cylindrical FCAL1 absorber matrix can be seen in Figure 4.9. The electrodes are made of copper as well and in each case four electrodes are grouped together to one tube group as it is shown in Figure 4.5.

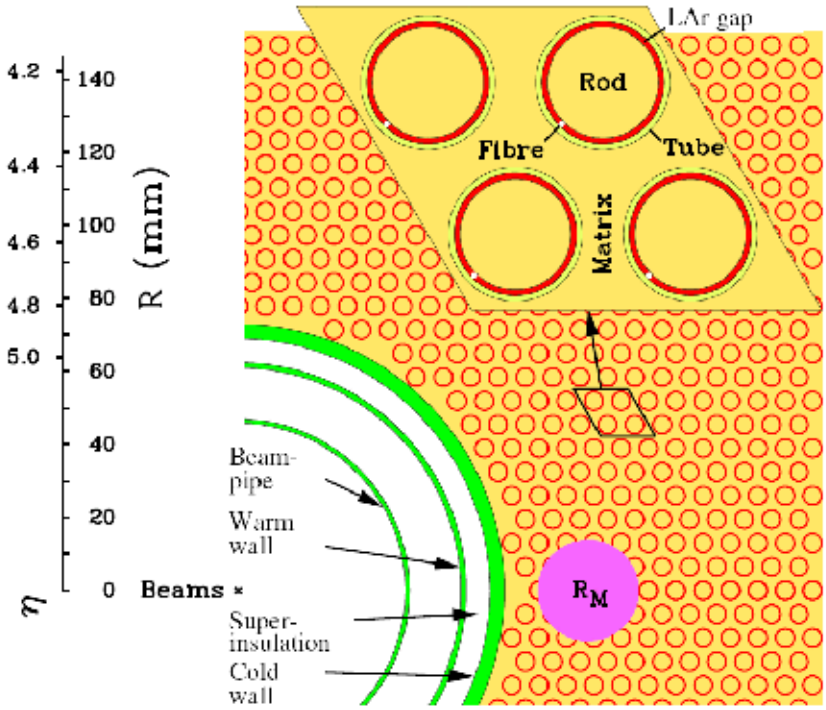

Figure 4.5: *FCAL1 Tube Groups. Each four electrodes are connected to one channel.*

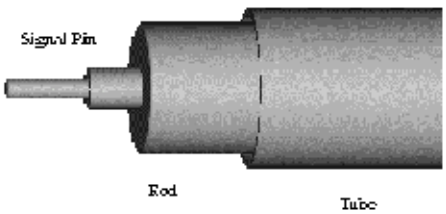

Figure 4.6: *FCAL1 Tube electrode. The signal pin is connected to the rod. Rod and tube are seperated by a LAr gap. [10].*

Figure 4.7: *Photograph of a Rod with quartz fibre.*

All tube groups are arranged parallelly to the beam pipe and by that they are covering the same area in the x-y-plane. That means the η-ϕ coverage varies by η and the particle flux that goes through the inner electrodes is higher than through the outer ones. The tube electrodes consist of an inner rod with a diameter of 4.750 mm and an outer tube with 5.250 mm diameter. The distance for the 250 µm cylindrical shell gap of liquid argon between rod and tube is kept constant by a quartz fibre wound onto the inner rod in a single helical formation (see Figure 4.7). At one end the rod carries a signal pin as in Figure 4.6. The signal pins of each tube group are connected with one coaxial cable to one preamplifier and to the HV supply system. The signal cables are grounded by an array of push-in signal pins inserted in holes in the matrix at the signal cable end of the module (see Figure 4.8).

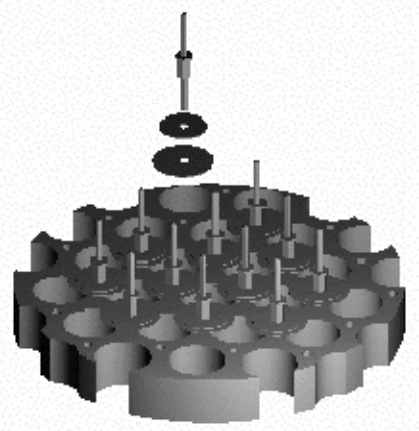

Figure 4.8: *End-plate ground pin and retainer assembly [10].*

The connection to the preamplifier for signal shaping and event readout is done across a high pass filter as it is shown in Figure 4.10. A low pass filter allowing a DC current flow is installed between the signal pins and the HV supply system to suspend large fluctuations in the high voltage applied to the LAr-gaps.

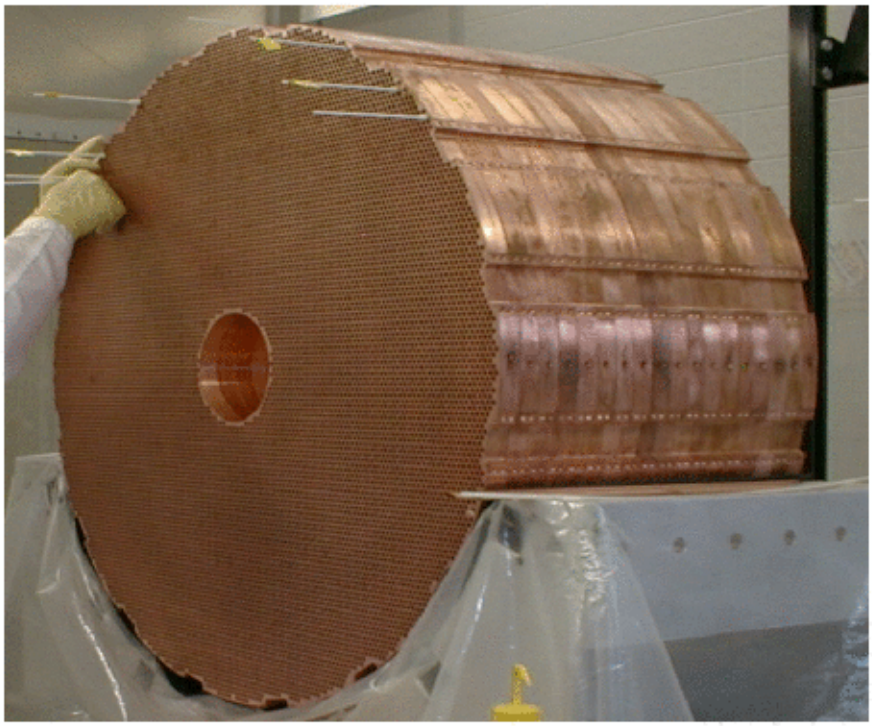

Figure 4.9: *Photograph of the FCAL1 Absorber Matrix made of copper.*

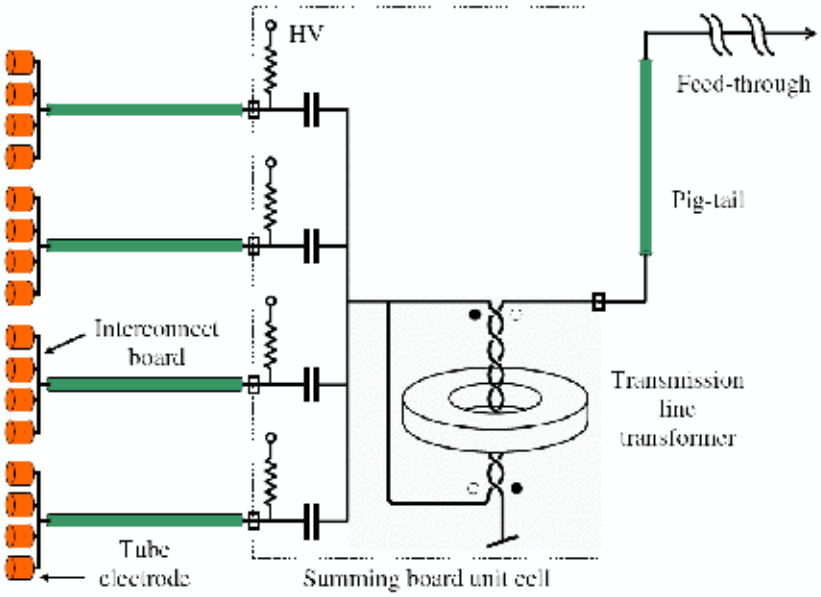

Figure 4.10: *FCAL electronic connection principle.*

4.4 Luminosity Measurement in the ATLAS Experiment

A luminosity measurement of the ATLAS detector with the highest possible precision is necessary, especially when measuring cross sections. This is the case, for example, when one analysis top-quark pair production or verifies QCD by measuring jet cross sections.
For this reason different luminosity measuring and monitoring devices are installed in the ATLAS detector. The first one is the LUCID (Luminosity measurement using Cerenkov Integrating Detector) system consisting of projektive Cerenkov tubes installed near the beam pipe in a distance of 17 m from the interaction point. It is constructed to measure the relative luminosity using the produced charged particles. LUCID covers the pseudo-rapidity range $5.4 \leq |\eta| \leq 6.1$ and a luminosity range from $10^{27}\,\mathrm{cm}^{-2}\,\mathrm{s}^{-1}$ to $10^{34}\,\mathrm{cm}^{-2}\,\mathrm{s}^{-1}$. The non-linearity is expected to be less than 1 %. A picture of LUCID before installation in ATLAS can be seen in Figure 4.11.

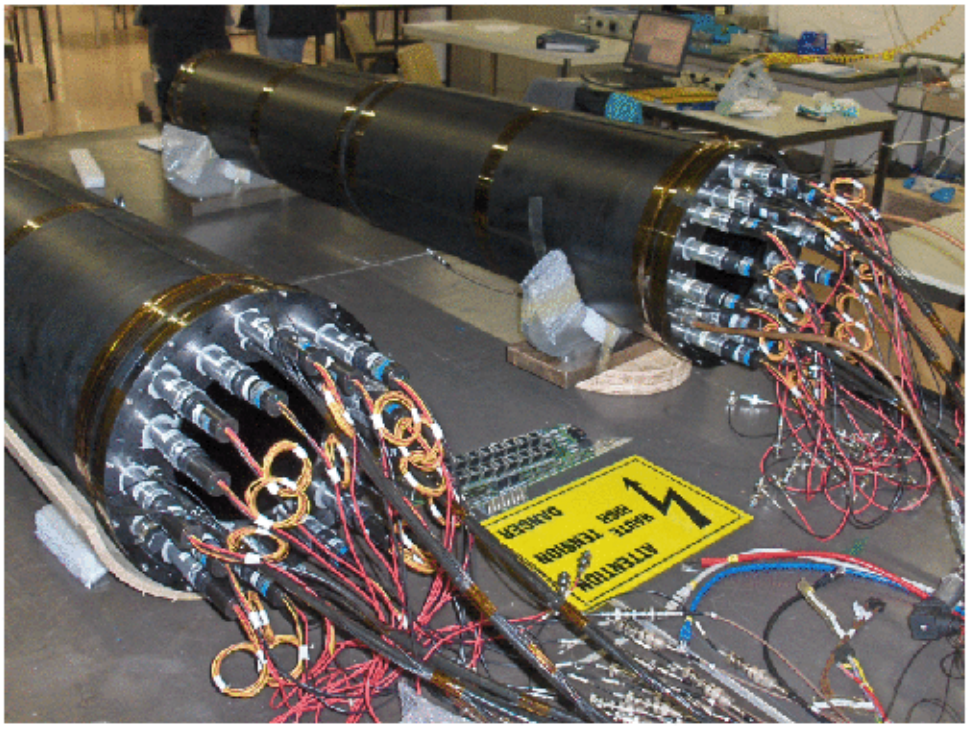

Figure 4.11: *The LUCID system before installation in ATLAS.*

Another luminosity measurement system is the Beam Current Monitor (BCM) which uses diamond crystals installed near the beam pipe to measure single minimum-ionising particles. On each side four BCM stations are installed 1.8 m away from the interaction point. This system allows a monitoring of the rate of minimum-ionising particles to detect beam losses. It also provides a relative luminosity monitoring on a bunch by bunch basis. This luminosity measurement is done by measuring the flux of charged particles in a defined solid angle as it is the case in LUCID. A picture of the BCM stations around the beam pipe is shown in Figure 4.12.

An additional system, the BRAN luminosity monitors which instrument absorbers located 141 m away from the interaction point, is provided by the LHC itself. Four quadrants each

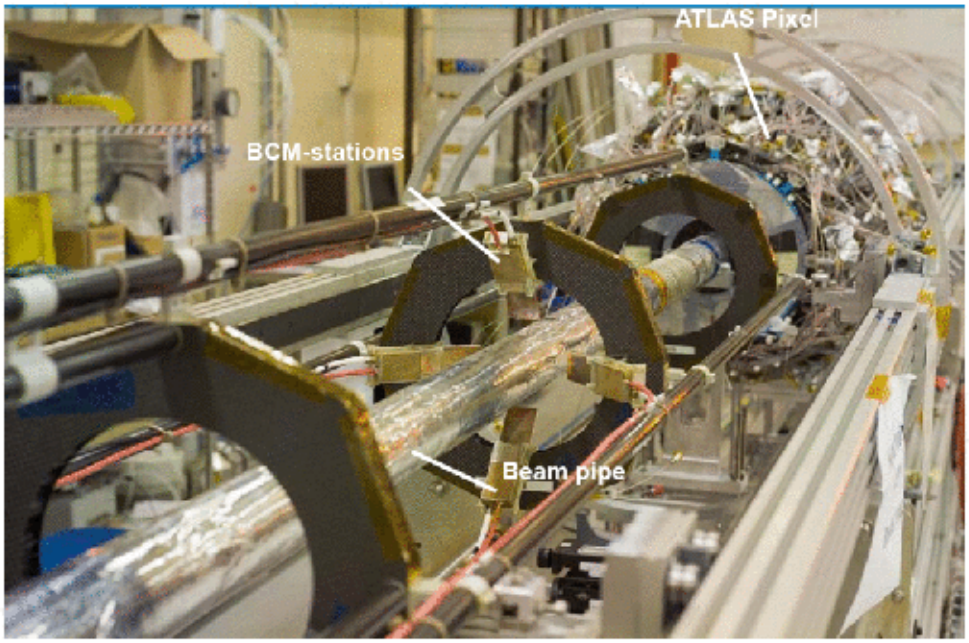

Figure 4.12: *The four BCM stations of one side. The diamond sensors have a diameter of 10 cm.*

of a size of 16 cm^2 are measuring the flux of photons and neutrons originating from the collisions. The BRAN system provides a bunch-by-bunch measurement for the relative luminosity and, in addition, information about the crossing angle at the interaction point.

All these measurement devices for the relative luminosity described above (LUCID, BCM, BRAN) have to be calibrated with an measurement of the absolute luminosity. At hadron colliders, small-angle elastic scattering is useful to measure the absolute luminosity. In ATLAS these processes will be measured with the ALFA (Absolute Luminosity For ATLAS) detector which is located 237 m away from the interaction point. ALFA provides measurements at small angles in the Coulomb-Nuclear Interference (CIN) region. Special runs with low instantaneous luminosity of only 10^{27} cm^{-2} s^{-1} are required for an absolute calibration of the luminosity by using ALFA. In the beginning of the LHC running, an uncertainty on the absolute luminosity of 20-30 % is expected using machine measurements. This can be improved by a number of calibration runs using ALFA and an absolute precision of the luminosity of 3 % is reachable.
The measurement of the relative luminosity using the FCAL1 HV currents would be an additional method for measuring and monitoring luminosity whose results can be compared with those of the other methods described above. By combining the measurements of different systems, the uncertainty on the relative luminosity can be reduced. Furthermore, each method has its own advantages and disadvantages which can be compensated by another method. Those of the luminosity measurement using the FCAL1 HV currents are explained in the following.

5 Luminosity Measurement with FCAL1

5.1 Theoretical Foundations

In [6] the possibility of a relative luminosity measurement at the LHC by reading out the HV currents of the liquid argon calorimeters in ATLAS is described. The measurements can be used for an online luminosity monitoring to detect luminosity changes on the one hand and to get the relative change in integrated luminosity per run for offline analysis on the other hand. The electromagnetic section of the FCAL (FCAL1) was proposed as a good candidate for this measurement.
Because of the large instantaneous luminosity of the LHC and their high cross sections the LHC will produce a large number of so called minimum-bias[1] events. These inelastic proton-proton interactions with low q^2 are considered in this note to obtain a high statistical precision, because they deposit most of their energy in the forward section of the detector. But it is not possible to calculate an absolute cross section for minimum bias events from theory. Therefore only a relative luminosity measurement is possible with this method.
The readout of the HV supply currents is indeed described as the only way to get the energy deposited by minimum-bias events in the calorimeter. The event readout of the calorimeter cannot be used, because most minumum-bias events will not be triggered. In addition the bipolare shaping of these signals would average a simple sum of all signals to zero.
The sum of all HV currents of the calorimeter should be proportional to the energy deposited by minimum-bias events in the whole calorimeter. This energy would in turn be proportional to the number of minimum-bias events itself, when assuming a constant average energy of these events. And finally the number of minimum-bias events would be proportional to the luminosity of the machine which is the parameter of interest:

$$L \sim N_{minimum-bias} \sim E_{deposited} \sim I_{HV}. \tag{5.1}$$

To explain Relation 5.1 in more detail, some simplifications are made in the following. A particle distribution flat in η and p_T independent of η is assumed. The p_T distributions are approximated by a delta function at their mean values and details of detector construction are neglected. The energy of charged particles is approximated by the mean energy of charged particles $< E(\bar{p_T}) >$ as a function of the transverse momentum $\bar{p_T}$ inside the angular acceptance region. With these simplifications the energy deposited in a calorimeter region between $\eta_1(\theta_1)$ and $\eta_2(\theta_2)$ can be approximated by

[1] Minimum-bias events do not have to pass a trigger which would cause a bias.

$$E = L \cdot \sigma \cdot \int_{\eta_1}^{\eta_2} \frac{\mathrm{dN}}{\mathrm{d}\eta} \cdot E(\bar{p_T}) \cdot x \cdot \mathrm{d}\eta = \mathrm{L} \cdot \sigma \cdot \frac{\mathrm{dN}}{\mathrm{d}\eta} \cdot \bar{\mathrm{p}_\mathrm{T}} \cdot \mathrm{x} \cdot (\frac{1}{\tan\theta_2} - \frac{1}{\tan\theta_1}), \tag{5.2}$$

with N being the number of charged particles and x the average energy fraction a charged particle deposits in the electromagnetic calorimeter. Now the number of ionisation pairs produced in the calorimeter per second is given by

$$N_{Pairs}[1/s] = \frac{1}{W} \cdot E \cdot f \cdot K(e/\mu) \tag{5.3}$$

with $W = 23.3\,\mathrm{eV}$ (see Table 5.1), f the calorimeter sampling fraction and $K(e/\mu) = 0.7$. The sampling fraction of a calorimeter represents the fraction of the total energy deposition (on average) deposited in the active layers of the calorimeter. $K(e/\mu) = 0.7$ is the suppression factor for electron response with respect to minimum ionising particle in the sampling medium [10]. Because of the high voltage across the LAr gap the ion pairs begin to drift and generate a current (e is the electron charge):

$$I = N_{pairs} \cdot e. \tag{5.4}$$

With these simplifications a combination of Equations 5.2, 5.3 and 5.4 leads to a proportionality between the luminosity L and the readout current I in the detector.

Property	Value
Atomic number	18
Atomic weight (u)	39.94
Atomic diameter (Å)	3.42
Normal boiling point (bp) (K)	87.27
Liquid density at bp ($\mathrm{g\,cm^{-3}}$)	1.40
Radiation length (cm)	14.2
Absorption length (cm)	83.6
$< \Delta E_{mip}(1cm) >$(MeV)	2.1
W-value (1 MeV electrons)(eV/ion-pair)	23.3
Electron mobility at bp ($\mathrm{m^2V^{-1}s^{-1}}$)	0.048
Ion mobility at bp ($\times 10^5$)($\mathrm{m^2V^{-1}s^{-1}}$)	0.016

Table 5.1: *Properties of liquid argon [10].*

In [6] it is concluded that 1% precision of a relative luminosity measurement is possible with this method, from both a statistic and a systematic point of view.
Therefore the statistical effects of a fluctuation in the number of particles hitting the detector and of fluctuations in the energy deposited by a particle are discussed in [6]. The fluctuation in the number of particles is by far the dominant effect. But the time constant of the low pass filter before the FCAL1 of about 2.5 ms is high enough to average out these fluctuations and in addition summing over all HV channels would reduce the noise even more.
The following systematic effects are discussed in the note [6]:

- **Background currents** are expected from natural material activity even without colliding beams. It is possible to measure these currents without a beam and then subtract them from those obtained with beams, because such a background can be assumed to be constant.

- **Recombination** is a possible source of non-linearity, because it can occur during a large positive space charge density. The rate of recombination depends on the ionisation density which is proportional to the luminosity . As concluded in Ref [] the ionisation density for the FCAL1 is less than the critical density even in FCAL regions close to the beam pipe where the ionisation density is expected to be largest. For this reason a non-linear effect for the FCAL1 HV current is expected to be less than 1% even at high luminosities.

- **Detector activation** can cause additional currents. It was calculated that it is much smaller than those due to primary interactions and thus can be disregarded.

- **Temperature variations** have an effect on the current because of density changes of the liquid argon. This effect is about 0.5 %/K for FCAL temperature variations of $\triangle T < 0.4$ K.

- **Displacement of the mean interaction point** along the beam axis of about 1 cm would cause a variation of the HV current of about 0.2 % for the FCAL1. Summing the current of the FCAL1 modules on both sides of the detector would reduce the variation to less than 0.1 %.

- **Lost beam particles** and cascades initiated by protons lost outside the detector could reach the FCAL and charged particles from primary and secondary interactions in the detector can induce a HV current in the FCAL1. Taking the shielding of ATLAS into account, calculations are leading to an additional HV current of the order of 0.1 nA and thus can be neglected.

This relative luminosity measurement method is studied here using the FCAL1 in ATLAS. In the following the HV supply system of the calorimeter part is described in more detail.

5.2 The HV Supply System of the FCAL1

The measurement principle including the most important electronic devices is displayed in Figure 5.1. At the calorimeter is a high voltage of 250 V applied. When a charged particle passes through, it behaves as a current source. This current can then be measured between the HV supply and the low pass filter. At the signal readout wire a high pass filter with a blocking capacitor is installed and no DC current can flow away on this side.
The note also describes the most important requirements for the HV power supply system of FCAL1 to achieve a 1% precision of the relative luminosity measurement. The most important one is that the HV current measurement resolution of the HV modules of the ATLAS FCAL1 is sufficient to detect current variations of 1 % or better. In addition the protection resistors in front of the calorimeter have to be designed such that non-linearities in the current readout are kept to less than 1 %. A filter network of low pass filters reduces the noise before digitisation and smoothes statistical fluctuations on short time scales.

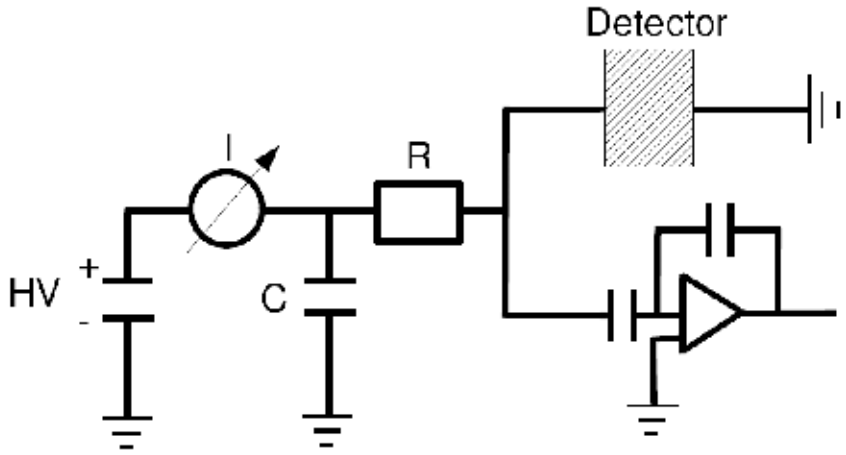

Figure 5.1: *HV current measurement principle for one HV channel of the ATLAS FCAL. The wire with the low pass filter included is used for HV supply and HV current measurement. The wire with the blocking capacitor is used for calorimeter signal readout.*

In the following the HV supply system for the ATLAS FCAL1 and its compliance with these requirements are described. HV supply crates from the Dresden company ISEG [] are used for the FCAL1. Every crate has four HV channels for high voltage supply, voltage measurement and current measurement. The FCAL1 HV supply structure is constructed in a way that both FCAL1 modules are divided into 16 sections in ϕ and each HV supply crate powers one of these sectors.
In Chapter 4 it was described that four tubes of the ATLAS FCAL1 are always combined to one tube group. The connection to the HV channels is provided in such a way that always 64 tube groups are connected to one HV channel in parallel. The tube groups of one channel are distributed over the whole η range of the FCAL1 so that there are no η dependent differences between the channels. This means that every section in ϕ is connected to four HV channels with 64 tube groups each. Altogether there are 128 HV channels for both FCAL1 modules.
The HV cables of the inner 32 tube groups of one HV channel have 1 MΩ protection resistors and the outer 32 are protected by 2 MΩ resistors. The resulting resistance of the HV line of one channel can be calculated via

$$R = \frac{1}{\frac{32}{1\mathrm{M}\Omega} + \frac{32}{2\mathrm{M}\Omega}} = \frac{1}{48}\mathrm{M}\Omega = 20.8\mathrm{k}\Omega. \tag{5.5}$$

Together with the filter resistors the time constant is about 2.5 ms for each HV channel. This time constant is much higher than the 25 ns between two bunch crossings in LHC (as described in Chapter 3) and the 50 ns response time for a signal of the FCAL1 itself. This means that one HV current measurement averages over a lot of bunch crossings in LHC and that the calorimeter response time do not influence the measurement.
The HV supply modules installed for the ATLAS FCAL1 are equipped with 20 bit ADCs for digitisation achieving a resolution of < 20 nA. The readout cycle for current- and voltage measurements in all four channels takes less than 1 s for each HV crate.

So the filter network of the FCAL1 is well designed to suppress noise and short-term statistical fluctuations. The current measurement resolution is good enough to detect 1 % variations with a safety factor of 5 at an expected current of > 10 µA per HV channel.
But nevertheless there are many statistic and systematic effects in this measurement idea, that it is necessary to proof the proportionality between the luminosity and the HV supply current in a testbeam. In such a fixed target experiment the time structure of the beam has to be considered, because there are a lot of seconds without beam between two pulses. The participation at such a testbeam with a small FCAL1 prototype is described in the following.

6 The Protvino Testbeams

6.1 The Purpose of the Testbeams

It is planned to increase the nominal luminosity of the LHC of 10^{34} cm^{-2} s^{-1} by a factor of 10 to 10^{35} cm^{-2} s^{-1} after a few years of running. For this later period (sLHC-phase) it is important to test the various detector components, whether they are working correctly for such a high particle flux or whether they would have to be modified. Testbeams to investigate this for the electromagnetic endcap calorimeter (EMEC), for the hadronic endcap calorimeter (HEC) and for the FCAL1 took place at the proton synchrotron U-70 in Protvino, Russia, located about 100 km south of Moscow. The high interaction rate and particle flux at the sLHC was simulated by placing the calorimeter prototypes directly into the proton beam behind iron absorbers. During this hilumi testbeams it was possible to run with different beam intensities and therefore simulate different LHC luminosities .
For that purpose a unique beam extraction technique using bent crystals [] comes into operation in Protvino. With those bent crystals the primary proton beam can be extracted gradually and the extraction of one accelerator fill can take a few seconds. The extracted beam intensity can be adjusted by moving the bent crystals.
This capability was used to measure the HV current of the FCAL1 and to compare it with the beam intensity at multiple intensity steps during the Protvino testbeams. Therefore it was important to ensure that both the beam intensity and the FCAL HV current were measured and read out with the required precision and rate during the testbeams. In addition, the time structure of the beam had to be compatible with the HV current measurement parameters. That means the bunch spacing had to be shorter than the period the current measurement integrated over and the time constant of the low pass filter. Furthermore, the time with the beam turned on without interruption (spill) had to be longer than the current measurement cycle time and much longer than the time constant of the low pass filter. The bunch structure and the spills are explained in more detail in the next section.
To collect all important information, a technical run took place before the testbeam itself. Dates and activities during the Protvino Testbeams are listed in Table 6.1.

Year	Date	Activity
2007	01.10. - 10.10.	Technical run
2007	03.11. - 10.11.	Technical run
2007	11.11. - 18.11.	Beam run
2008	11.04. - 15.04.	Beam run

Table 6.1: *Dates and activities during the Protvino testbeams.*

6.2 The U-70 Accelerator and its Beam Parameters

The U-70 is a proton synchrotron with a maximum beam energy of 76 GeV. It is operating since 1967 and belongs to the Institute of High Energy Physics (IHEP), Protvino. The accelerator ring with a perimeter of 1.48 km at IHEP can be seen in Figure 6.1.

Figure 6.1: *The U-70 accelerator at IHEP, Protvino. The synchrotron has a perimeter of* 1.48 *km.*

The protons are pre-accelerated in a linac up to an injection energy of 1.32 GeV before they are injected into the U-70. The U-70 can be filled with a maximum of 30 bunches with a bunch spacing of 165 ns. Only 5 bunches out of the possible maximum of 30 bunches were used and filled with protons in the hilumi testbeams. With a distance between each two bunches of about 1 µs. After accelerating to the required maximum energy, the beam can be extracted into one or more beam lines leading to the experiments. One accelerator fill can be extracted over a time frame of maximum 3.5 s. This means that the so called burst or spill is at most 3.5 s long. In addition the accelerator can operate in a debunched mode, i.e. the synchrotron bunch structure is smoothed and the beam is distributed uniformly over the spill. The idea for the hilumi testbeams was that one proton bunch with ∼15 ns FWHM length would simulate one hadronic shower in the calorimeters. Therefore, only the bunched beam was useful for the hilumi beamline, but not the debunched mode.
After extracting one accelerator fill, it takes about 9.5 s to pre-accelerate, inject into the U-70, accelerate to nominal energy and extract another spill into the beam line. In the hilumi testbeams a spill length of about 1.2 s was used. It was possible to get a beam intensity ranging from 10^7 p/spill (∼10 p/bunch) to 10^{12} p/spill (∼10^6 p/bunch) after extraction.
The layout of the Protvino accelerator ring can be seen in Figure 6.2 and the beam structure

used at the hilumi beam line is shown in Figure 6.3. The most important beam parameters are summarised in Table 6.2.

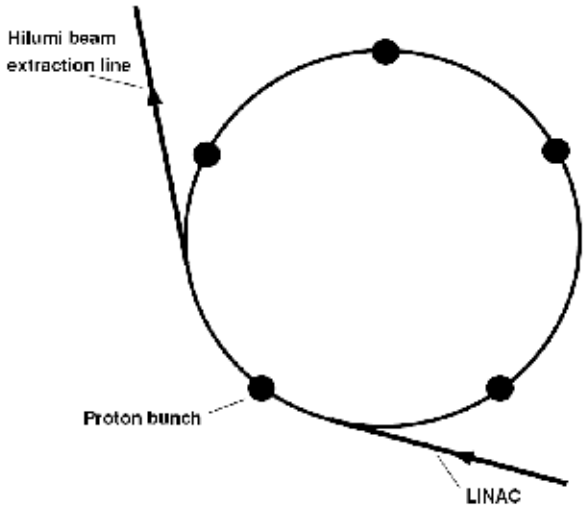

Figure 6.2: *The Protvino accelerator ring with five of 30 bunch spots filled with protons. Between each pair of filled bunches are five empty bunch spots. There is approximately 990 ns time between the filled bunches.*

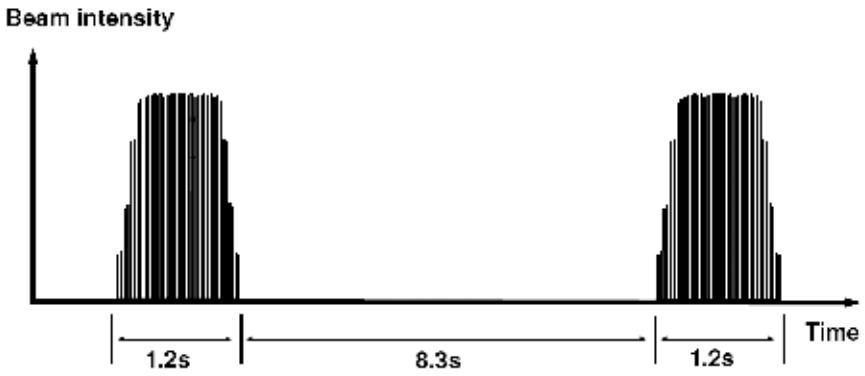

Figure 6.3: *Idealised beam structure after extraction into the hilumi beam line (bunched mode only). One spill includes the protons of one accelerator fill and is about 1.2 s long. The synchrotron bunch structure with the bunch spacing of about 990 ns is indicated within the spill. The spill cycle time was about 9.5 s leading to a time intervall between the spills of about 8.3 s. In reality the plateau is not nearly as flat as indicated in the figure.*

Beam parameter	Maximum/nominal	In hilumi test beams
Beam energy	76 GeV	50 GeV
Injection energy	1.32 GeV	1.32 GeV
Number of bunches	30	5
Bunch spacing	165 ns	990 ns
Plateau length for extraction	3.5 s	1.2 s
Spill cycle time	9.5 - 9.85 s	9.5 s
Beamsize at extraction point (FWHM)	∼2 cm	∼2 cm
Beam intensity at extraction point	10^6 - 10^{12} p/spill	10^7 - $5 \cdot 10^{11}$ p/spill

Table 6.2: *Beam parameters of the U-70 accelerator for nominal usage and as used in the hilumi test beams.*

6.3 Experimental Setup and Beam Monitoring

The experimental setup used at the hilumi beamline in Protvino is shown in Figure 6.4. A high priority in the experimental area was the beam monitoring to determine the beam intensity and beam position as precisely as possible at all time. For that purpose several beam monitoring devices were installed between the extraction point and the calorimeter cryostats.

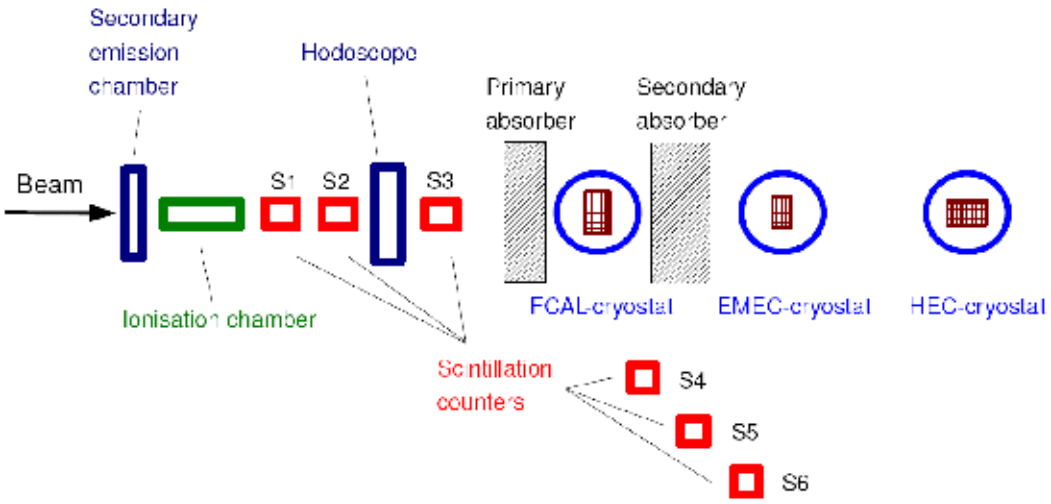

Figure 6.4: *Layout of the experimental setup of the hilumi test beam. The primary absorber had an absorption length of about 0.7 λ and the secondary absorber of about 1.8 λ. Here the beam direction is from left to right.*

The first device was a secondary emission chamber filled with a gas and a matrix of wires under high voltage. It was used for a beam position measurement in the high intensity range. The second device, a ionisation chamber was the most important beam intensimeter, because it was able to measure the relative beam intensity over nearly the full intensity range. The ionisation chamber measured the integrated intensity over one spill. Its absolute

calibration was done by activated aluminium foils analysed after the testbeam. In addition, six scintillation counters, three inside the beamline (S1-S3) and three under large angles next to the beam (S4-S6), were installed. They were used as a second intensimeter for the lowest intensities and to have a cross check for the ionisation chamber. The advantage of these counters was the fast response time and a time resolution of about 10 ns. With these counters it was possible to separate the bunches so that they could be used as a bunchtrigger as well. Finally a matrix of 32 scintillation counters arranged horizontally and vertically to measure the x- and y-extension and position of the beam was installed inside the beamline in front of the calorimeters. This so called hodoscope can monitor the beam position at low intensities. The hodoscope and the counters S1, S2, S3 inside the beamline were working at low intensities up to about 10^8 p/spill and had to be moved out of the beam at higher intensities to avoid damage. The counters S4, S5, S6 are detecting secondary particles after scattering the proton beam off the absorbers. Because of the much lower rate of secondary particles, these large-angle counters are also working in the high intensity regime. A summary of the beam monitoring devices is given in Table 6.3.
The absorbers were arranged in front of the calorimeter prototypes to increase the beam size and to tune the particle flux through the calorimeters.

Device	Measurement	Time resolution	Intensity [p/spill]
Secondary em. chamber	Beam position	spill	$> 5 \cdot 10^9$
Ionisation chamber	Beam intensity	spill	$2 \cdot 10^7$ - $2 \cdot 10^{11}$
Counters S1,S2,S3	Beam intensity	$\sim$10 ns	$< 5 \cdot 10^7$
Counters S4,S5,S6	Beam intensity	$\sim$10 ns	$< 10^{10}$
Hodoscope	Beam position	bunch	$< 5 \cdot 10^7$

Table 6.3: *Beam monitoring devices for hilumi testbeam.*

The calorimeters themselves were located in cryostats filled with liquid Argon and cooled with liquid nitrogen. The liquid argon has to be kept clean from oxygen pollution. Because of its high electronegativity, oxygen would capture the drifting electrons. To keep the argon purity high (< 1 ppm oxygen pollution), the cryostats were under high pressure of about 1.5 bar. The two absorbers consisting of multiple iron plates were installed in front of and behind the FCAL cryostat. The primary absorber had a thickness of about 0.7 absorbtion lengths and the secondary absorber of about 1.8 λ. That way the particle flux going through the calorimeters was of about the same size as it will be the case in ATLAS. Behind the absorbers, the particle flux through the calorimeters consisted mainly of pions and protons.
In Figure 6.5 a picture of the beam area with the beam monitors and the cryostats is displayed. Next to the beam extraction point on the right the secondary emission chamber (bright box) can be seen, followed by the black counter S1, the ionisation chamber tube and the counter S2. To the left the hodoscope hides the counter S3 and the support for the first iron absorber is visible in front of the three cylindrical cryostats on the left of the picture.

Figure 6.5: *Beam area of the Protvino hilumi testbeam. Here the beam direction is from right to left. The devices visible from right to left: secondary emission chamber, scintillation counter S1, ionisation chamber (barrel in the middle of the picture), counter S2, hodoscope and the three cryostats.*

6.4 The FCALchick Project

In ATLAS the FCAL1 is exposed to the highest particle flux and energy density. For this reason only one absorber of 0.7 λ was installed in front of the FCAL module. The FCAL module in Protvino is called the FCALchick, a Russian diminutive of the FCAL1. The FCALchick project is lead by the group of John Rutherfoord at the University of Arizona. Its goal is to test the electromagnetic section of the FCAL in the harsh radiation environment of the sLHC phase. The FCALchick consists of two parts: one part with 250 µm LAr gaps like in ATLAS and one part with only 100 µm LAr gaps between the rod and the tube. The latter one was designed for the sLHC phase and the goal was to test it during the Protvino testbeams. The FCALchick includes 16 electrodes of the 250 µm gap type, 16 electrodes of the 100 µm gap type and a cooling loop for the liquid nitrogen cooling. A layout of the FCALchick can be seen in Figure 6.6. The shaded circles show the anticipated beam size in front of the absorbers. As in ATLAS four electrodes are combined to one tube group in each case. Every tube group is connected to one channel. The electrodes of the FCALchick are only 50 mm long instead of 450 mm as for the ATLAS FCAL1. A picture of the FCALchick with some rods taken out is shown in Figure 6.7. The eight FCALchick channels were connected to an electronics box, where the filters are

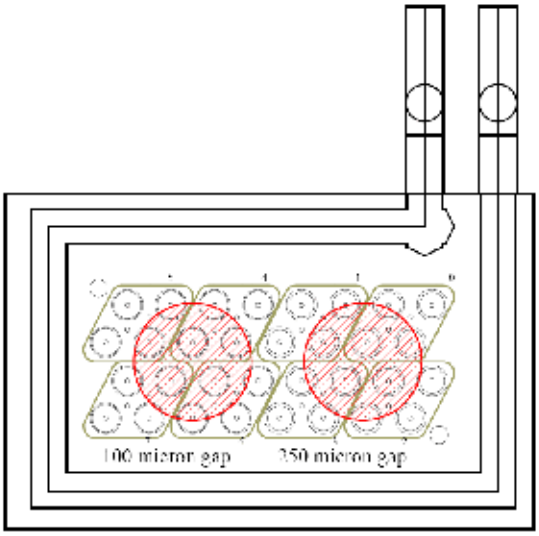

Figure 6.6: *Layout of the FCALchick used in the Protvino test beams. It consists of four channels (each including four cylindrical electrodes) of the* 250 *µm gap side, four channels of the* 100 *µm gap side and a cooling loop. The red circles show the anticipated beam size in front of the absorbers.*

placed and the cables are split into the signal readout wire and the high voltage supply wire. The low pass filter at each HV channel had 105 kΩ protection resistors and 220 nF filter capacitors. With that the time constant of the filters is $\tau \approx 4$ ms nearly identical to the ATLAS FCAL1 HV channel.
For the FCALchick testbeam in Protvino an older HV supply crate from ISEG was installed. The current measurement of that HV module had only effective 16 bit ADCs for current digitisationleading to a resolution of about 200 nA over an allowed range from −10 mA to +10 mA. For monitoring, controlling, and data readout the PVSS[1] system was used as it will be the case in ATLAS. PVSS stands for Process Visualisation and Steering System. The measured voltages and currents were saved in the PVSS internal archive. The minimum current readout cycle time was 1 s, so that one current measurement per second for each channel was written into the PVSS archive. This means that with a spill length of about 1.2 s, one measurement per spill was possible. But it was not known where exactly within this one second, e.g. within the spill the measurement took place. The reason for that is that the ISEG HV module did not provide a precise timestamp for each measurement. This could cause a problem in the case of non-constant beam intensities during one spill, because it would be impossible to compare the measured HV current with the real beam intensity at the moment of the measurement.
In addition, the resolution of about 200 nA could be insufficient in the low intensity region. Before the start of the beamruns operating parameters of the FCALchick were estimated and can be seen in Table 6.4 [17].
In this estimate the parameters are extrapolated linearly to the highest intensities. Using the HV current per channel given in Table 6.4, it can be estimated that at least up to the 10^8 p/spill intensity region, the resolution of 200 nA per HV channel would be insufficient

[1]Process Visualisation and Steering System

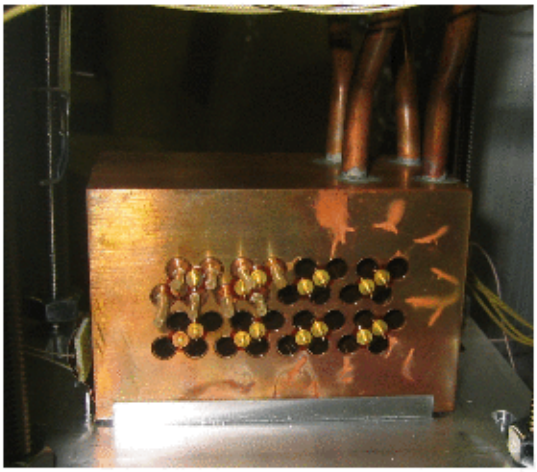

Figure 6.7: *The FCALchick used in the Protvino testbeams with some rods missing. At the front side some signal pins are visible.*

Protons/spill	10^7	10^8	10^9	10^{10}	10^{11}	10^{12}
Protons/bunch	5	50	500	5000	$5 \cdot 10^4$	$5 \cdot 10^5$
LHC lumi equal [cm^{-2} s^{-1}]	10^{32}	10^{33}	10^{34}	10^{35}	10^{36}	10^{37}
FCAL heating dE/dx [W]	$3.5 \cdot 10^{-4}$	$3.5 \cdot 10^{-3}$	$3.5 \cdot 10^{-2}$	0.35	3.5	35
Ohmic heating [W]	$2.5 \cdot 10^{-5}$	$2.5 \cdot 10^{-4}$	$2.5 \cdot 10^{-3}$	$2.5 \cdot 10^{-2}$	0.25	2.5
$\triangle$T rod - tube [mK]	0.012	0.12	1.2	12	120	1200
Pulse peak in ADC counts	240	2400	24000	$2.4 \cdot 10^5$	$2.4 \cdot 10^6$	$2.4 \cdot 10^7$
HV current [µA]	0.49	4.9	49	490	4900	49000
HV current / channel [µA]	0.12	1.2	12	120	1200	12000

Table 6.4: *Protvino beam intensities and FCALchick (250 µm side) operating parameters for the different beam intensities [17].*

for obtaining a monitoring precision of 1%. The most important parameters of both ISEG HV supply modules (used for FCAL1 in ATLAS and in Protvino) are summarised in Table 6.5.

Used in	ATLAS	Protvino
Serial Nr.	472xxx	473xxx
Maximum current	6 mA	10 mA
Current digitalisation ADC's	20 bit	16 bit
Current measurement resolution	10 nA	200 nA

Table 6.5: *ISEG HV module parameters.*

In addition, the HV current flowing per HV channel line in Protvino is much less than in ATLAS, because the electrodes are nine times shorter and only one instead of 64 tube groups is connected to one channel. For these reasons, during the technical run in October 2007 it was decided to design and build an independent HV current measurement device for the forthcoming beamrun in November 2007 to measure the HV current of the four FCALchick

250 µm channels with a better resolution and a higher frequency.

6.5 The Dresden HV Current Measurement

To estimate the required precision of the measurement of the HV current, the current flow through the calorimeter was calculated as detailed below:
The energy loss of a minimum ionising particle in liquid argon is given by

$$\frac{\mathrm{dE}}{\mathrm{dx}} = 1.51 \ \frac{\mathrm{MeV} \cdot \mathrm{cm}^2}{\mathrm{g}} \cdot \varrho_{LAr} \tag{6.1}$$

and the density of LAr at the boiling point is [10]

$$\varrho_{LAr} = 1.40 \ \frac{\mathrm{g}}{\mathrm{cm}^3}. \tag{6.2}$$

This leads to a minimum energy loss of

$$\frac{\mathrm{dE}}{\mathrm{dx}} = 2.1 \ \frac{\mathrm{MeV}}{\mathrm{cm}} \tag{6.3}$$

as given in Table 5.1, together with the energy required for one ionisation of 23.3 eV [10]. This means one minimum ionising particle produces

$$N = \frac{2.1 \ \frac{\mathrm{MeV}}{\mathrm{cm}}}{23.3 \ \mathrm{eV}} \simeq 9000 \ \frac{\mathrm{ion-pairs}}{\mathrm{mm}} \simeq 1.44 \ \frac{\mathrm{fC}}{\mathrm{mm}}. \tag{6.4}$$

With a potential of 1 kV/mm the drift velocity of electrons is about

$$v = 5 \ \frac{\mathrm{mm}}{\mu\mathrm{s}} \tag{6.5}$$

at T∼85 K. This leads to a measureable current of

$$I = 1.44 \ \frac{\mathrm{fC}}{\mathrm{mm}} \cdot 5 \ \frac{\mathrm{mm}}{\mu\mathrm{s}} = 7.2 \ \mathrm{nA} \tag{6.6}$$

per minimum ionising particle. This means, even at the lowest beam intensities in Protvino, HV-current variations caused by beam-intensity variations were expected to be larger than 7.2 nA, because this would be the HV current caused by a single charged particle.
The HV curent measurement device[2] uses 24 bit ADCs to digitise the voltage drop over a 125 Ω resistor. That way it was possible to measure the current over a maximum range from −10 mA to +10 mA. Over this 20 mA region a resolution of

[2] Designed by Andreas Glatte, an electronics engineer at TU Dresden.

$$\triangle I = \frac{20\ \mathrm{mA}}{2^{24}} \simeq \frac{20\ \mathrm{mA}}{1.68 \cdot 10^{7}} \simeq 1.2\ \mathrm{nA} \tag{6.7}$$

per bit was achieved.

Electronics noise mainly coming from the HV supply crate limited the effective resolution. To reduce it as much as possible an additional filter capacitor of 20 µF was installed in parallel to the 125 Ω resistor. The cut-off frequency of that filter is approximately 35 Hz. The effective resolution including electronics noise turned out to be about 20 nA (depending on the channel). A sketch of the design of this device is shown in Figure 6.8.

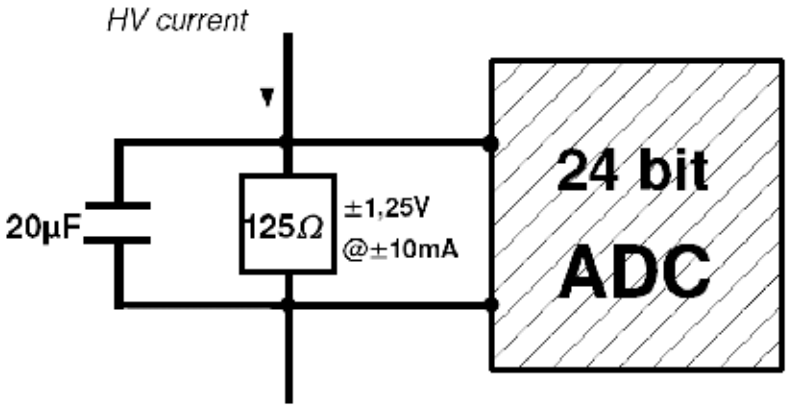

Figure 6.8: *Electrical circuit of the independent Dresden HV current measurement device. The HV current flow is measured using the voltage drop over a* 125 Ω *resistor. This voltage drop is digitised by a 24 bit ADC.*

The measurement box also includes a microcontroller and a realtime clock to add a timestamp to every measurement. The rate was 10 measurements/second/channel and the precision of the timestamp was 10 ms. Also HV connectors were included to connect the box with the HV line in front of the HV crate. A picture of the Dresden measurement box can be seen in Figure 6.9. The data transfer and power supply of the measurement box was realised by a 30 m long LAN-cable going from the box next to the HV crate (Rack 1) to the beam hut (Rack 2) as shown in Figure 6.10.

To exclude influences from the current measurement on the HV supply system itself, optocouplers with 2 kV isolation were included to transmit the ADC information. For transferring the data to a computer, a serial RS422 gateway was used. The data taking and monitoring of the HV currents was done via a program integrated into LabView. To edit this program was part of this thesis and the resultig interface can be seen in Figure 6.11.

With this program it was possible to set all relevant data recording parameters like the number of measurements per recorded file. In addition, functions for adjusting the real time clock and for resetting and calibrating the four ADCs were included (top half of Figure 6.11). To prevent fluctuating offset calibration of the ADCs during data taking, an automatic calibration function was included with the possibility to calibrate the ADCs automatically after each spill. In this function a calibration of the ADC was performed with a delay, when the

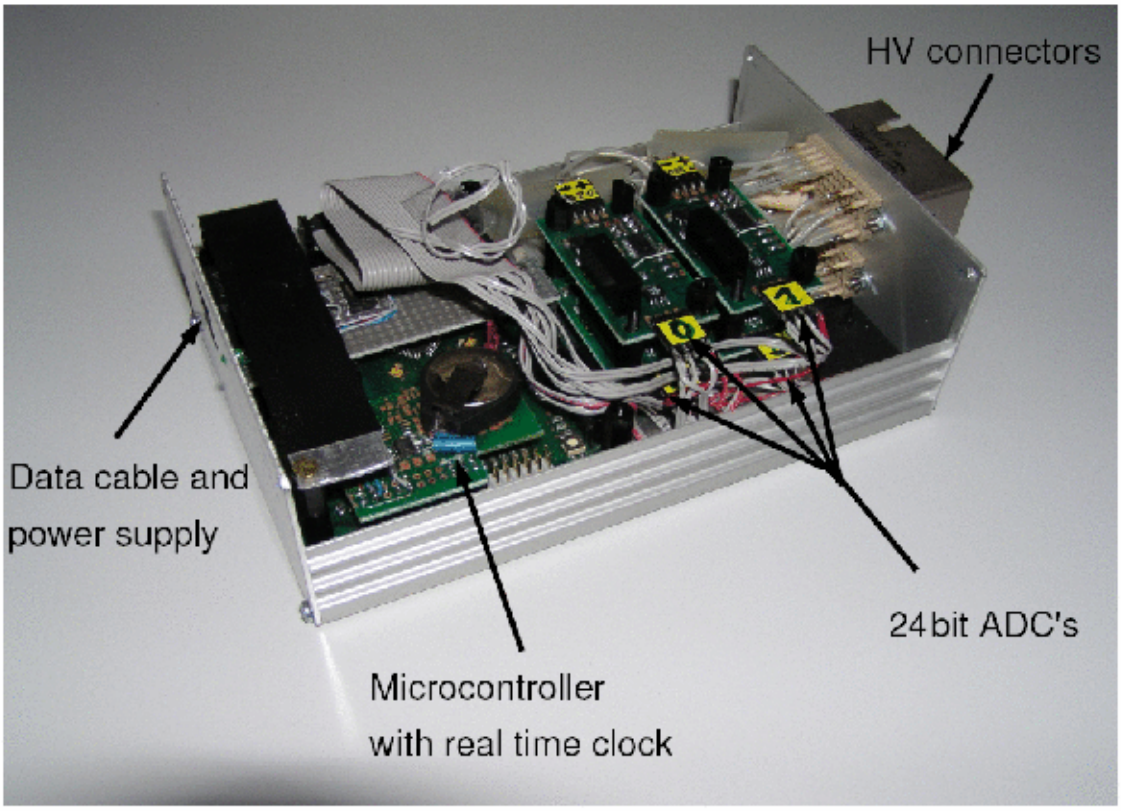

Figure 6.9: *Dresden HV current mesaurement device. The four 24 bit ADCs for the four FCALchick 250 µm channels are connected to a microcontroller to process their data and add a timestamp from the real time clock to each measurement.*

average HV current of the channel was higher than a choosen threshold. The delay and the time for averaging were adjustable and mostly set to 1 s for averaging and to 3 s for the delay. For this reason the time interval for averaging was nearly one spill length and the delay excluded calibration during a spill which would interrupt the measurement. In addition it was possible to observe the current flow of each channel in four real time histograms (bottom half of Figure 6.11). The visible time intervall of these histograms was adjustable, too. The history of the histograms was set to one hour.

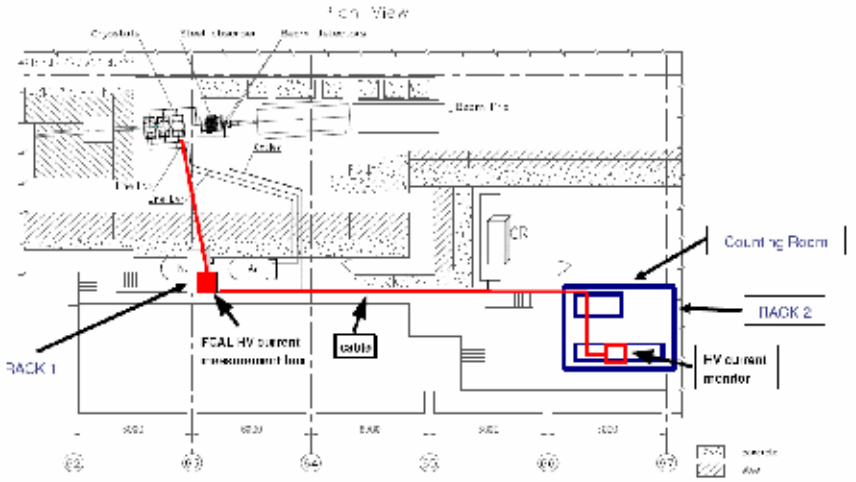

Figure 6.10: *Hilumi testbeam area in Protvino. The HV supply crate and the Dresden HV measurement device are located outside the beam area itself. A LAN cable was used to send the FCALchick HV current information to the counting room. The beam area was shielded by a wall of armoured concrete.*

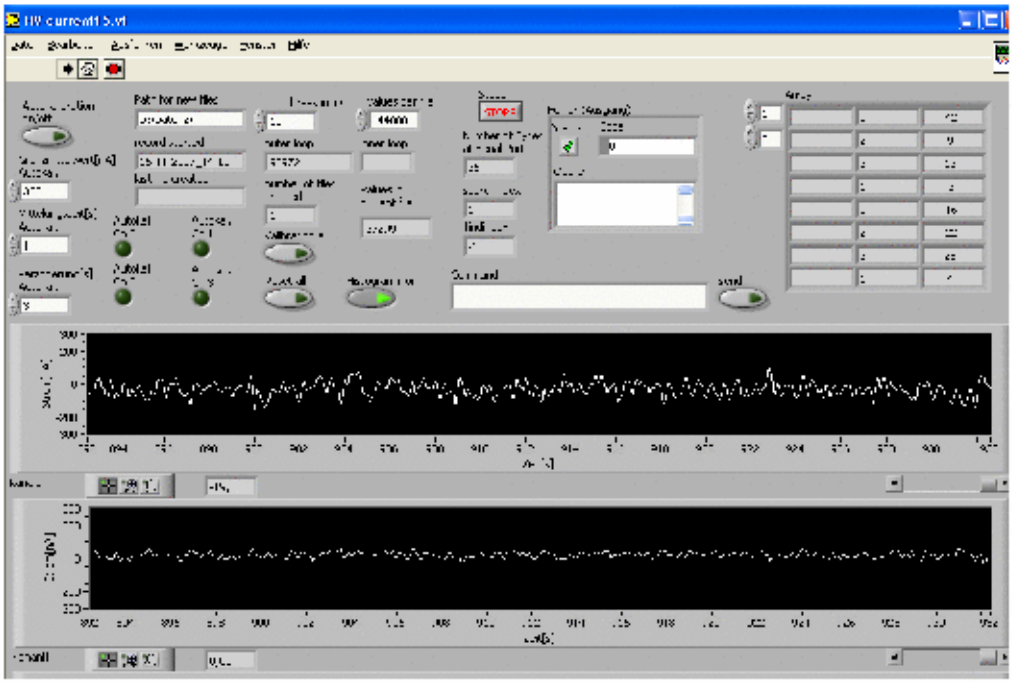

Figure 6.11: *FCAL HV current measurement interface. At the top of the interface some buttons for setting the data recording parameters and the ADC-calibration options are arranged. At the bottom the real time histograms of the measured HV current are visible.*

6.6 Data Taking

The first beam run took place in November 2007. At the beginning of the run it was possible to install the 4-channel HV current measurement device successfully. Due to problems with the electronics of the calorimeter signal readout, the cryostats, the purity of the liquid argon and the proton beam itself only one and a half day for data taking was left. Early in the run it turned out that the purity of the liquid argon was not as high as required (1 ppm). It was even not sufficient for a precise purity measurement indicating values worse than 3 ppm. But the influence of the oxygen pollution on the HV current and on the relative HV current measurement should be small, because the fraction of electrons captured by the oxygen should be nearly independent of the beam intensity.
As planned the beam was half-bunched and half-debunched, i.e. the first half of the spill was with synchrotron bunch structure and the second half was in the debunched mode, where the bunches were smoothed to a flat beam. Before the beamrun it was expected that this would not cause any problems, because the beam intensity in both modes should be identical. But it turned out that the measured HV current was much higher in the debunched mode than in the bunched mode (compare Figure 6.12). The reason for that are larger saturation effects caused by positive ion buildup and electrostatic shield in the LAr gaps when one bunch passes the detector in bunched mode compared to debunched mode. This is caused by the high number of particles hitting the detector at the same time during a bunch. In the debunched mode the same number of protons is distributed over a much larger time interval and so the particles can ionise the argon gradually. In this case, the ions from the previous ionisation would have already drifted away and positive ion buildup would be much less.
The problem for the luminosity measurement project is created by the different behaviour

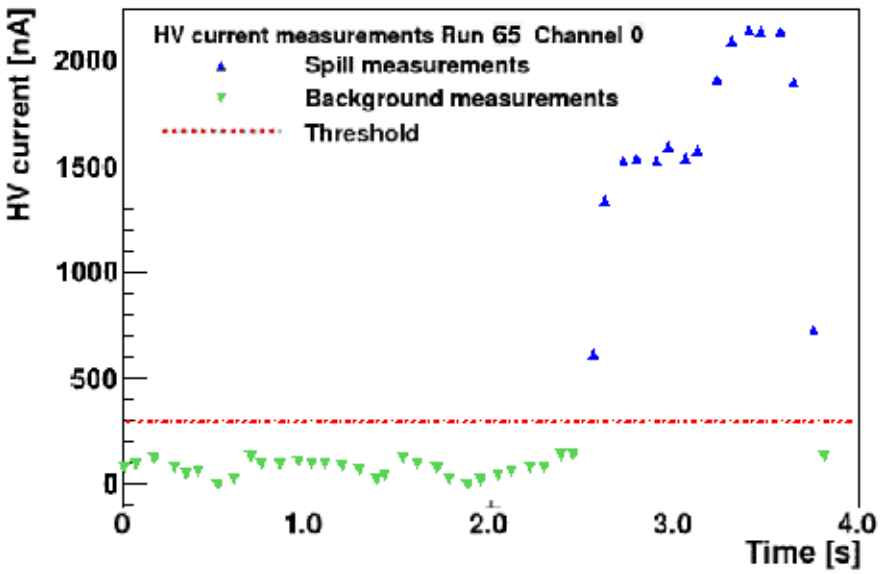

Figure 6.12: *HV current measurements of one spill of Run 65. Upward pointing triangles: measurements within the spill. Downward pointing triangles: background measurements (no spill). Dashed line: threshold to separate spills from background.*

of the HV current in bunched and debunched mode (as described above) and the fact that the ionisation chamber as the most important beam intensimeter provides only the integral over the whole spill with bunched and debunched mode together. In addition, the length of the bunched part and of the debunched part did not have to be constant. These circumstances did lead to a biased relation between the HV current and the measured beam intensity. After analysing the data it turned out that the data taken during the November run was not accurate enough for a precise comparison of the HV currents with the beam intensity, because of the problems described above. Furthermore, it was impossible to detect beam intensity variations between the bunched part and the debunched part of one spill. Such variations would influence the precision of the measurement, too. An example for the comparison of the FCALchick HV current with the beam intensity is given in Figure 6.13. The plots show the integrated HV current over one spill compared with the beam intensity provided by the ionisation chamber on a spill by spill basis. The details of the analysis of the HV current and the comparison with the beam intensity are described in Chapter 7. It is visible that a linear relation does not fit to the data very well. For this reason no detailed investigation of non-linearities between the HV current and the beam intensity was possible with the data taken in the November run.

The plan for the testbeam included a variation of the high voltage at the calorimeters and so the nominell voltage of 250 V was not applied to the FCALchick in every run. Since only the runs with 250 V were relevant for the luminosity measurement project, only these runs are listed in the run summary in Table 6.6.

It was possible to move the cryostats perpendicular to the beam line such that the beam could either be centered on the 250 µm side or the 100 µm side of the FCALchick. The nominal voltage of the 100 µm side was 100 V. When the beam was centered on the 100 µm side, 250 V were also applied to the module with 250 µm LAr gaps. Periods with different beam positions relative to the FCALchick have to be analysed separately. The reason for this is the fact that the particle flux which goes through the calorimeter and thus the HV current are depending on the position of the beam relative to the calorimeter. However the beam intensity as measured by the ionisation chamber is completely independent of that.

Run	Beam intensity [p/spill]	Duration [min:s]	FCALchick module centered on beam
59	$2.61 \cdot 10^7$	9:44	250 µm side
62	$2.28 \cdot 10^8$	11:03	250 µm side
65	$1.16 \cdot 10^9$	10:00	250 µm side
68	$2.43 \cdot 10^9$	9:25	250 µm side
75	$3.13 \cdot 10^9$	9:52	250 µm side
77-80	$2.31 \cdot 10^9$	100:00	100 µm side
81-87	$1.52 \cdot 10^8$	108:00	100 µm side
88-90	$4.57 \cdot 10^9$	80:00	100 µm side
91-93	$1.29 \cdot 10^{10}$	63:00	100 µm side
94-96	$3.48 \cdot 10^{10}$	55:00	100 µm side
97	$2.15 \cdot 10^{11}$	12:00	100 µm side

Table 6.6: *Runs taken during the November run with 250 V applied to the FCALchick 250 µm side.*

This means that every beam position variation relative to the cryostats would influence the

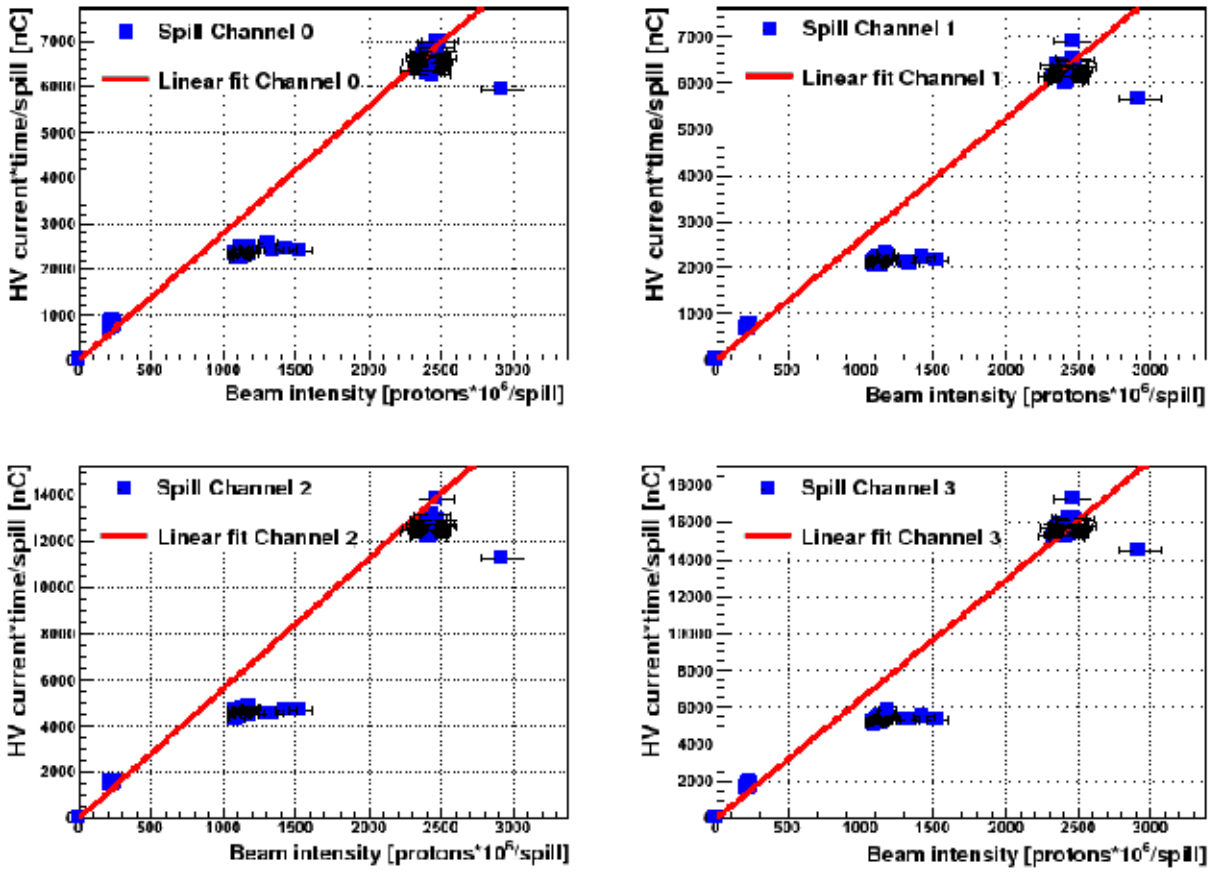

Figure 6.13: *Comparison of the FCALchick HV current with the beam intensity for Runs 62, 65, 68 with linear fit. Each plot shows the integrated HV current over one spill (y-axis) compared with the ionisation chamber data (x-axis) for one HV channel of the FCALchick 250 µm side on a spill by spill basis. A detailed explanation of the analysis is given in Chapter 7.*

comparison between the HV current and the beam intensity.
At lower intensities up to run 69 the scintillation counters S1, S2, and S3 were used for bunch triggering. From run 70 onwards the high angle counters S4, S5 and S6 continued the task of triggering. The signals of these counters were split: One wire went to 40 MHz ADCs for bunch trigger and writing intensity information into the Data Aquisition (DAQ) for each event. The other went to a shaper with 50 mV threshold and to a scaler. This information was used for an online intensity monitoring during the experiment and was saved independently of the DAQ for the whole spill. The scaler counted the signal in 4.096 ms time intervalls, but without amplitude measurement. With this scaler information it was not possible to discriminate the protons within one bunch and to measure the number of protons of this bunch in bunched mode, if using the counters in the beamline (S1, S2, S3). This means that only the number of bunches could be counted and no beam intensity measurement was possible in bunched mode, because for higher beam intensities only the number of protons per bunch was increased and the number of bunches within one spill was kept nearly constant.

The particle flux of scattered particles reaching the high angle counters S4, S5 and S6 is low enough so that an intensity measurement is possible and not disrupted by too large particle overlap. In debunched mode the protons are well enough separated so that a beam intensity measurement is possible also with the counters within the beam.
The information of the integrated intensity over each spill of the ionisation chamber and the shaped signal of the scintillation counters were saved independently of the DAQ and were later used as a reference for the HV currents.
A second beam run took place in April 2008. In this run a lot of things were improved. For example the seals at the cryostats were replaced and argon gas with higher purity was used. With these improvements it was possible to increase the purity of the liquid argon to an acceptable level of about 2 ppm. In addition, more attention was paid to the beam position relative to the calorimeters and possible fluctuations of the beam position itself. It is possible that such fluctuations happend during the November run, because no precise beam position information was saved for offline analysis.

The biggest advantage of the April run was that the machine was operating in bunched

Run	Beam intensity [p/spill]	Duration [min:s]	FCALchick module centered on beam	Cryostat position [mm]
152	$2.0 \cdot 10^7$	12:04	100 µm side	−6
160	$2.0 \cdot 10^7$	20:23	100 µm side	−6
161-162	$2.0 \cdot 10^7$	44:19	100 µm side	0
166	$2.4 \cdot 10^9$	23:21	100 µm side	−6
175-178	$2.3 \cdot 10^9$	62:00	100 µm side	−6
189	$1.6 \cdot 10^{11}$	13:25	250 µm side	+40
196-202	$2.0 \cdot 10^{10}$	107:00	250 µm side	+40
209-210	$2.0 \cdot 10^{10}$	34:20	250 µm side	+40
211-218	$2.0 \cdot 10^{10}$	80:00	100 µm side	+25
219	$2.0 \cdot 10^8$	12:17	100 µm side	+25
221	$2.0 \cdot 10^8$	12:09	100 µm side	+15
222	$2.0 \cdot 10^8$	12:27	100 µm side	+25
223	$1.6 \cdot 10^8$	11:58	100 µm side	+25
230	$1.3 \cdot 10^8$	12:16	250 µm side	+32.5
240	$2.5 \cdot 10^9$	12:00	250 µm side	+32.5
241	$5.3 \cdot 10^9$	12:07	250 µm side	+32.5
242	$8.5 \cdot 10^8$	12:13	250 µm side	+32.5
243	$5.0 \cdot 10^8$	10:03	250 µm side	+32.5
244	$5.0 \cdot 10^8$	11:27	250 µm side	+32.5

Table 6.7: *Runs taken in April with 250 V applied to the FCALchick 250 µm side.*

mode only, because the debunched mode could not be used for data taking as described in the following section. As explained above, there are indeed higher saturation effects in the liquid argon in bunched mode, but more important is that the beam structure was constant during the testbeam. This means that no disturbing effects caused by different calorimeter behaviour in bunched- and debunched mode (as during the November run as described above) could influence the measurement. In fact the data taking in April turned out to be much more suited for a detailed comparison with the beam intensity spill-by-spill. In Table

6.7 the data with 250 V applied to the FCAL 250 µm side taken during the April run is summarised. In addition the precise position of the FCALchick cryostat is given for each run relative to an expected zero value. The many cryostat position changes were done to center the cryostats to the beam position after possible beam position changes. Primarily the dataset from the April run was used for a detailed analysis. The third channel of the FCALchick 250 µm side was not working during the April run and so the ADC was switched to one channel of the 100 µm side. Especially the Runs 230 and 240-244 with a constant beam position turned out to be very useful for comparing the FCAL HV currents with the beam intensity.

6.7 Calorimeter Signal Readout in Protvino

For completion the readout of the calorimeter signals in Protvino is explained in the following. After the bunch trigger signal, the calorimeters were read out. Like in ATLAS they are operating with 40 MHz ADCs leading to 25 ns time intervalls. A fast flash memory always saved the last 256 time intervalls and after triggering the last 72 time intervalls were read out. In this timeframe of $72 \cdot 25$ ns $= 1800$ ns two events (equal to two bunches) could be read out. The DAQ needed about 10 ms for processing the data, collecting all other information (beam intensity, TDC information, slow control data) and write it to permanent storage before being ready for the next event. This means that only about 100 events or bunches out of approximately 10^6 bunches per second can be written out together with the corresponding beam intensity information. The debunched mode could not be used for data taking, because of the missing bunch trigger signal as explained above. This mode was only necessary for a parallel experiment the beam was shared with.

7 Analysis of Testbeam Data

7.1 Introduction

The goal of this thesis is to find out, whether it is feasible to obtain a relative measurement of the luminosity from a measurement of the FCAL1 HV currents. In fixed target experiments like the Protvino hilumi testbeams the luminosity is proportional to the beam intensity. Therefore the measured beam intensity is used here to compare it with the HV currents. It is necessary to proof that the HV currents depend on the luminosity linearly and to measure the amount of possible non-linearities.
As explained in Chapter 6, the ionisation chamber used at the Protvino hilumi testbeam runs is the only beam intensity monitor that gives a linear response over the whole relevant intensity range. Its data is therefore best suited for a comparison with the measured FCAL HV currents. The ionisation chamber measures the integrated intensity of individual spills and so the integrated intensity of every spill is available. The Dresden 4-channel HV current measurement device provides 10 measurements per second for each channel, yielding 12 HV current measurements per spill assuming a spill length of 1.2 s.

The first opportunity was to calculate an average current of these 12 measurements for every spill and compare this average with the beam intensity on a spill by spill basis. However the average depends not only on the integrated beam intensity, but also on the particular spill length and possible beam intensity distribution variations within the single spills (compare Figure 7.3). This can cause biased HV current averages at constant beam intensities and influence the results of the analysis.
For this reason it is decided to calculate the integral over the HV current of the whole spill. This integrated charge can then be compared with the integrated intensity on a spill by spill basis. This comparison would be independent of the individual spill length.

In the following the datasets and data formats used for the analysis are described. The definition of a spill in the HV current data and the calculation of the integral over the current of a spill is explained in the next sections. Furthermore, the comparison of this integrated HV current with the beam intensity is described.

7.2 Datasets and Data Format

During the beam runs the data was recorded in textfile format. Three datasets were used for the analysis:

- **The ionisation chamber** provided one beam intensity measurement, integrated over

one spill. Its data was recorded in the format given in Table 7.1. The timestamp of

Format	Day	Mon	dd	hh:mm:ss	Year	Beam intensity [p/spill]
Example	Sat	Apr	12	21:00:46	2008	$2.4738E+09$
	Sat	Apr	12	21:00:55	2008	$2.0913E+09$
	Sat	Apr	12	21:01:05	2008	$2.3405E+09$
	Sat	Apr	12	21:01:15	2008	$2.379E+09$
	Sat	Apr	12	21:01:24	2008	$2.2814E+09$

Table 7.1: *Data format of ionisation chamber data.*

the ionisation chamber data was synchronised with the DAQ timestamp.

- **The scintillation counter** signal was saved in time slices with a length of 4.096 ms. For each spill a window of 450 time slices was recorded, corresponding sums to about 1.8 s. The timestamp was the same as for the ionisation chamber data. Below the ADC counts of the time slices are following (see Table 7.2). The lengths of the time

Format	Example				
Timestamp	Sat	Apr	12	21:00:46	2008
Number in slices	450				
Counts in slice 1		0			
Counts in slice 2		1			
Counts in slice 3		1			
Counts in slice 4		3			
Counts in slice 5		6			
Counts in slice 6		23			
Counts in slice 7		60			
Counts in slice 8		155			
Counts in slice 9		2416			
.		3612			
.		3733			
.		3630			

Table 7.2: *Data format of scintillation counter data (some time slices of one spill).*

slices are well defined (4.096 ms), but the absolute precision of the timestamp was only 1 s as for the ionisation chamber data. The timestamp was obtained from the DAQ timeserver as well.

- **FCAL HV current data** The data format chosen for the Dresden HV current is given in Table 7.3. The four channels are defined by the numbers 0,1,2,3 and one ADC count corresponds to 1.2 nA. The timestamp included a slot for the milliseconds with a precision of 10 ms and was not connected to the DAQ timeserver. For this reason it had to be synchronised to the DAQ timestamp manually using the LabView program described in Chapter 6. This was possible with a precision of about ± 10 ms.

Format	Year.MM.dd	hh:mm:ss.mil,channel,	ADC counts
Example	2008.04.12	21:00:46.020,0,	2374
	2008.04.12	21:00:46.030,2,	2129
	2008.04.12	21:00:46.070,1,	2713
	2008.04.12	21:00:46.100,3,	3485
	2008.04.12	21:00:46.120,0,	2319
	2008.04.12	21:00:46.130,2,	2009

Table 7.3: *Data format of Dresden HV current data.*

7.3 Analysis of HV Current Data

The HV current measurements took place every 100 ms and no additional information was available, whether a measurement took place within a spill or not. For this reason it was necessary to separate the HV current measurements during a spill from those between two spills (electronic noise). For that purpose a current threshold was defined for every channel and every period with nearly constant background (measurements between two spills) individually. All measured currents above the threshold were assigned to a spill, whereas all currents below the threshold were assigned to dark current between two spills. The threshold was set closely above the noise-peak to remove as much as possible of the dark current and as few as possible of the signal (spill). Basically the Runs 230 and 240-244 of the April run are used for the following analysis. In the following all diagrams marked with channel 3 show the data of channel 6 of the 100 µm side (compare Figure 6.6), because the ADC was switched to that channel during the testbeam in april. Examples of the HV current distributions of these runs can be seen in Figures 7.1 and 7.2.
The large peak in all histograms corresponds to the noise currents seen during the time between spills. During Run 230 the beam intensity was only $1.3 \cdot 10^8$ p/spill and so the HV current within the spills was not much above the noise and is visible in the histograms as a second peak. In the histograms for the Runs 240-244 this second peak is not visible, because the beam intensity was between $5.0 \cdot 10^8$ p/spill and $5.3 \cdot 10^9$ p/spill and the HV current within the spills is outside the histogram range. The chosen thresholds based on these histograms are summarised in Table 7.4. These thresholds are only estimations and no uncertainties are given for them, because small variations of the thresholds do not influence the integral over the spills significantly. The HV current measurements of the four channels of one selected spill during Run 230 is given in Figure 7.3.

Run	Channel 0	Channel 1	Channel 2	Channel 3
230	470	100	400	80
240-244	600	150	460	70

Table 7.4: *Thresholds to separate the spills from the noise in nA.*

The threshold (horizontal line) was used to separate the measurements within a spill from those between two spills. At higher intensities this separation is much clearer as shown for a spill at an intensity of $5.3 \cdot 10^9$ p/spill in Figure 7.4.
The upward pointing triangles in Figures 7.3 and 7.4 were assigned to measurements within a spill and the downward pointing triangles were asigned to background measurements be-

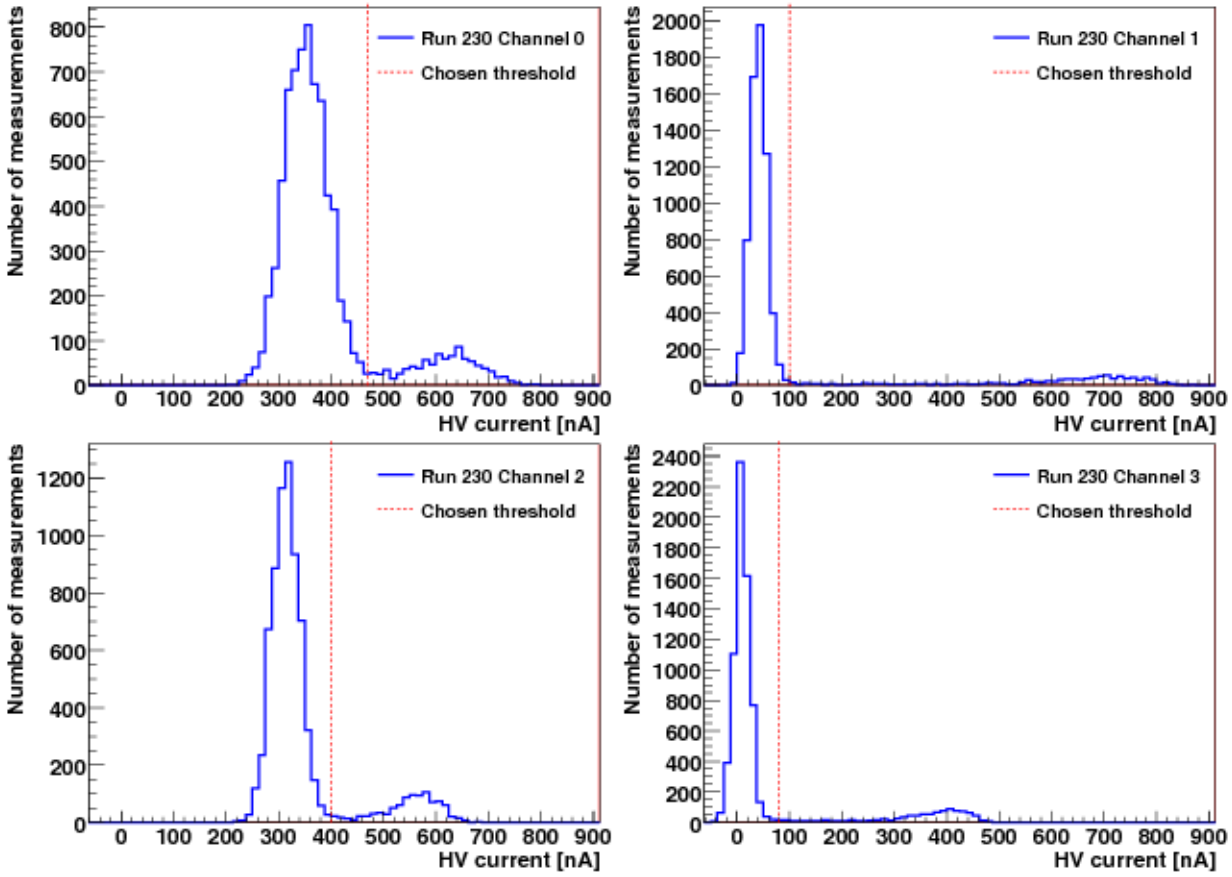

Figure 7.1: *HV current distributions of the four channels for Run 230.*

tween two spills.
After thus having defined a spill, it is possible to calculate the integral over the spill measurements. In the following the detailed calculation of this integral is explained.
The mean of the background measurements was calculated and subtracted from each measurement within the spill. Especially channels 0 and 2 showed dark currents above zero[1]. To obtain the integrated HV current for every spill in every channel, the integral for the upward pointing triangles was calculated for each channel independently as:

$$I = \sum_{i=1}^{n} (s_i - B) \cdot \left(\frac{t_i - t_{i-1}}{2} - \frac{t_{i+1} - t_i}{2}\right), \tag{7.1}$$

where s_i are the measurements within the spill, B the mean of the Background measurements before the considered spill, n the number of measurements within the spill and t the time of the corresponding measurement. The mean of the background was calculated as:

$$B = \frac{1}{m} \sum_{i=1}^{m} b_i, \tag{7.2}$$

[1]The reason for these might be ground loops or little short circuits in the HV connection or within the gaps themselves.

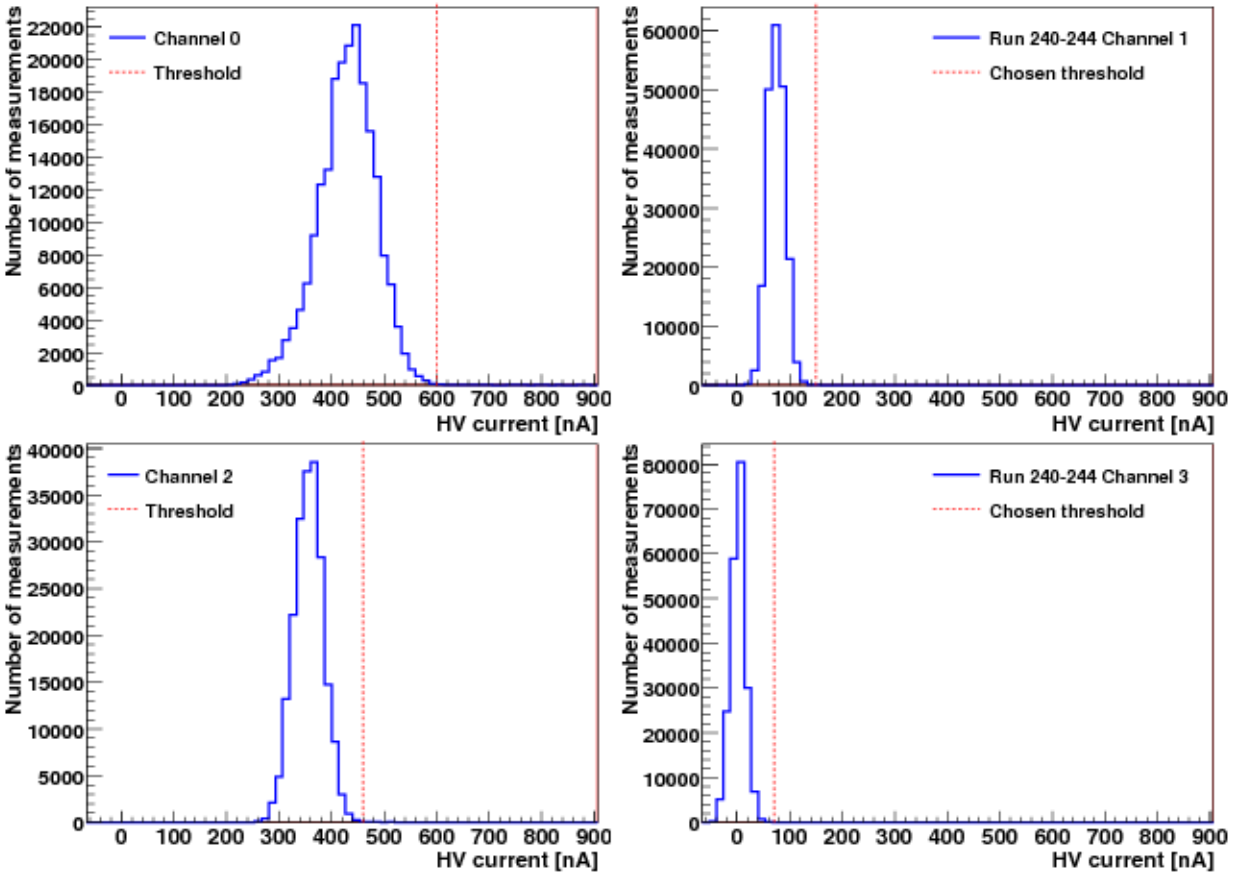

Figure 7.2: *HV current distributions of the four channels for Runs 240-244.*

with b being a background measurement between two spills and m is the number of such measurements.
To obtain the uncertainty of the integral (7.1) it is necessary to know the uncertainty of each single measurement. The uncertainty coming from digitalisation is only about 1.2 nA and can be neglected. Therefore the major contibution to the uncertainty of a single measurement is the electronic noise. This noise can be calculated out of the fluctuations of the measurements. The first possibility was to calculate the fluctuations of the spill measurements from these measurements themselves as described in the following.
If d is the time between two measurements, the uncertainty on the integrated HV current was calculated by

$$\triangle I = \sqrt{[(n \cdot d \cdot \triangle s)^2 + (n \cdot d \cdot \triangle b)^2]} = \sqrt{d^2 \cdot n^2[(\triangle s)^2 + (\triangle b)^2]}. \tag{7.3}$$

Here $\triangle s$ is the uncertainty on one measurement within a spill and $\triangle b$ the uncertainty on a background measurement. $\triangle b$ was calculated using all background measurements between the considered and the previous spill via:

$$\triangle b = \frac{1}{\sqrt{m \cdot (m-1)}} \sqrt{\sum_{i=1}^{m} (B - b_i)^2}. \tag{7.4}$$

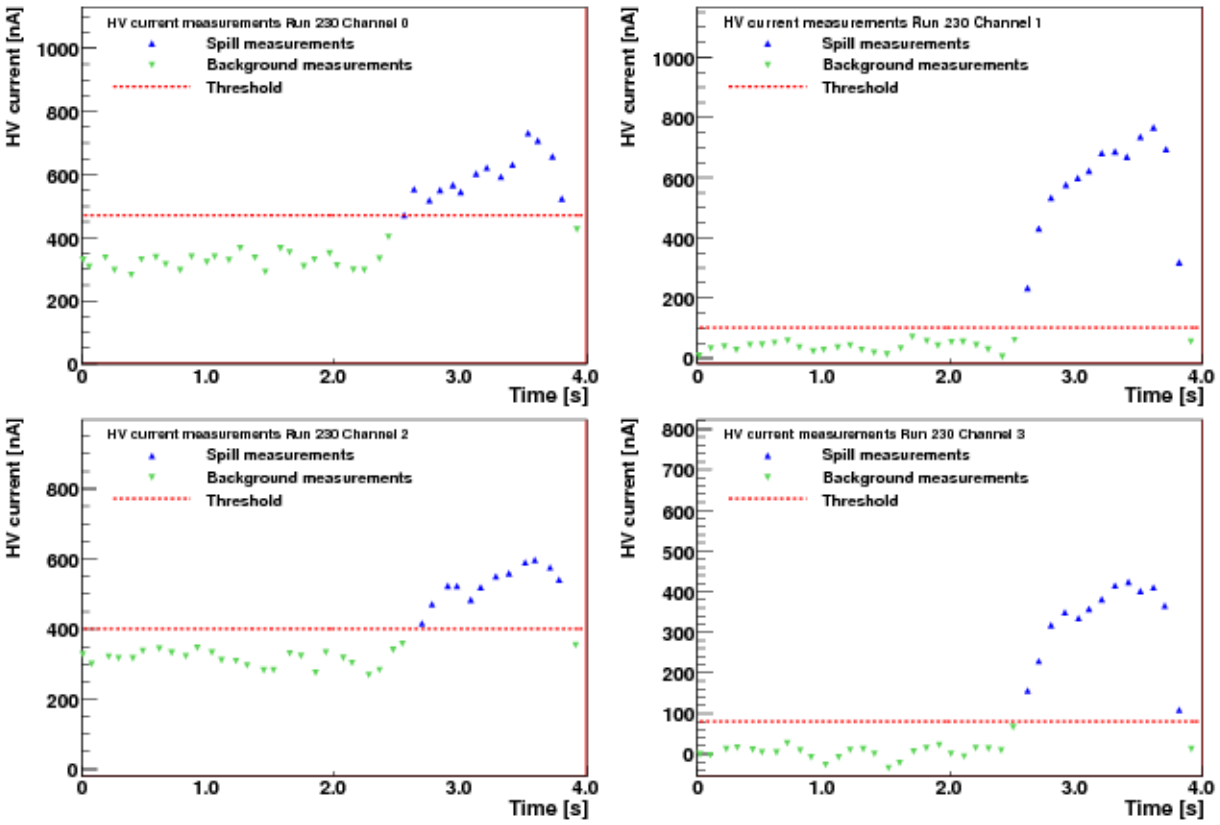

Figure 7.3: *HV current measurements of one spill of Run 230. Upward pointing triangles: measurements within the spill. Downward pointing triangles: background measurements (no spill). Horizontal line: threshold to separate spills from background.*

Calculating the uncertainty on a spill measurement, would be possible by doing it in a similar way using

$$\triangle s = \frac{1}{\sqrt{n \cdot (n-1)}} \sqrt{\sum_{i=1}^{n} (S - s_i)^2}, \tag{7.5}$$

with S being the mean of the spill measurements calculated the same way as in Equation (7.2):

$$S = \frac{1}{n} \sum_{i=1}^{n} s_i. \tag{7.6}$$

However, this method would lead to larger than pure statistical fluctuations, as the current during a spill is not constant. This is caused by using a low pass filter and possible beam intensity variations within the spill. Both of these effects would lead to much bigger fluctuations of the spill measurements, as it would be the case from statistical fluctuations only.

Instead the uncertainty of one spill measurement was taken from the background measurements as well, corresponding to $\triangle s = \triangle b$. This is sensible, because there should be no

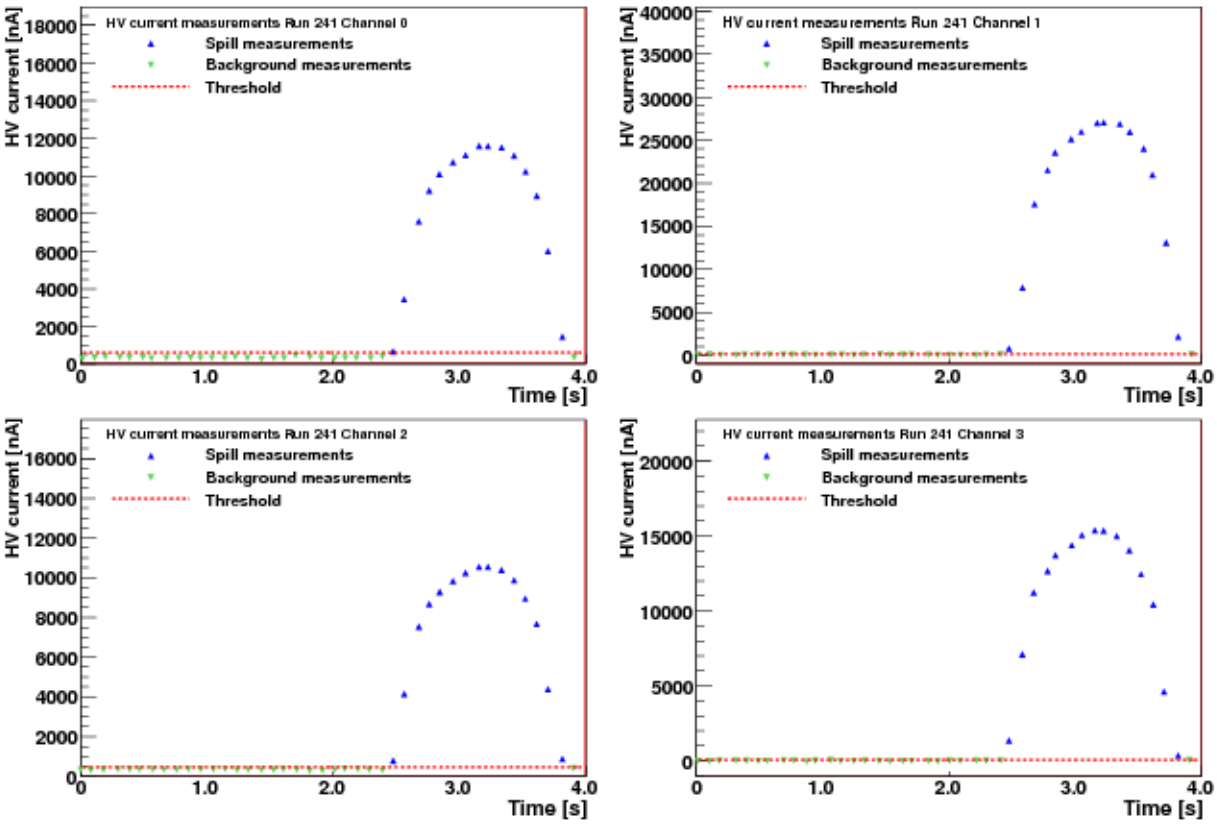

Figure 7.4: *HV current measurements of one spill of Run 241. Upward pointing triangles: measurements within the spill. Downward pointing triangles: background measurements (no spill). Horizontal line: threshold to separate spills from background.*

difference in the electronic noise between spill measurements and background measurements. For this reason Equation (7.3) becomes simplified to:

$$\triangle I = \sqrt{d^2 \cdot n^2[(\triangle b)^2 + (\triangle b)^2]} = \sqrt{d^2 \cdot n^2 \cdot 2(\triangle b)^2} = \sqrt{2} \cdot d \cdot n \cdot \triangle b. \tag{7.7}$$

7.4 Comparison with Ionisation Chamber Data

The integrated current was then compared with the ionisation chamber data on a spill by spill basis. A time window of 3 s around a spill located in the HV currents was used to find the corresponding spill in the ionisation chamber data. This way, possible displacements in the timestamps were compensated and matching the wrong spills were excluded, because of the much larger spill-to-spill distance of about 9.5 s.
The integral calculated in Equation (7.1) and the corresponding uncertainty calculated in Equation (7.7) were used to compare the measured HV current with the beam intensity measured by the ionisation chamber. Using this data without attention of possible complications leads to a preliminary result for the four channels shown in Figure 7.5.
The relative uncertainty on the ionisation chamber data was roughly estimated to be 5 %. Figure 7.5 shows that there are not all measurements near a linear curve present in the

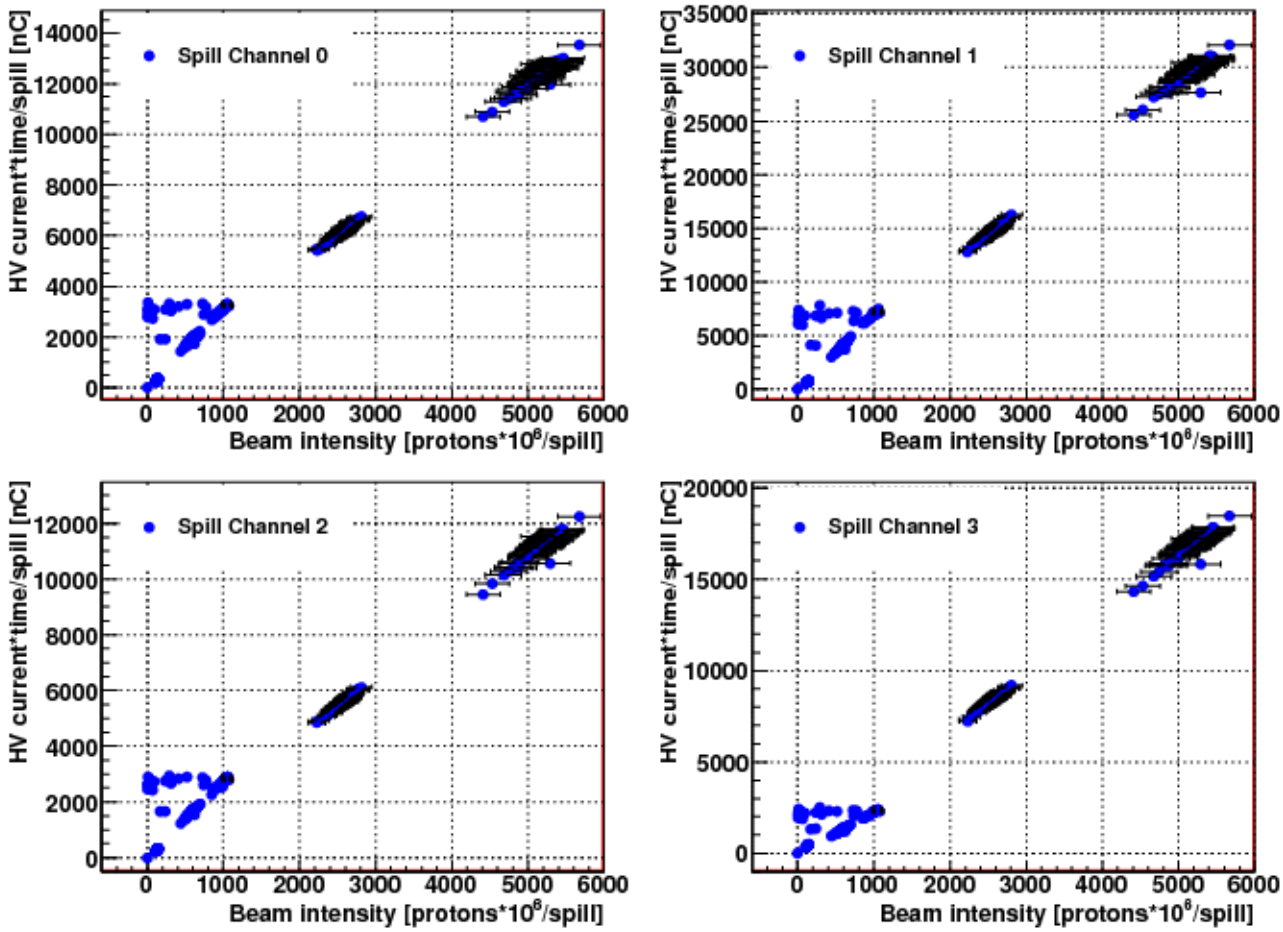

Figure 7.5: *HV current vs. beam intensity for Runs 230, 240-244.*

relationship between HV currents and the beam intensity. Thus, it is necessary to check out some possible sources of non-linearities like mismeasurements (in the HV currents or in the beam intensity data) or beam position variations.

7.5 Consideration of Beam Position Variations

The position of the FCAL cryostat was kept constant during the Runs 230 and 240-244, but it cannot be excluded that the beam position varied during this period. To investigate this possibility, the integrated currents of the four channels were compared among themselves. A significant change of the ratio between two channels would indicate a shift of the beam position. All six possible ratios were analysed: channel 0 to 1 and channel 2 to 3 in the horizontal, channel 0 to 2 and channel 1 to 3 in the vertical and channel 0 to 3 and channel 1 to 2 for the diagonal directions. In Figure 7.6 the detailed channel layout is given.

The ratios between the different channels for a whole period (Run 230 and Runs 240-244) are shown in Figure 7.7. Two clearly seperated peaks are identifiable except for the ratio between channel 2 and channel 0. This leads to the assumption of two different beam positions with a possible beam position shift perpendicular to the axis defined by channel 2

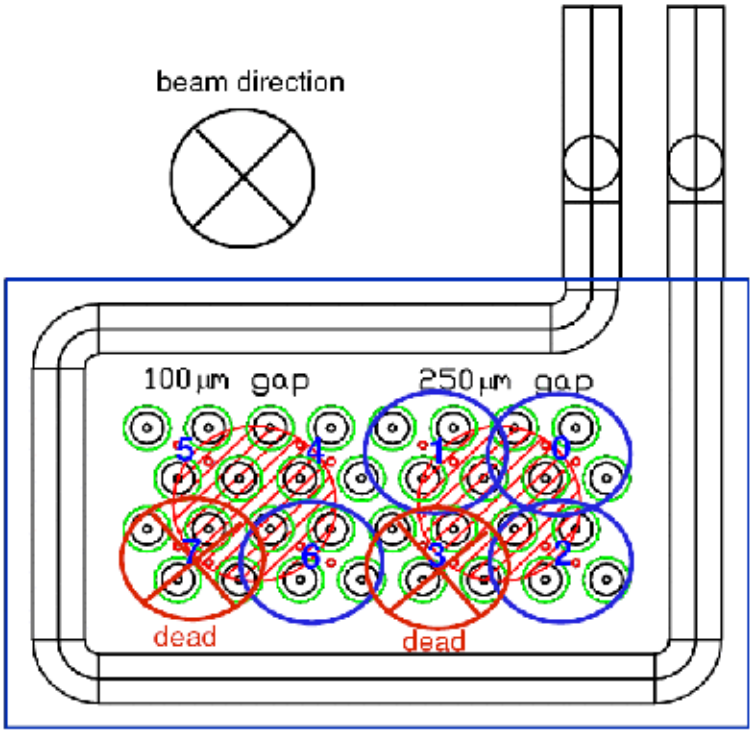

Figure 7.6: *Channel layout for the April 2008 Run. Channels surrounded by blue circles were connected to the Dresden four channel HV current measurement. Channels with red cross were not working during the April Run.*

and channel 0. In fact there was a period of nearly 5 hours without a beam between Run 241 and Run 242 because of a beam loss in the hilumi beam extraction line. After that the beam had to be accelerated again and it is possible that the beam position was different after it. To verify this assumption, the data is divided into the part before and after the beam loss. The ratios for the first (Runs 230,240,241) and for the second period (Runs 242-244) can be seen in Figure 7.8 and in Figure 7.9 respectively.

Each of the two peaks in Figure 7.7 corresponds to one period and the beam position is nearly constant within one period. It is impossible to calculate the difference in the HV current of the four channels for different beam positions, because the exact profile of the proton beam after the primary absorber is unknown. This means that the two time intervals have to be analysed seperately, as the HV current changes during a beam position shift even if the beam intensity is constant.

The separate comparison between the HV current and the beam intensity for the two periods with constant beam position is shown in Figure 7.19 for the Runs 230, 240, 241 and in Figure 7.23 the Runs 242-244.

The integrated HV current of the spills in the first period shows good proportionality to the beam intensity. In the second period a lot of spills are close to a straight line going through (0,0), but many spills show a constant HV current with changing beam intensity. The reason for this could be single mismeasurements of the ionisation chamber.

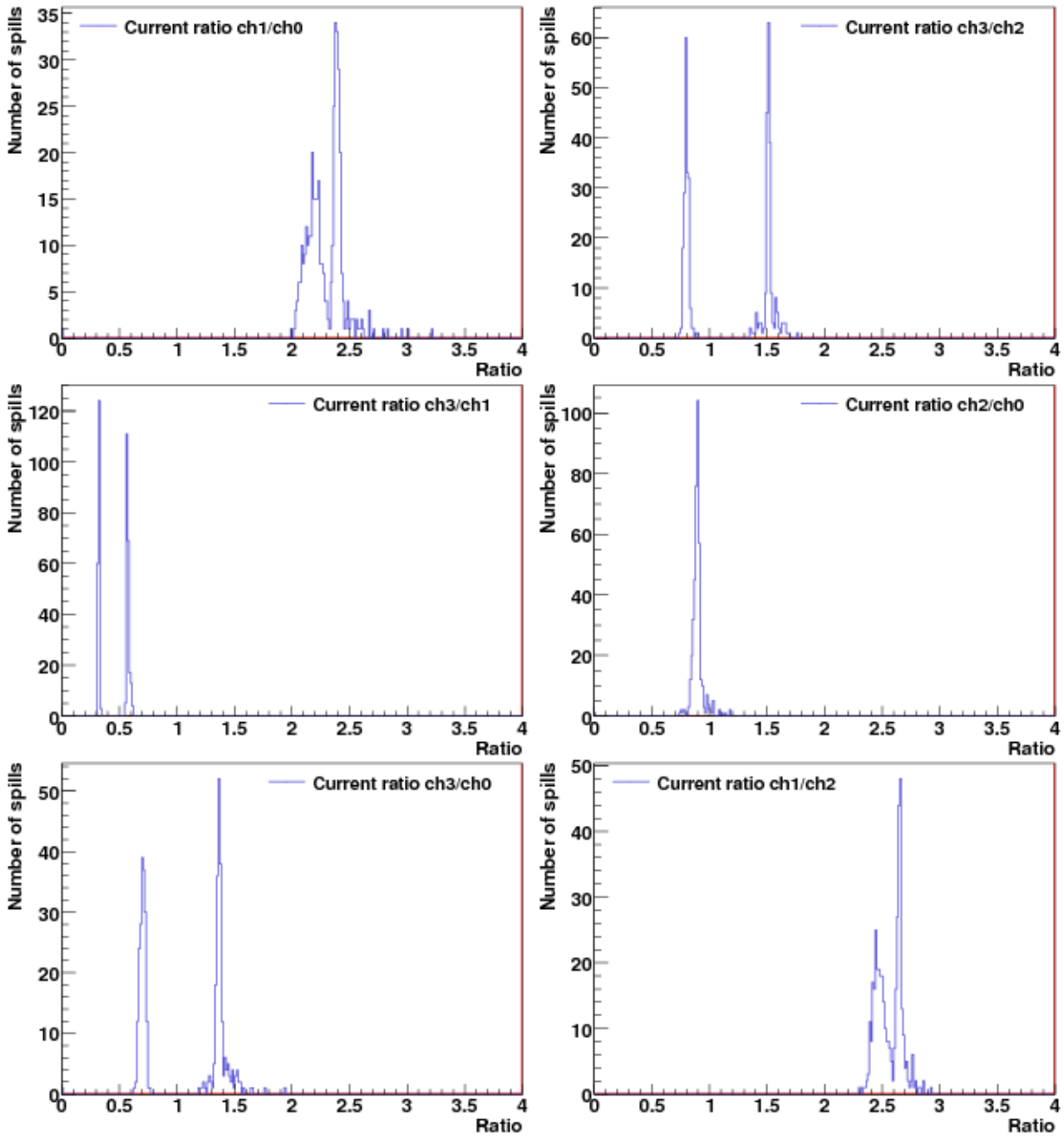

Figure 7.7: *Ratios of HV current for Runs 230, 240-244. The integrated HV current over one spill is used to calculate the ratios.*

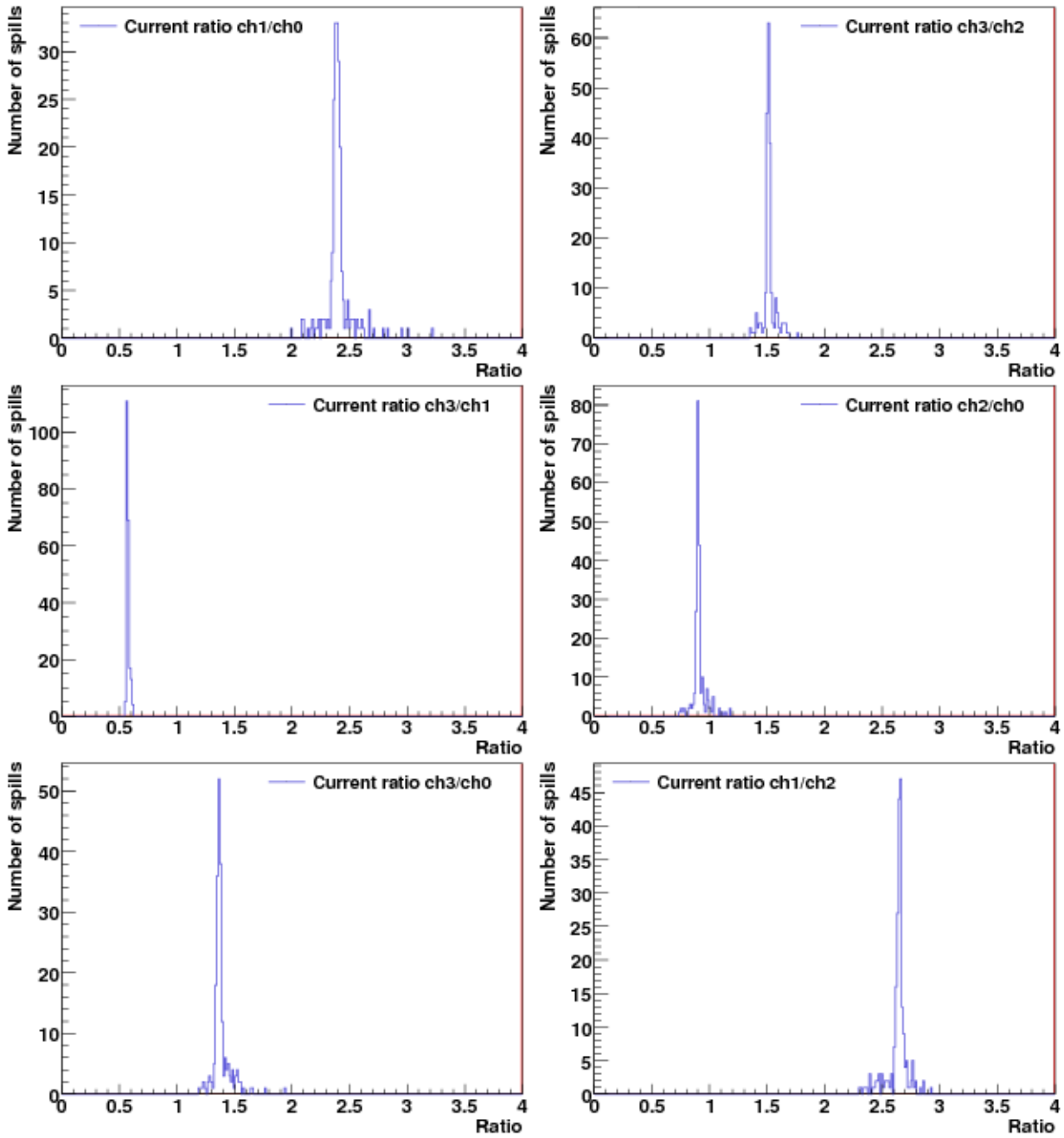

Figure 7.8: *Ratios of Runs 230, 240, 241. The integrated HV current over one spill is used to calculate the ratios.*

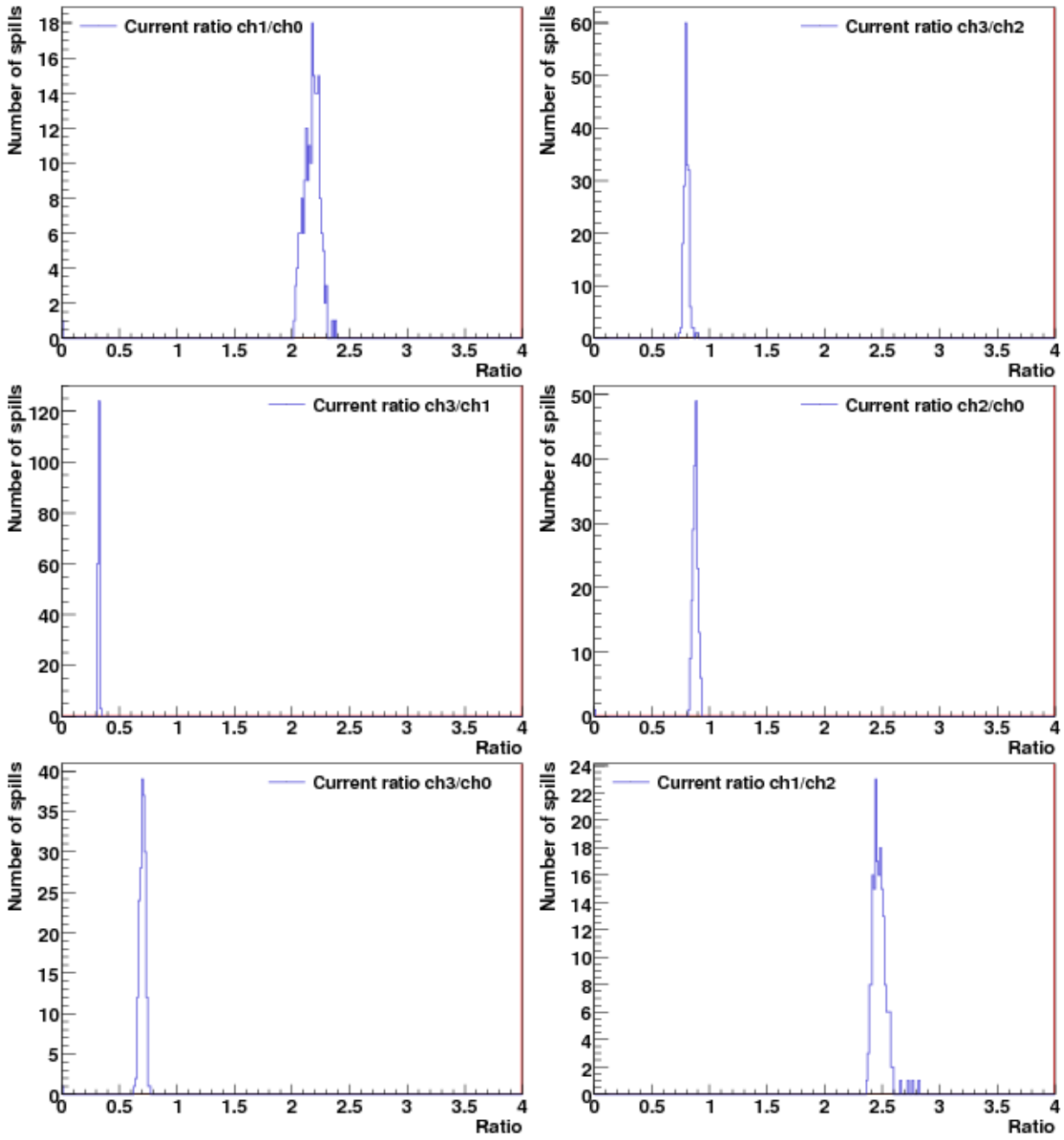

Figure 7.9: *Ratios of Runs 242, 243, 244. The integrated HV current over one spill is used to calculate the ratios.*

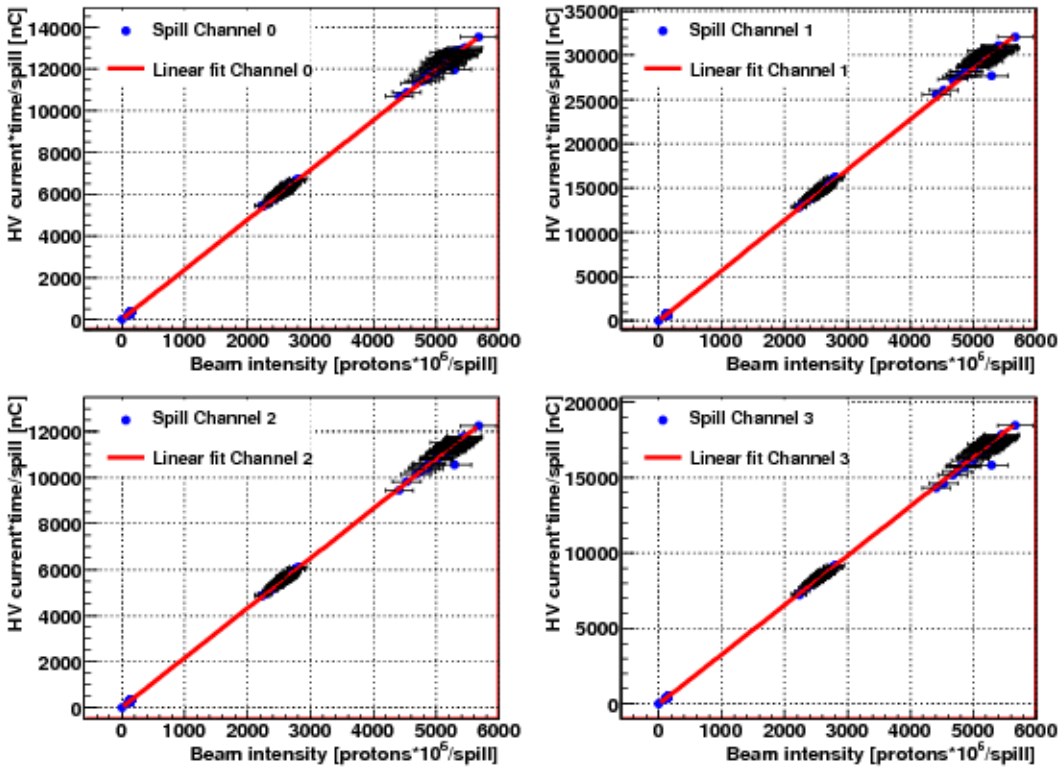

Figure 7.10: *HV current vs. beam intensity with linear fit for the Runs 230, 240, 241.*

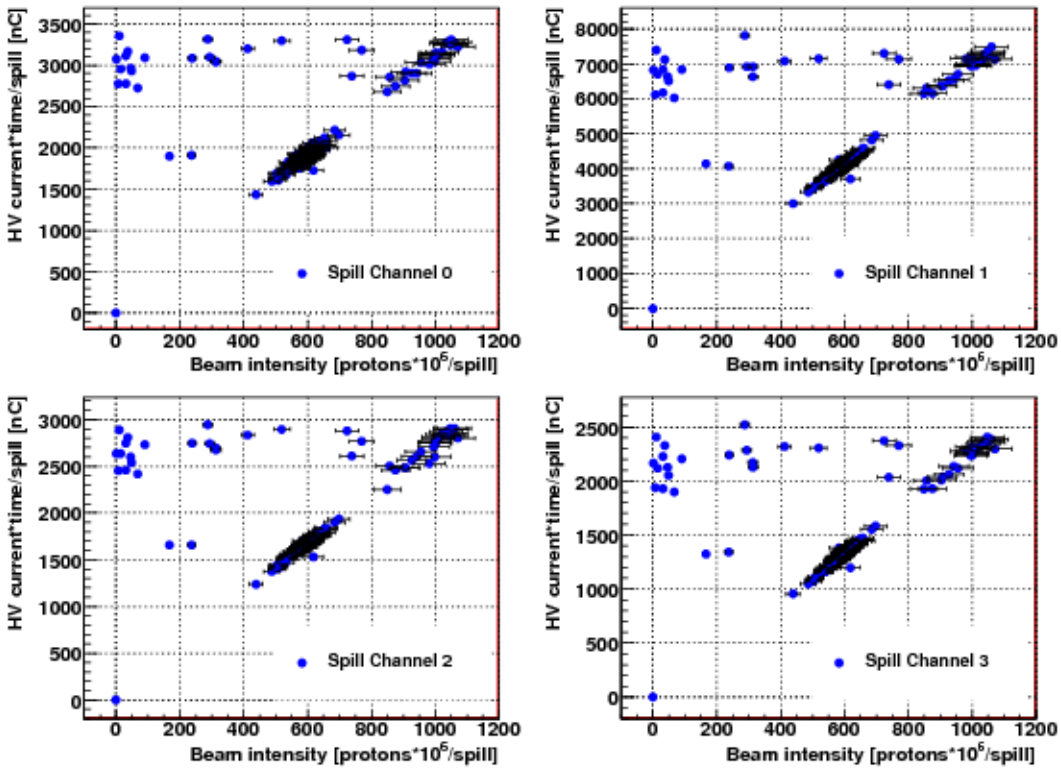

Figure 7.11: *HV current vs. beam intensity for the Runs 242-244.*

7.6 Bad Spill Rejection using Scintillation Counter Data

To reject these mismeasurements, the ionisation chamber data was compared with the recorded data of the scintillation counters, the second beam intensity measurement device used in Protvino. In the April run the large angle counter S5 was connected to the shaper and to the scaler (as explained in Chapter 6) to record its data in time slices with a length of 4.096 ms. Its data can only be compared with the ionisation chamber data on a run-by-run basis, as the scintillation counter response does not depend linearly on the beam intensity over large intensity ranges. At first the ionisation chamber output was compared with the scintillation counter output for Run 242, the run with the most suspected mismeasurements. For this comparison the counts of the scintillation counter were integrated over one spill. The result for Run 242 can be seen in Figure 7.12.

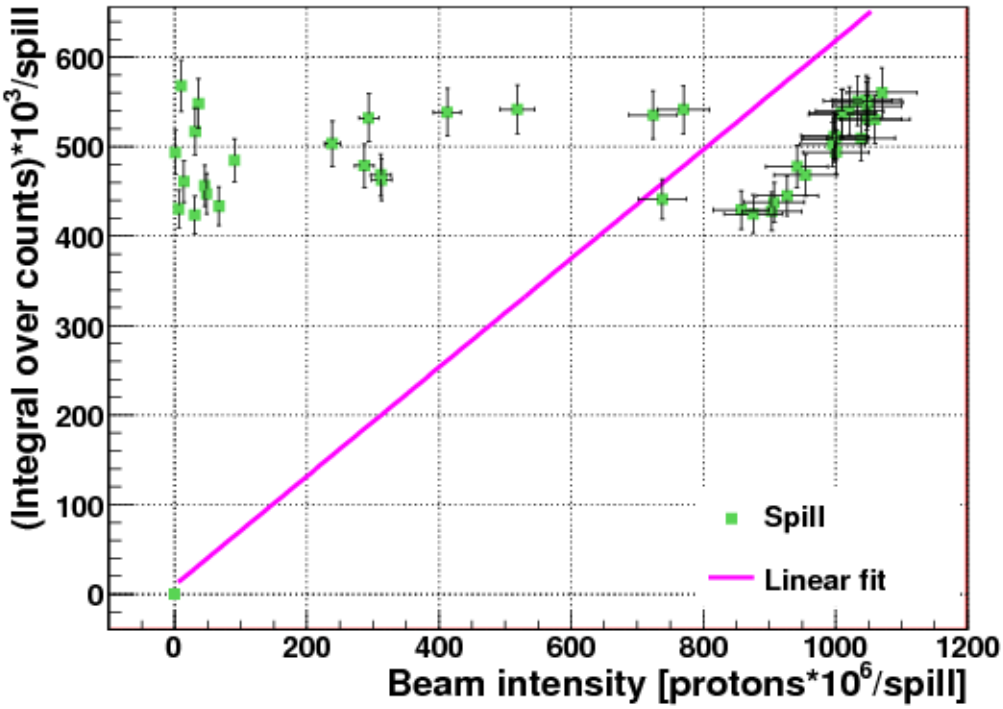

Figure 7.12: *Scintillation counter counts vs. beam intensity with linear fit for Run 242.*

That confirms the assumption that the low intensity measured in the spills with high HV current in Figure 7.23 really originates from mismeasurements of the ionisation chamber. The next step was to reject these bad spills with a recursive algorithm: A linear fit is applied as indicated in Figure 7.12. The spill with the highest χ^2 contribution is discarded and the fit redone. This procedure is repeated as long as the variation of the fit χ^2 becomes smaller. To find this point χ^2 of the linear fit was plotted against the number of spills remaining using the described algorithm. χ^2 of the linear fit as a function of the number of remaining spills is shown in Figure 7.13.

χ^2 of the fit becomes smaller, if the spill with the highest χ^2 contribution is discarded. If all spills with a relatively high distance to the fit curve in Figure 7.12 are removed, the χ^2

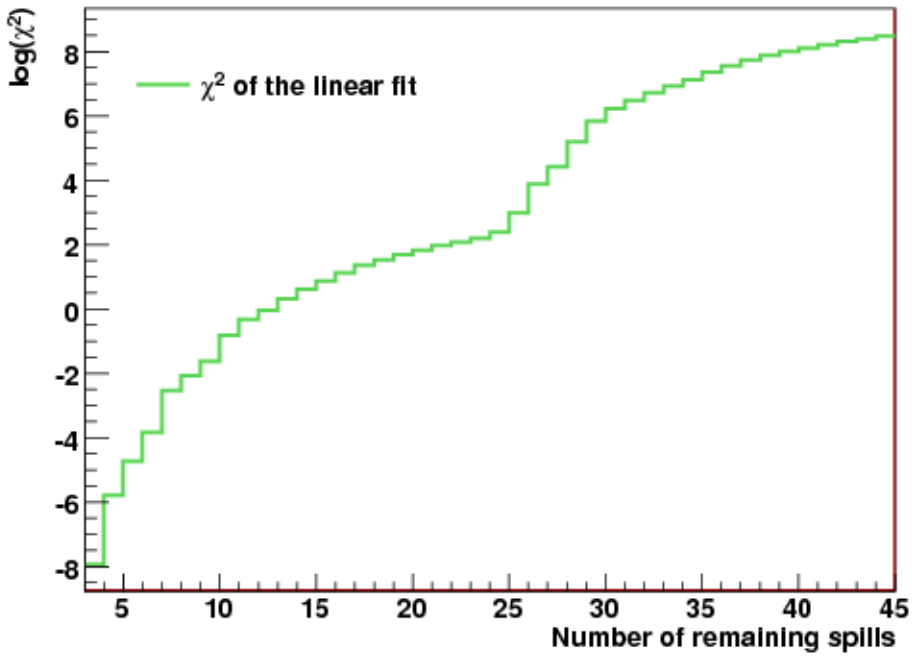

Figure 7.13: *Fit χ^2 in dependence on the number of remaining spills after bad spill removal as described in the text for Run 242 with logarithmic y-axis.*

in dependence on the number of remaining spills (curve in Figure 7.13) becomes more flat. The reason for this is that only spills near the fit function with low χ^2 contribution are left and only these spills can be removed in this case.
The intention is to calculate this number of remaining spills and to keep all spills which are still remaining at this point, because these would be nearly on a linear curve going through (0,0). This point is defined by the inflexion point of the first derivative of the curve in Figure 7.13. To get this point, the χ^2 curve was fit with a fourth order polynomial (P4) because of two inflexion points of the distribution. The first and second derivative was then calculated for P4 and the maximum of the second derivative would be the number of spills remaining, where the variation of χ^2 becomes smaller. The fit polynomial and its first and second derivatives can be seen in the Figures 7.14, 7.15 and 7.16.

The maximum is located at 23.9 remaining spills. For this reason the 24 spills remaining after using the recursive algorithm were kept. Figure 7.17 shows the ionisation chamber output versus the output of the scintillation counter for Run 242 after removing the bad spills.

For Runs 243 and 244 only one bad spill had to be rejected in each case. The comparison of the integrated HV current with the ionisation chamber data without the rejected spills for the second period (Runs 242-244) is shown in Figure 7.18. Here it can be seen that the spills rejected by comparing the ionisation chamber data with the scintillation counter data were really mismeasurements of the ionisation chamber and that the HV current measurement was working correctly. Nevertheless, these spills cannot be included into the analysis, because no correct beam intensity measurement is available for them.

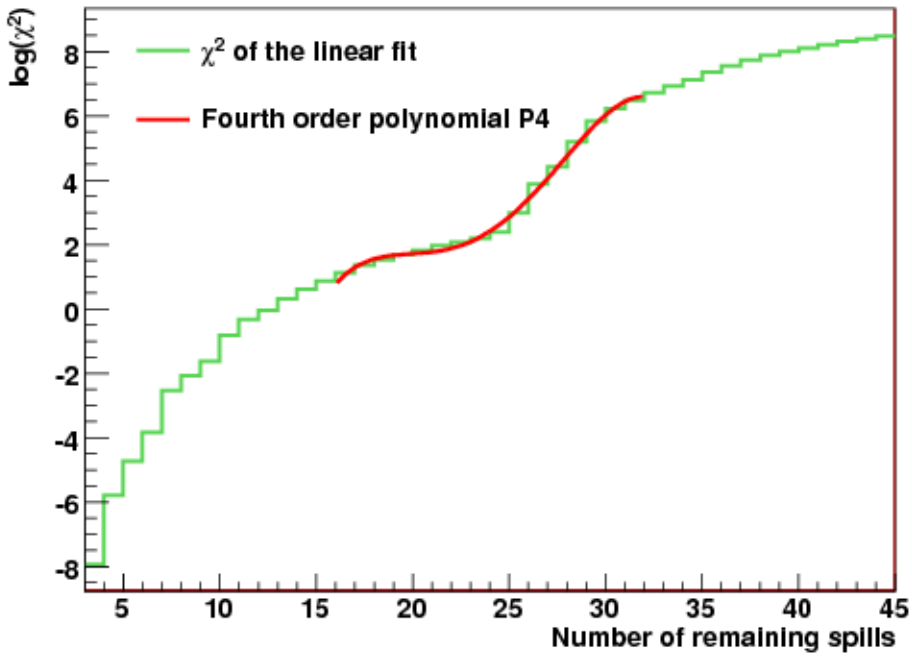

Figure 7.14: χ^2 *vs. remaining spills for run 242 with fit.*

After the removal of bad spills, the second period together with the first period (Runs 230-241, compare Figure 7.19) can be used for a detailed analysis of possible non-linearities between the FCAL HV current and the beam intensity.

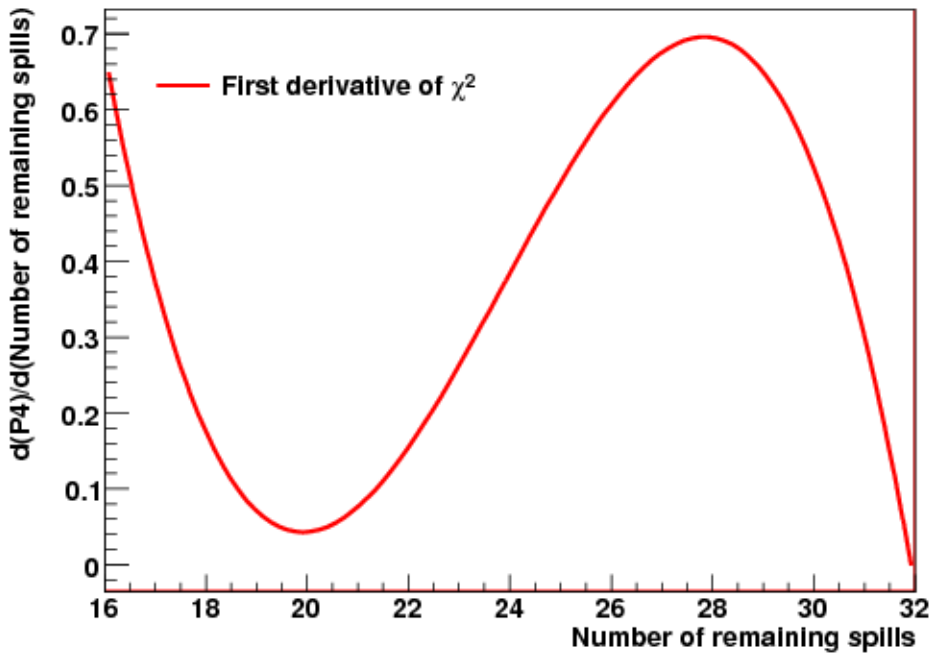

Figure 7.15: *First derivative of fitted polynomial P4.*

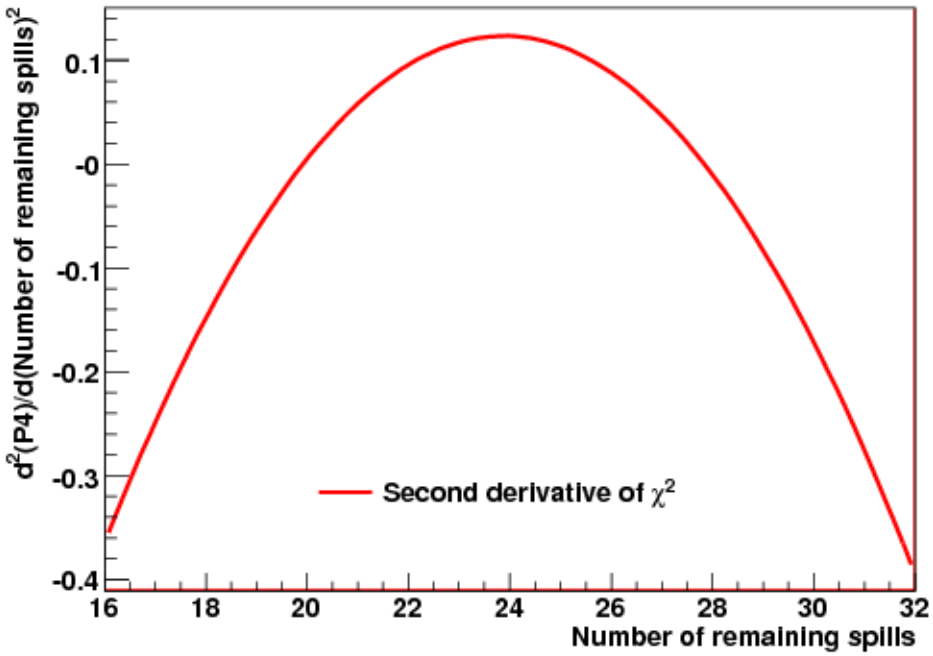

Figure 7.16: *Second derivative of fitted polynomial P4.*

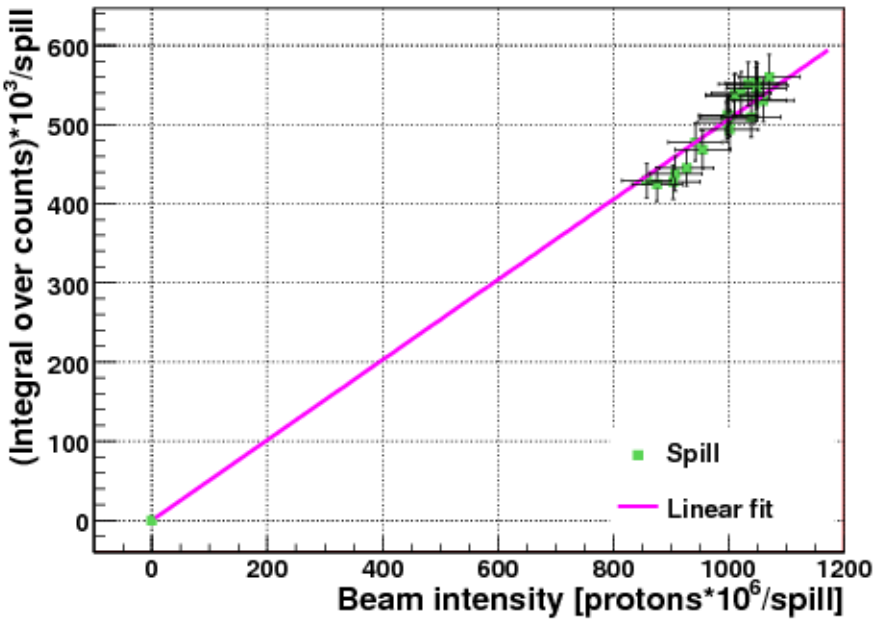

Figure 7.17: *Scintillation counter counts vs. beam intensity for Run 242 without rejected spills.*

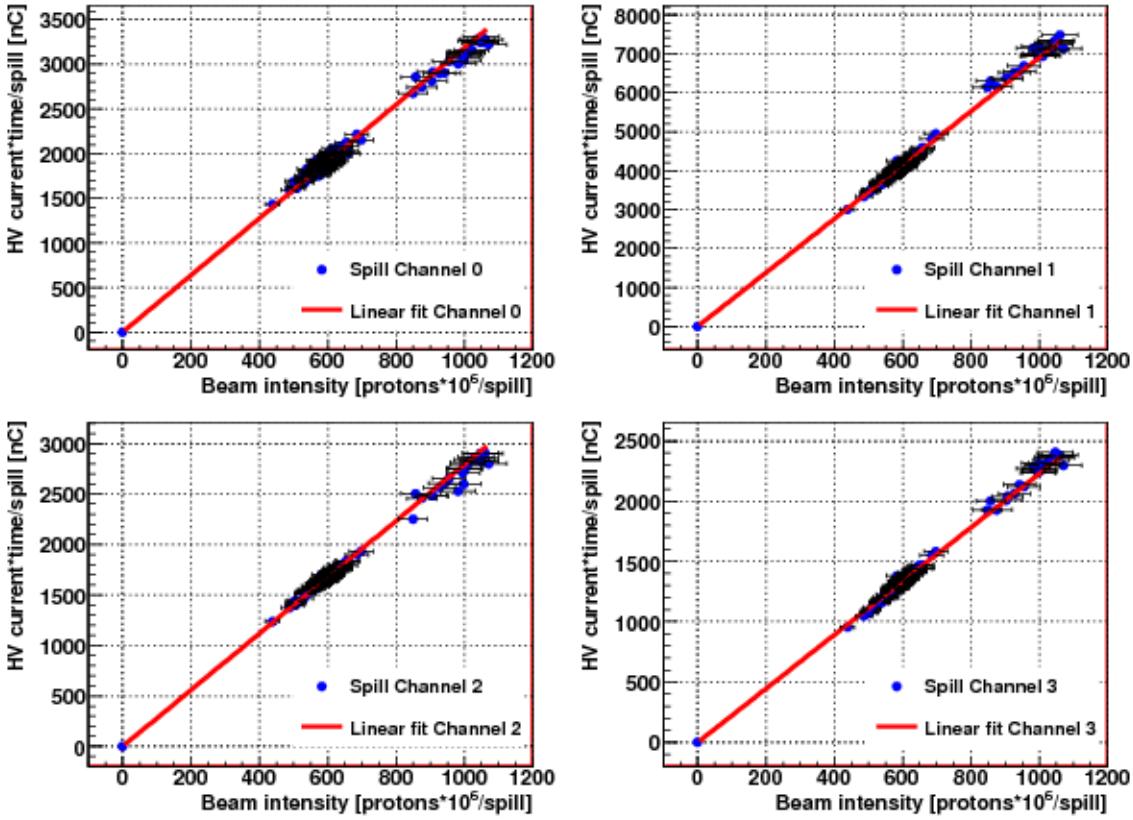

Figure 7.18: *HV current vs. beam intensity for Runs 242-244 without rejected spills.*

7.7 Investigation of Non-Linearities

To investigate possible non-linearities between the HV current and the beam intensity, the data as shown in Figures 7.19 and 7.18 was fit using a non-linear function. In first order all possible non-linearities can be approximated by a quadratic contribution. A second order polynomial was used for the fit and the fitted relation between the HV current I and the beam intensity X is:

$$I/(\mathrm{nC}) = P_0 + P_1 \cdot X/(10^6\mathrm{p/spill}) + \mathrm{P}_2 \cdot (\mathrm{X}/10^6\mathrm{p/spill})^2, \tag{7.8}$$

with P_0 being the constant part, P_1 the linear part and P_2 the quadratic part. The non-linearity f of the HV current can be calculated as:

$$f = \frac{P_2 \cdot (X/10^6\mathrm{p/spill})^2}{P_1 \cdot X/(10^6\mathrm{p/spill})} = \frac{P_2}{P_1} \cdot X/(10^6\mathrm{p/spill}). \tag{7.9}$$

Here the constant part P_0 can be neglected. As it can be seen the non-linear fraction depends linearly on the beam intensity X. The parameters of the fits for the first and the second period are given in Table 7.5. Here the quadratic contribution term is given for $X = 10^9$ p/spill. This corresponds to the nominal LHC luminosity of about 10^{34} cm^{-2} s^{-1} (see Table 6.4). The fit parameters in the lines "Sum(0,1,2)" were taken out of a combined fit, in which the HV current is summed over the channels 0,1 and 2. These are the channels with 250 µm LAr gaps, whereas the channel 3 ADC was connected to channel 6 of the 100 µm side. Therefore only the first three channels are of interest for this analysis. By summing the HV currents of three channels, statistical fluctuations and possible beam position fluctuations with small amplitudes can be reduced even more.
Using the sum gives a non-linearity of 0.38 ± 0.17 % for the first period and 0.58 ± 2.57 % for the second period for a beam intensity of 10^9 p/spill. The major contribution on the uncertainty of the non-linear fraction is the uncertainty of P_2. For this reason only the uncertainty of P_2 is considered and the uncertainty of P_1 is neglected in the calculation for the uncertainty of the non-linear fraction. Noticeable are the low χ^2s compared to the degrees of freedom (DoF) of the fits in Table 7.5. This leads to the assumption that the 5% uncertainty on the ionisation chamber data was a too conservative estimation.
Therefore a smaller uncertainty of 1.25% was used for the ionisation chamber to obtain a χ^2/DoF of about one. It can be assumed that the uncertainty on the integrated HV current is calculated correctly and the smaller uncertainty on the ionisation chamber data is more realistic. The fits were repeated with this uncertainty and the results are summarised in Table 7.6. The smaller ionisation chamber uncertainty also leads to lower uncertainties in the quadratic fractions of the fits. This way the non-linar fraction of the HV current is 0.26 ± 0.05 % for the first period and 0.59 ± 0.65 % for the second period, when using the sum of the channels 0 to 2.
The reason for the larger uncertainty in the second period is the smaller beam intensity range from about $5 \cdot 10^8$ p/spill to $1 \cdot 10^9$ p/spill. Compared to this the first period covers a beam intensity range from about $1 \cdot 10^8$ p/spill to $5 \cdot 10^9$ p/spill and therefore the uncertainty on the non-linear part is smaller.
The plots with the non-linear fits and ionisation chamber uncertainties of 1.25% are given

Period	Channel	P_0	P_1	P_2	$\triangle P_2$
First	0	-0.58	2.35	$-1.04 \cdot 10^{-5}$	$0.49 \cdot 10^{-5}$
	1	-0.23	5.63	$2.36 \cdot 10^{-5}$	$0.98 \cdot 10^{-5}$
	2	-0.27	2.16	$0.00 \cdot 10^{-5}$	$0.42 \cdot 10^{-5}$
	3	-0.11	3.29	$-0.49 \cdot 10^{-5}$	$0.56 \cdot 10^{-5}$
	Sum(0,1,2)	-0.12	10.12	$0.39 \cdot 10^{-5}$	$0.18 \cdot 10^{-5}$
Second	0	0.00	3.30	$-1.78 \cdot 10^{-4}$	$0.79 \cdot 10^{-4}$
	1	0.00	6.69	$3.22 \cdot 10^{-4}$	$1.91 \cdot 10^{-4}$
	2	0.00	2.89	$-1.51 \cdot 10^{-4}$	$0.68 \cdot 10^{-4}$
	3	0.01	2.14	$1.34 \cdot 10^{-4}$	$0.64 \cdot 10^{-4}$
	Sum(0,1,2)	0.00	12.93	$-0.75 \cdot 10^{-4}$	$3.33 \cdot 10^{-4}$

Period	Channel	$\chi^2(DoF)$	P_2/P_1	$(\triangle P_2)/P_1$	$P_2/P_1 \cdot 1000 \cdot$ $\cdot (10^6\text{p/spill})$
First	0	103(217)	$4.40 \cdot 10^{-6}$	$2.10 \cdot 10^{-6}$	$0.44\% \pm 0.21\%$
	1	19(217)	$4.19 \cdot 10^{-6}$	$1.74 \cdot 10^{-6}$	$0.42\% \pm 0.17\%$
	2	61(217)	$-0.00 \cdot 10^{-6}$	$1.92 \cdot 10^{-6}$	$0.00\% \pm 0.19\%$
	3	18(217)	$-1.48 \cdot 10^{-6}$	$1.71 \cdot 10^{-6}$	$0.15\% \pm 0.17\%$
	Sum(0,1,2)	23(217)	$3.84 \cdot 10^{-6}$	$1.74 \cdot 10^{-6}$	$\mathbf{0.38\% \pm 0.17\%}$
Second	0	40(161)	$-5.39 \cdot 10^{-5}$	$2.38 \cdot 10^{-5}$	$5.39\% \pm 2.38\%$
	1	11(161)	$4.82 \cdot 10^{-5}$	$2.85 \cdot 10^{-5}$	$4.82\% \pm 2.85\%$
	2	14(161)	$-5.23 \cdot 10^{-5}$	$2.36 \cdot 10^{-5}$	$5.23\% \pm 2.36\%$
	3	13(161)	$6.27 \cdot 10^{-5}$	$2.97 \cdot 10^{-5}$	$6.27\% \pm 2.97\%$
	Sum(0,1,2)	7(161)	$-0.58 \cdot 10^{-5}$	$2.57 \cdot 10^{-5}$	$\mathbf{0.58\% \pm 2.57\%}$

Table 7.5: *Fit parameters of the non-linear fits for the Runs 230 and 240-244 with assumed 5% uncertainty of the ionisation chamber data. The factor* 1000 *in the last column is for obtaining a beam intensity of (*10^9p/spill*) which is equal to the nominal LHC luminosity .*

in the Figures 7.19 and 7.23. The plot in Figure 7.19 zoomed in on Run 230 with a beam intensity of approximately $1 \cdot 10^8$ p/spill can be seen in Figure 7.21. In addition, the plots with the HV current summed over the channels 0, 1 and 2 for the two periods and zoomed in on Run 230 are given in the Figures 7.20, 7.22 and 7.24.

Period	Channel	P_0	P_1	P_2	$\triangle P_2$
First	0	-2.38	2.40	$0.00 \cdot 10^{-5}$	$0.18 \cdot 10^{-5}$
	1	-2.94	5.65	$1.71 \cdot 10^{-5}$	$0.29 \cdot 10^{-5}$
	2	-0.92	2.17	$-0.19 \cdot 10^{-5}$	$0.15 \cdot 10^{-5}$
	3	-0.90	3.29	$-0.63 \cdot 10^{-5}$	$0.19 \cdot 10^{-5}$
	Sum(0,1,2)	-1.35	10.17	$2.60 \cdot 10^{-5}$	$5.43 \cdot 10^{-5}$
Second	0	-0.01	3.30	$-1.90 \cdot 10^{-4}$	$0.22 \cdot 10^{-4}$
	1	-0.01	6.69	$3.22 \cdot 10^{-4}$	$0.48 \cdot 10^{-4}$
	2	-0.02	2.89	$-1.54 \cdot 10^{-4}$	$0.18 \cdot 10^{-4}$
	3	-0.16	2.14	$1.29 \cdot 10^{-4}$	$0.16 \cdot 10^{-4}$
	Sum(0,1,2)	0.00	12.93	$-0.76 \cdot 10^{-4}$	$0.84 \cdot 10^{-4}$

Period	Channel	$\chi^2(DoF)$	P_2/P_1	$(\triangle P_2)/P_1$	$P_2/P_1 \cdot 1000 \cdot$ $\cdot (p \cdot 10^6/spill)$
First	0	309(217)	$-0.01 \cdot 10^{-6}$	$0.74 \cdot 10^{-6}$	$0.00\% \pm 0.07\%$
	1	248(217)	$3.03 \cdot 10^{-6}$	$0.52 \cdot 10^{-6}$	$0.30\% \pm 0.05\%$
	2	217(217)	$-0.87 \cdot 10^{-6}$	$0.71 \cdot 10^{-6}$	$0.09\% \pm 0.07\%$
	3	175(217)	$-1.91 \cdot 10^{-6}$	$0.59 \cdot 10^{-6}$	$0.19\% \pm 0.06\%$
	Sum(0,1,2)	226(217)	$2.55 \cdot 10^{-6}$	$0.53 \cdot 10^{-6}$	$\mathbf{0.26\% \pm 0.05\%}$
Second	0	432(161)	$-5.73 \cdot 10^{-5}$	$0.66 \cdot 10^{-5}$	$5.73\% \pm 0.66\%$
	1	174(161)	$4.81 \cdot 10^{-5}$	$0.72 \cdot 10^{-5}$	$4.81\% \pm 0.72\%$
	2	191(161)	$-5.31 \cdot 10^{-5}$	$0.63 \cdot 10^{-5}$	$5.31\% \pm 0.63\%$
	3	191(161)	$6.03 \cdot 10^{-5}$	$0.76 \cdot 10^{-5}$	$6.03\% \pm 0.76\%$
	Sum(0,1,2)	115(161)	$-0.59 \cdot 10^{-5}$	$6.51 \cdot 10^{-5}$	$\mathbf{0.59\% \pm 0.65\%}$

Table 7.6: *Fit parameters of non-linear fit for the Runs 230 and 240-244 with 1.25% uncertainty on ionisation chamber data. The factor* 1000 *in the last column is for obtaining a beam intensity of (*10^9p/spill*) which is equal to the nominal LHC luminosity .*

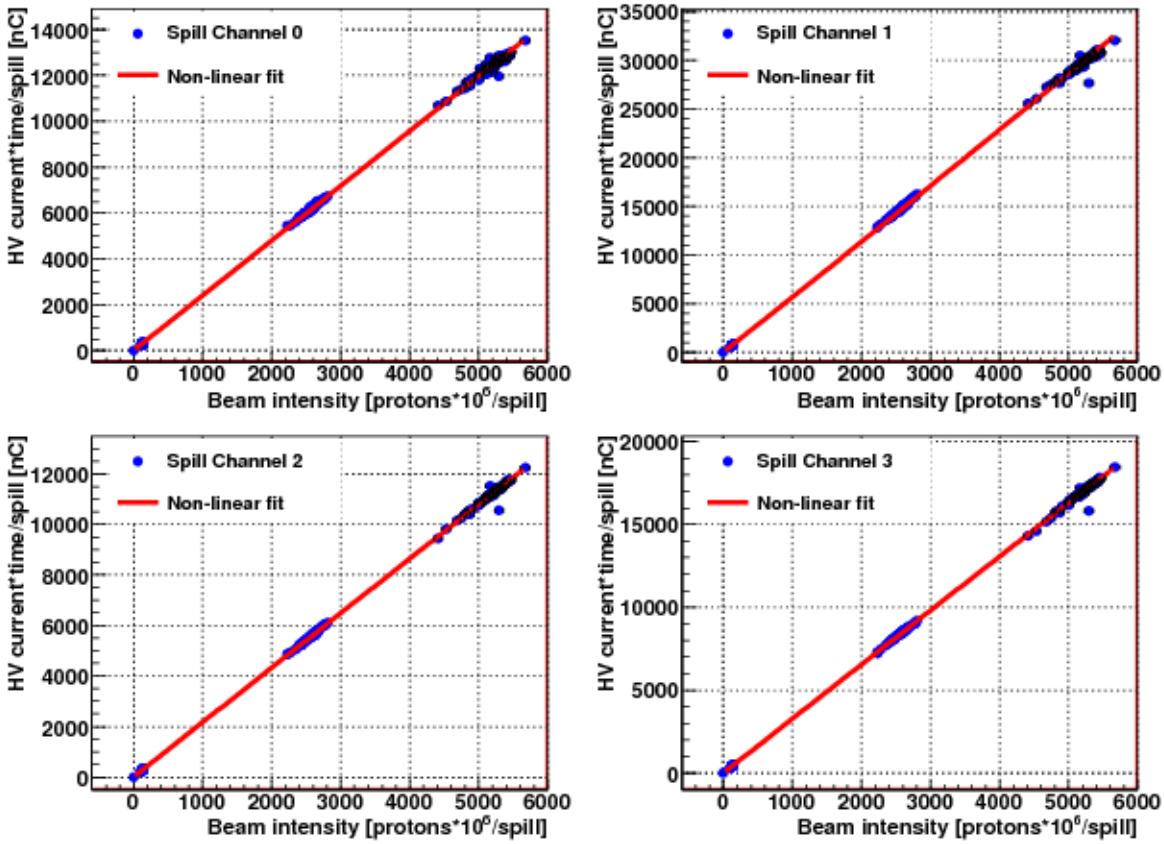

Figure 7.19: *HV current vs. beam intensity for Runs 230, 240, 241 with non-linear fit and 1.25% uncertainty of the ionisation chamber data.*

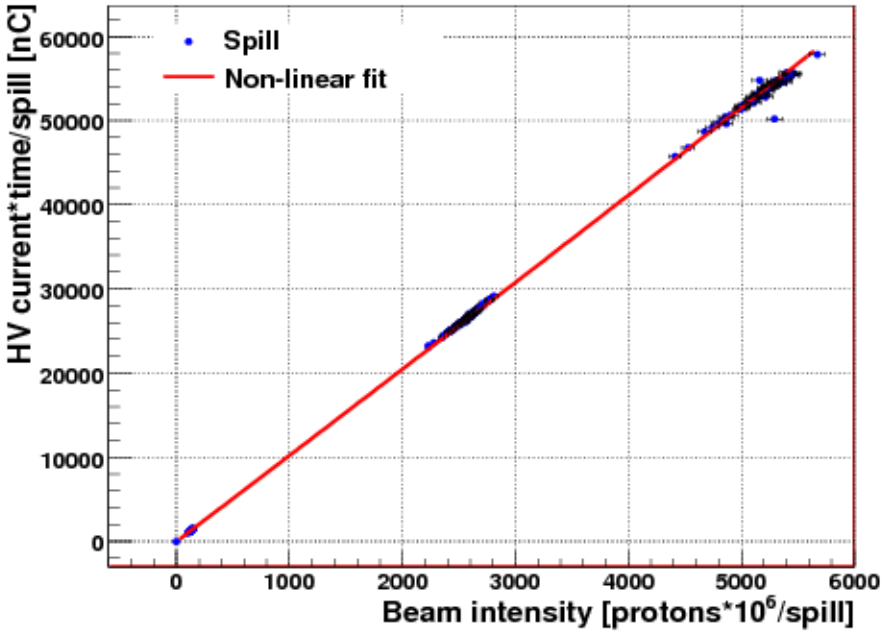

Figure 7.20: *HV current summed over channels 0-2 vs. beam intensity for Runs 230, 240, 241 with non-linear fit and 1.25% uncertainty of the ionisation chamber data.*

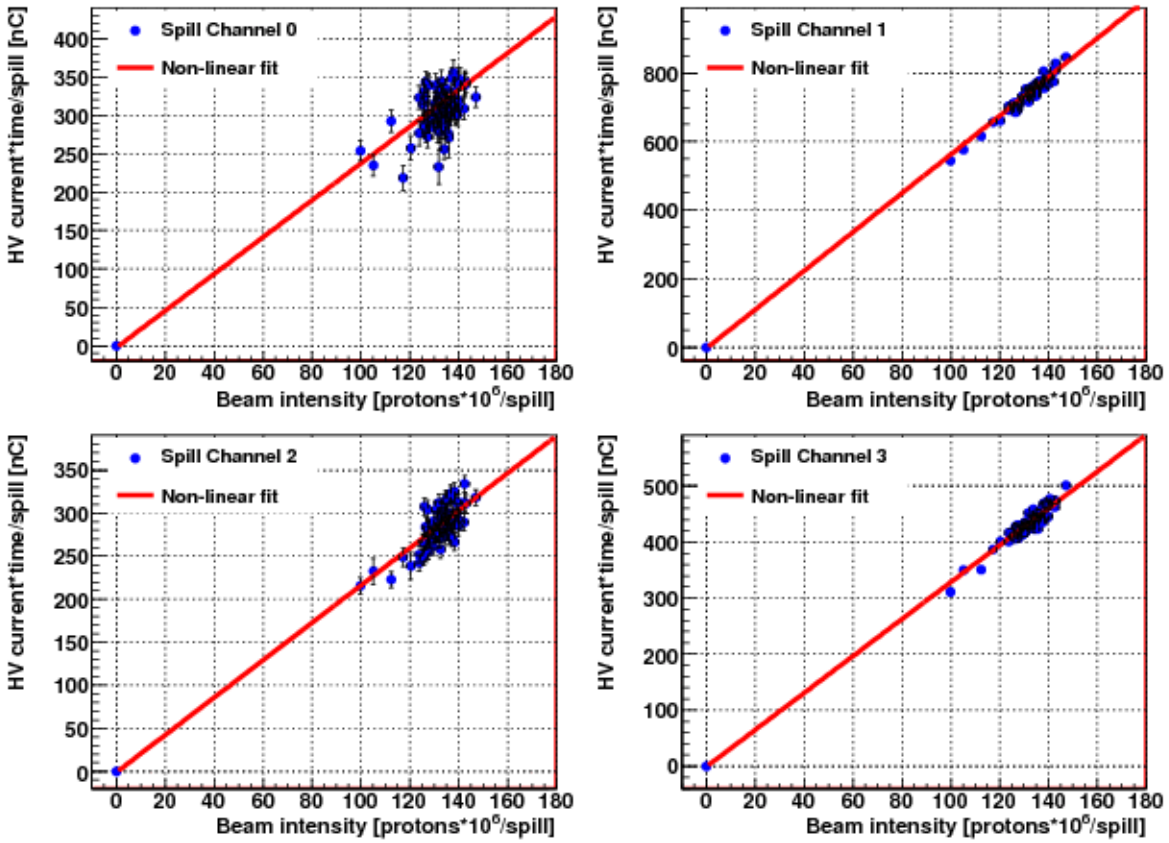

Figure 7.21: *HV current vs. beam intensity zoomed in on Run 230 with non-linear fit and 1.25% uncertainty of the ionisation chamber data.*

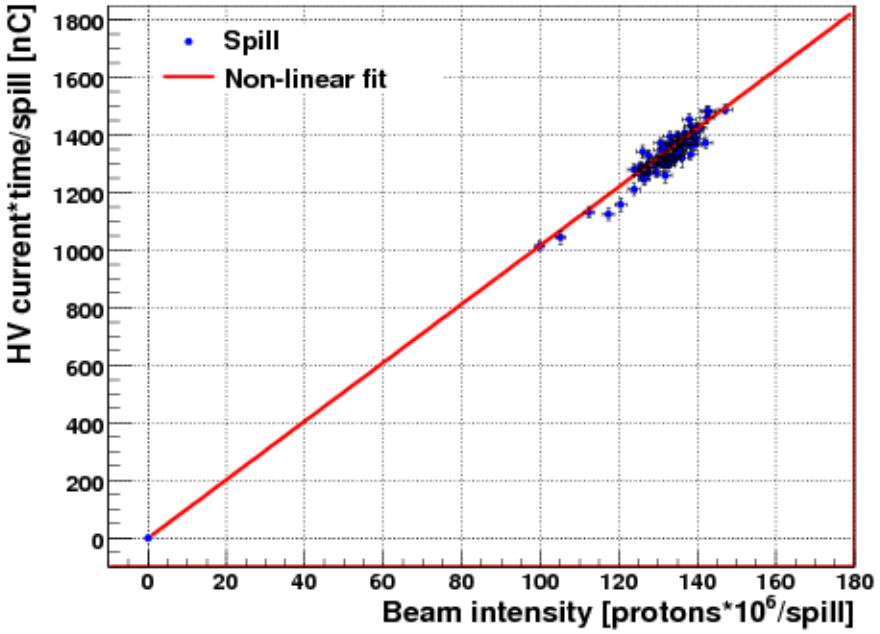

Figure 7.22: *HV current summed over channels 0-2 vs. beam intensity zoomed in on Run 230 with non-linear fit and 1.25% uncertainty of the ionisation chamber data.*

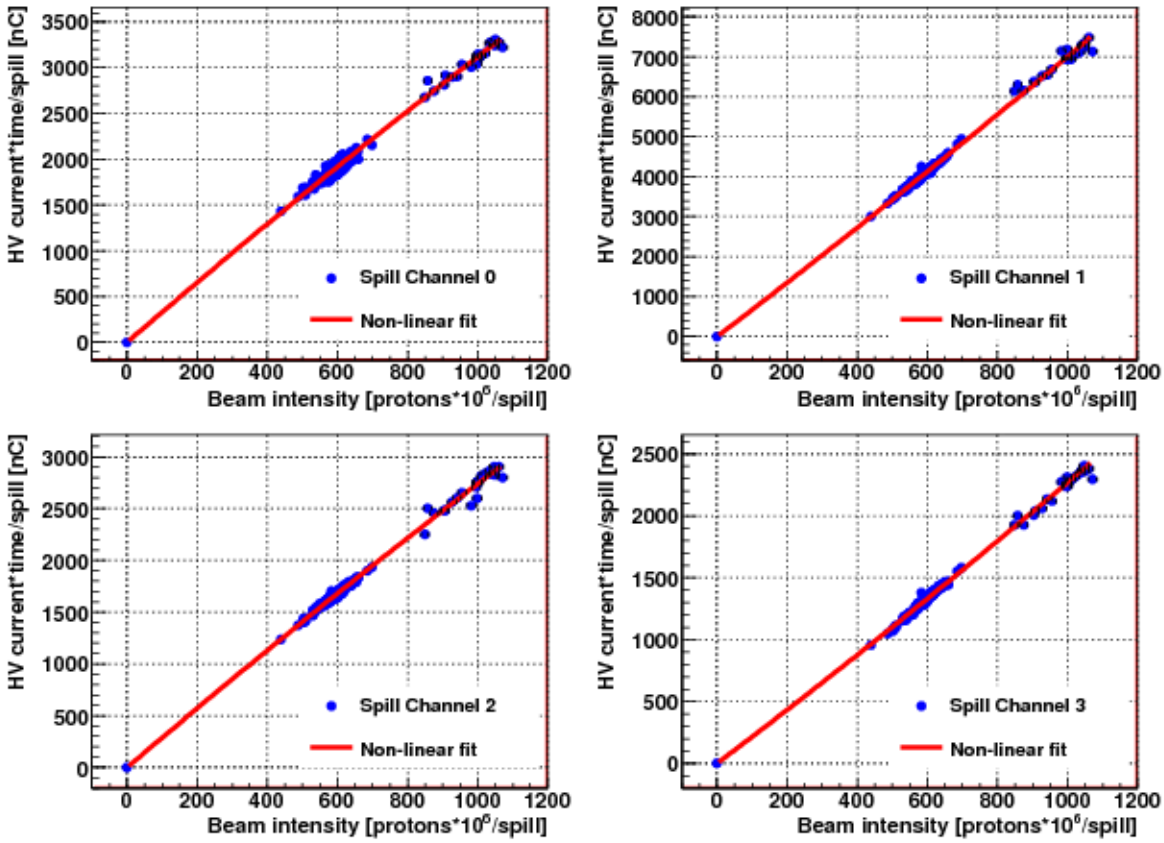

Figure 7.23: *HV current vs. beam intensity for Runs 242-244 with bad spills rejected. The fit allows a non-linear term and uses 1.25% uncertainty of the ionisation chamber data.*

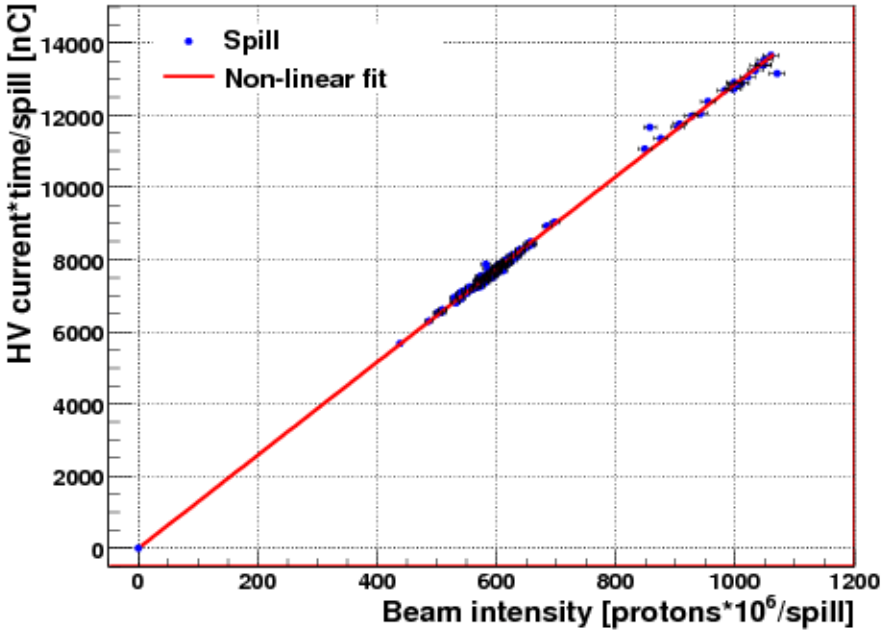

Figure 7.24: *HV current summed over channels 0-2 vs. beam intensity for the Runs 242-244 without rejected spills and with non-linear fit and 1.25% uncertainty of the ionisation chamber data.*

7.8 Results

To obtain the final result, the first period (Runs 230, 240, 241) with its large beam intensity range is considered. In addition, a 1.25% uncertainty of the ionisation chamber data instead of 5% is used based on the observation that the χ^2s of the fits become about one per degree of freedom with this smaller uncertainty. By using the summed HV current of the channels 0-2 it was possible to show that the FCAL HV current depends linearly on the beam intensity with a non-linearity of (0.26±0.05)% or less than 0.36% at 95% confidence level (CL).
The analysed data of the second period (Runs 242-244) gives a non-linearity of (0.59±0.65)% for the summed HV current of the channels 0-2. Here the uncertainty is much larger because of the smaller intensity range, but this result is consistent with the non-linearity calculated for the first period. This applies for a beam intensity of $1 \cdot 10^9$ p/spill which corresponds to the nominal ATLAS luminosity of 10^{34} cm^{-2} s^{-1}.

8 Implications for the Relative Luminosity Measurement in ATLAS

The analysis of the data taken during the April run in Protvino leads to a linear relation between the measured HV current of the FCALchick 250 µm side and the beam intensity with a non-linearity of less than 0.36 % (95% CL) at $1 \cdot 10^9$ p/spill (corresponding to the nominal ATLAS luminosity of 10^{34} cm^{-2} s^{-1}).

Nevertheless, the differences between a fixed target experiment like in the testbeam in Protvino and a collider experiment like ATLAS have to be considered. It is necessary to consider, if and how the testbeam results can be transferred to the conditions in the ATLAS experiment. First of all, it can be assumed that the measurement is in principle comparable to that in ATLAS, because the beam intensity is proportional to the luminosity in a fixed target experiment. The beam intensity was taken from the ionsiation chamber data in the analysis of Chapter 7. The offline comparison between the activated aluminium foils (as described in Chapter 6) and the ionsiation chamber data lead to the result, that the ionisation chamber data indeed depends linearly on the beam intensity up to about $2 \cdot 10^{11}$ p/spill.

The differences between the ATLAS FCAL1 and the FCALchick used as a small prototype of the FCAL1 in the Protvino testbeam have to be considered. The tubes of the FCALchick are nine times shorter than those of the FCAL1 in ATLAS and the FCALchick only consists of four channels with four tubes each as described in Chapters 4-6. This means that the main differences between the ATLAS FCAL1 and the FCALchick in Protvino are the different proportions of both calorimeter modules. In addition only one tube group of the FCALchick was connected to each HV supply channel instead of 64 tube groups in the ATLAS FCAL1. For these reasons it can be expected that the HV current per channel and for the whole calorimeter is much larger for the ATLAS FCAL1 than for the FCALchick during the Protvino testbeams.
The main conclusion of this is that the statistical fluctuations of the HV current in one HV channel of the ATLAS FCAL1 can be assumed to be even less than in Protvino and can be further reduced by summing over the HV currents of all 128 channels of both ATLAS FCAL1 modules. In addition the HV current measurement devices installed in the ATLAS FCAL1 are accurate enough for this measurement as described in Chapter 5.

For this reason only systematic effects as discussed in the note [6] and summarised in Chapter 5 could influence this luminosity measuring method in ATLAS. The effects of background currents from natural material activity as well as recombination and temperature variation effects can be assumed as already included in the testbeam result, because the FCALchick in Protvino consists of the same materials as the FCAL1 in ATLAS. In

addition, the conditions of the liquid argon (temperature of about 89 K, purity of about 2 ppm) were the same in the Protvino April run as will in ATLAS. The FCAL1 HV currents caused by detector activation could be higher than it was the case in Protvino because of the larger detector volume, but these currents can be disregarded to those due to primary interactions in ATLAS as described in Chapter 5.
The different beam structure in Protvino compared to the ATLAS experiment will not influence the luminosity measurement using the FCAL1 HV currents, because the low pass filters will cause an averaging over many bunch crossings and the only difference will consist in a continuous DC-current visible in the ATLAS experiment.
Therefore, only the systematic effects of a displacement of the mean interaction point and of lost beam particles reaching the FCAL1 could deteriorate the linear response of the FCAL1 HV currents in ATLAS. As discussed in Chapter 5 the effect of lost beam particles is negligible when taking the shielding of ATLAS into account. The HV current variations caused by a movement of the mean interaction point of 1 cm along the beam axis can be expected to be less than 0.2 % in each FCAL1 module (or less than 0.1 % for the sum of the currents of both FCAL1 modules).
Together with the obtained testbeam result of a non-linearity of less than 0.36 % (95% CL), it can be concluded that a relative luminosity measurement using the FCAL1 HV currents with a precision of better than 0.5 % is feasible, both from a statistic and a systematic point of view.
This is the non-linearity assuming the nominal ATLAS luminosity of 10^{34} cm^{-2} s^{-1} and it would be accordingly lower at lower luminosities of the LHC.

9 Conclusion and Outlook

The intention of this thesis was to study in testbeams, whether a measurement of the relative luminosity of the LHC using the HV currents of the FCAL1 in the ATLAS experiment would be feasible and what would be the precision of such a measurement.
The testbeams took place in November 2007 and April 2008 at the U-70 proton accelerator in Protvino, Russia. A small prototype of the FCAL1, the so called FCALchick, was used there. The participation in this testbeam and the data taking were planned. It was necessary to make sure that the beam intensity and the HV current of the FCALchick were measured accuratly such, that a comparison between these two quantities would be possible with the required precision. The beam intensity was measured via an ionisation chamber, which depended linearly on the beam intensity over the full intensity range. The HV current readout available in Protvino was insufficient and an additional HV current measurement device was constructed and installed in the Protvino testbeam area. In addition, a program was written for setting the readout parameters and providing an online monitoring of the HV current measurement in Protvino. The data taken during the testbeams was sufficient for a detailed comparison between the HV currents and the beam intensity.

The analysis of the data taken during the April run in Protvino shows a linear relation between the measured HV current of the FCALchick 250 µm side and the beam intensity with a non-linearity of less than 0.36 % (95% CL) at $1 \cdot 10^9$ p/spill (corresponding to the nominal ATLAS luminosity of $10^{34}\,\mathrm{cm}^{-2}\,\mathrm{s}^{-1}$). To obtain a result for the ATLAS experiment, it is necessary to include systematic uncertainties of the FCAL1 HV currents in ATLAS into the result of the testbeam-data analysis. The most important systematic uncertainty of approximately 0.1 % is caused by a displacement of the mean interaction point in ATLAS. Together with this, a precision of the relative luminosity measuring method of less than 0.5 % will be feasible in ATLAS as the result of this thesis.

In ATLAS the FCAL1 HV currents will be measured by a current measurement included in the HV supply modules and will be stored in the PVSS[1] archive.
Based on the result obtained in this thesis, an algorithm reading out the HV currents saved in the PVSS archive and transfering them to the Oracle database used for slow control and offline analysis was implemented. In addition, it is possible to calculate the sum of some HV channels or of all 128 channels within this algorithm. By comparing the HV currents of both FCAL modules it could be possible to get information about the position of the interaction point in ATLAS.
The readout cycle time for all 128 HV channels turned out to be approximately 3.5 s and

[1] Process Visualisation and Steering System

is limitted by the PVSS-to-Oracle archiving. The measured relative luminosity can be calibrated to absolute values in special dedicated runs with the ALFA[2] detector.
It is expected that the LHC will have its first collisions at the end of 2008 and that the relative luminosity measurement using the FCAL1 HV currents will be in progress, thenceforward.

[2]Absolute Luminosity For ATLAS

Appendix A Analysis of the other Runs of the April Testbeam

The Runs 230 and 240-244 are the ones with the best conditions for comparing the FCALchick HV currents with the beam intensity. The nominal voltage was applied at both FCALchick calorimeters (250 V at the 250 µm side and 100 V at the 100 µm side). In addition, the position of the cryostat was centered on the beam and kept constant during these runs. For these reasons the Runs 230 and 240-244 were analysed primarily.
To analyse the other runs of the April testbeam, the first part of the runs given in Table 6.7 were devided into periods with constant cryostat position. This table is given here again with the partition into the different periods included (see Table A.1).

Run	Beam intensity [p/spill]	Duration [min:s]	FCALchick module centered on beam	Cryostat position [mm]	Period
152	$2.0 \cdot 10^7$	12:04	100 µm side	−6	-
160	$2.0 \cdot 10^7$	20:23	100 µm side	−6	-
161-162	$2.0 \cdot 10^7$	44:19	100 µm side	0	-
166	$2.4 \cdot 10^9$	23:21	100 µm side	−6	3rd
175-178	$2.3 \cdot 10^9$	62:00	100 µm side	−6	3rd
189	$1.6 \cdot 10^{11}$	13:25	250 µm side	+40	4th
196-202	$2.0 \cdot 10^{10}$	107:00	250 µm side	+40	4th
209-210	$2.0 \cdot 10^{10}$	34:20	250 µm side	+40	4th
211-218	$2.0 \cdot 10^{10}$	80:00	100 µm side	+25	5th
219	$2.0 \cdot 10^8$	12:17	100 µm side	+25	5th
221	$2.0 \cdot 10^8$	12:09	100 µm side	+15	-
222	$2.0 \cdot 10^8$	12:27	100 µm side	+25	5th
223	$1.6 \cdot 10^8$	11:58	100 µm side	+25	5th
230	$1.3 \cdot 10^8$	12:16	250 µm side	+32.5	1st
240	$2.5 \cdot 10^9$	12:00	250 µm side	+32.5	1st
241	$5.3 \cdot 10^9$	12:07	250 µm side	+32.5	1st
242	$8.5 \cdot 10^8$	12:13	250 µm side	+32.5	2nd
243	$5.0 \cdot 10^8$	10:03	250 µm side	+32.5	2nd
244	$5.0 \cdot 10^8$	11:27	250 µm side	+32.5	2nd

Table A.1: *Runs taken in April with 250 V applied to the FCALchick 250 µm side. The partition into the different periods for analysis is shown in the last column.*

At the low beam intensities (about $2 \cdot 10^7$ p/spill) of the Runs 152 and 160-162, the HV current within the spills turned out as not high enough to separate it from the background measurements (between the spills) when the beam was not centered on the 250 µm side. The FCALchick HV current of the third, fourth and fifth period were integrated over one spill and compared with the beam intensity provided by the ionisation chamber on a spill by spill basis. This was done in the same way as described above for the first and second period and with an ionisation chamber uncertainty of 1.25 %. The plots of the HV current compared with the beam intensity of the four channels and with the summed HV current of the channels 0-2 compared with the beam intensity for the third, fourth and fifth period are given in the Figures A.1 - A.6. In addition the Figures A.7 and A.8 show the fifth period zoomed in on low beam intensities of up to $2 \cdot 10^8$ p/spill. All these plots are made with a non-linear fit function as in Equation (7.8).

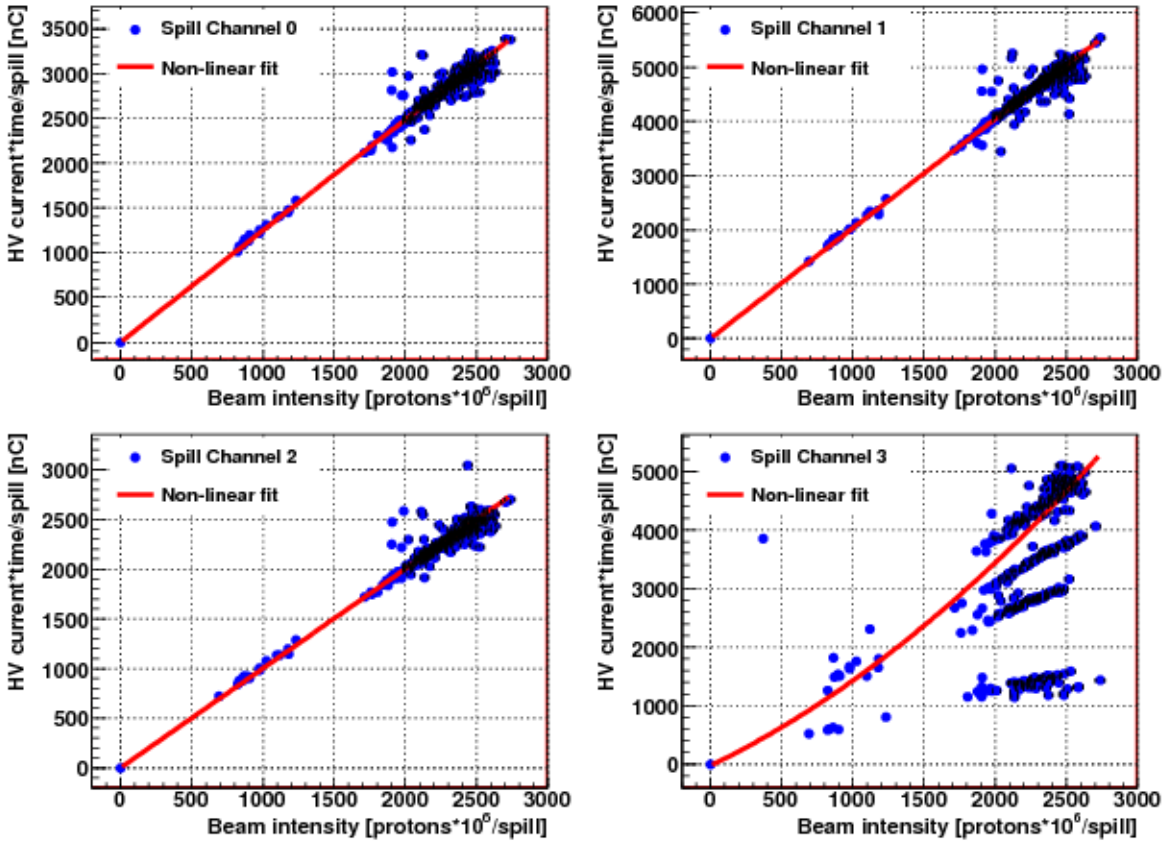

Figure A.1: *HV current vs. beam intensity for Runs 166, 175-178 with non-linear fit and 1.25% uncertainty of the ionisation chamber data.*

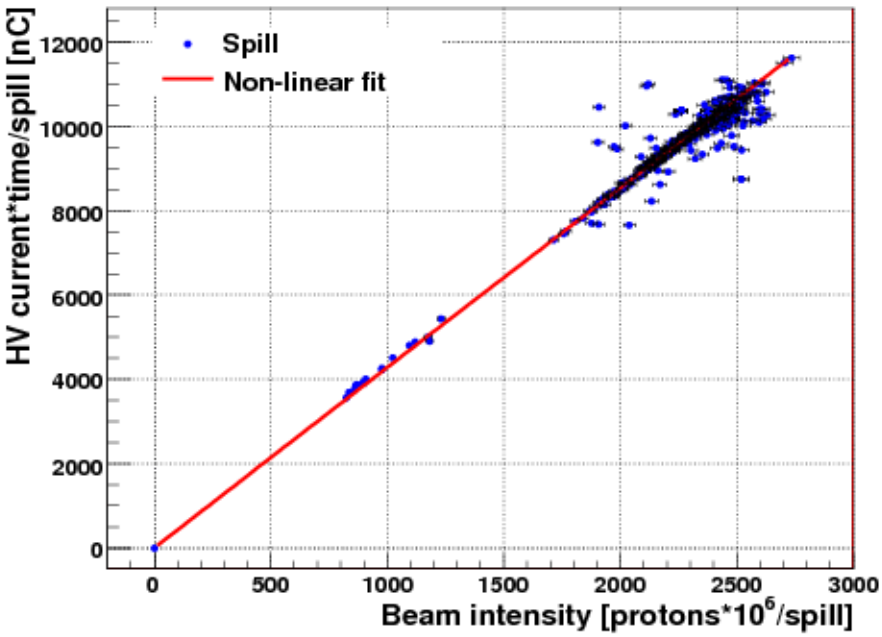

Figure A.2: *HV current summed over channels 0-2 vs. beam intensity for Runs 166, 175-178 with non-linear fit and 1.25% uncertainty of the ionisation chamber data.*

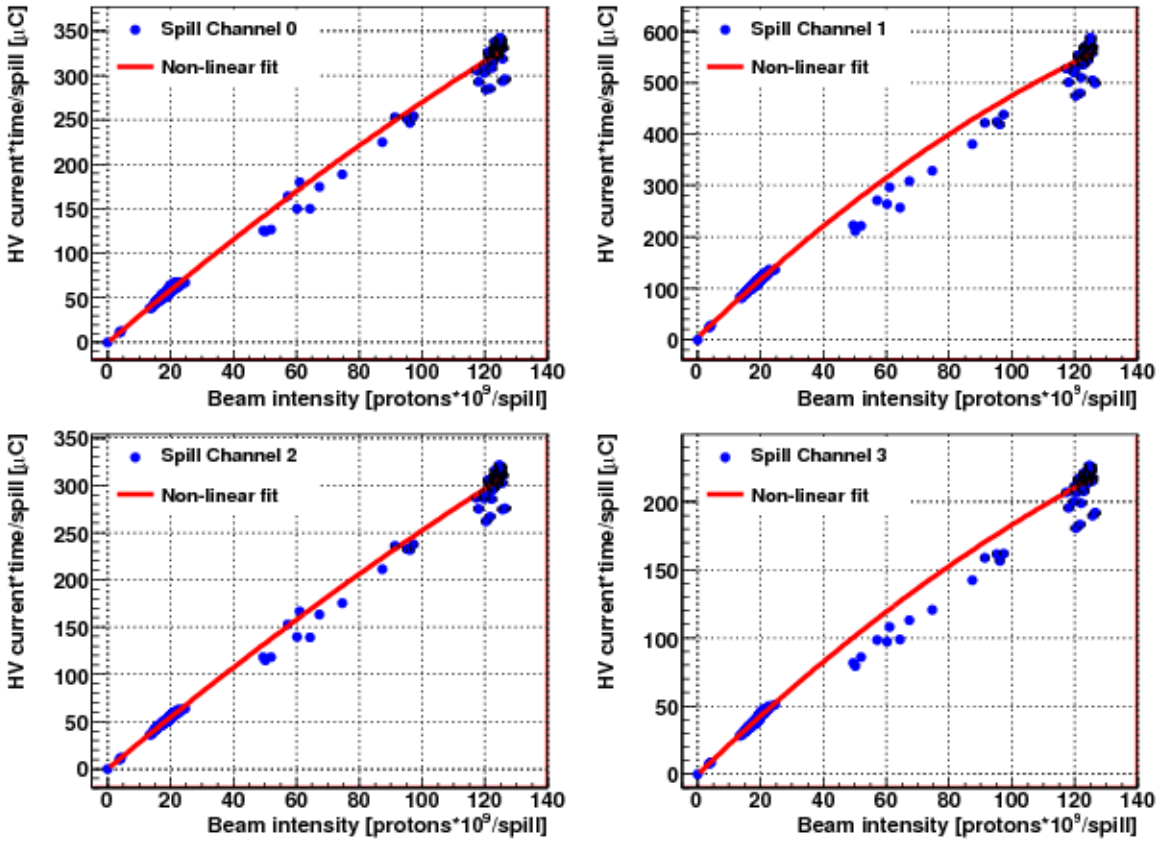

Figure A.3: *HV current vs. beam intensity for Runs 189, 196-202, 209-210 with non-linear fit and 1.25% uncertainty of the ionisation chamber data.*

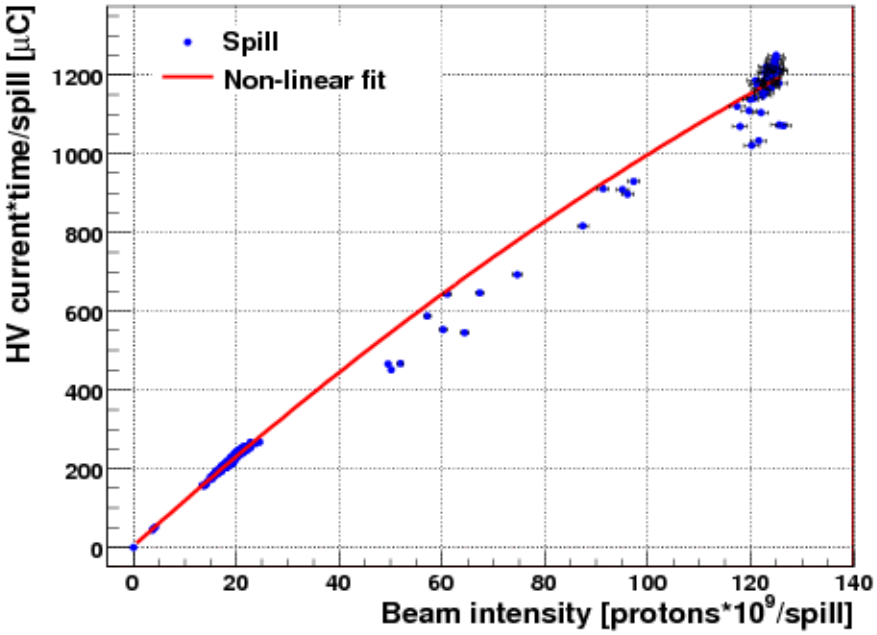

Figure A.4: *HV current summed over channels 0-2 vs. beam intensity for Runs 189, 196-202, 209-210 with non-linear fit and 1.25% uncertainty of the ionisation chamber data.*

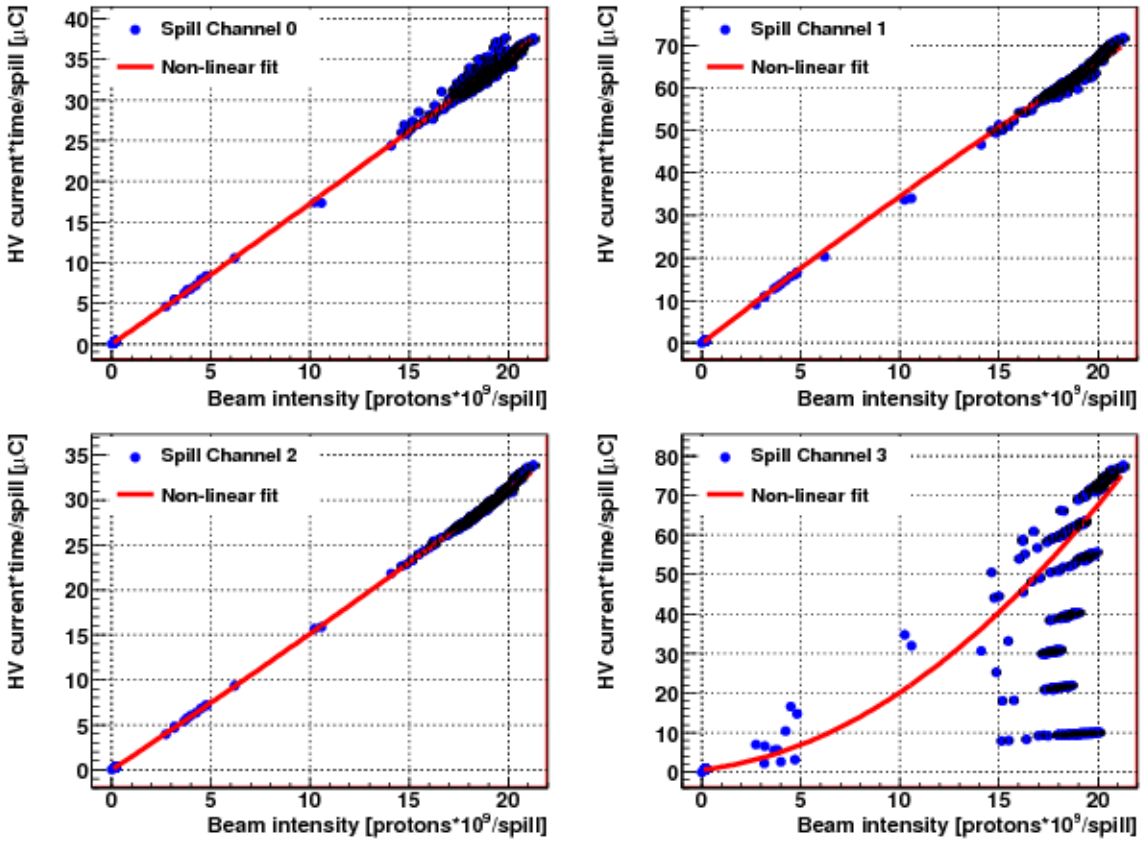

Figure A.5: *HV current vs. beam intensity for Runs 211-219, 222-223 with non-linear fit and 1.25% uncertainty of the ionisation chamber data.*

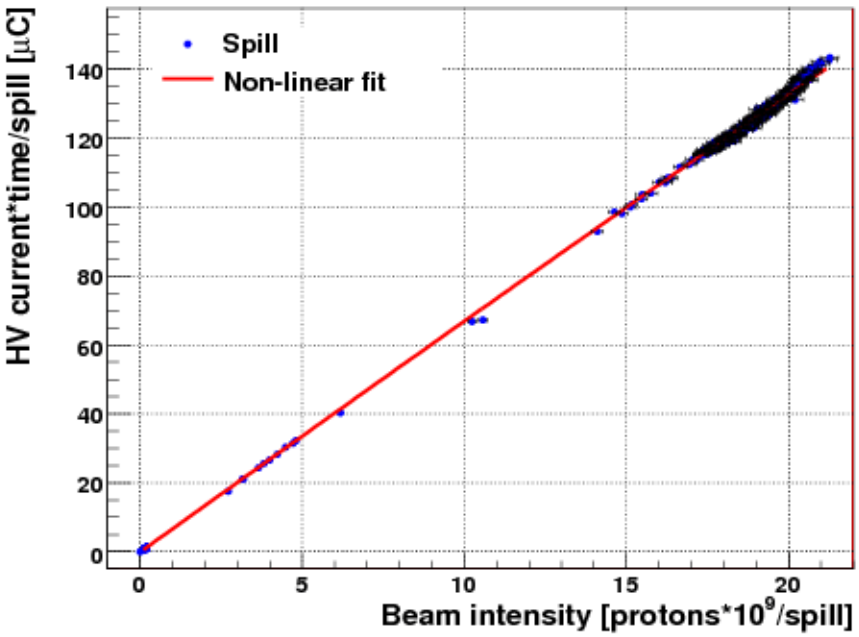

Figure A.6: *HV current summed over channels 0-2 vs. beam intensity for Runs 211-219, 222-223 with non-linear fit and 1.25% uncertainty of the ionisation chamber data.*

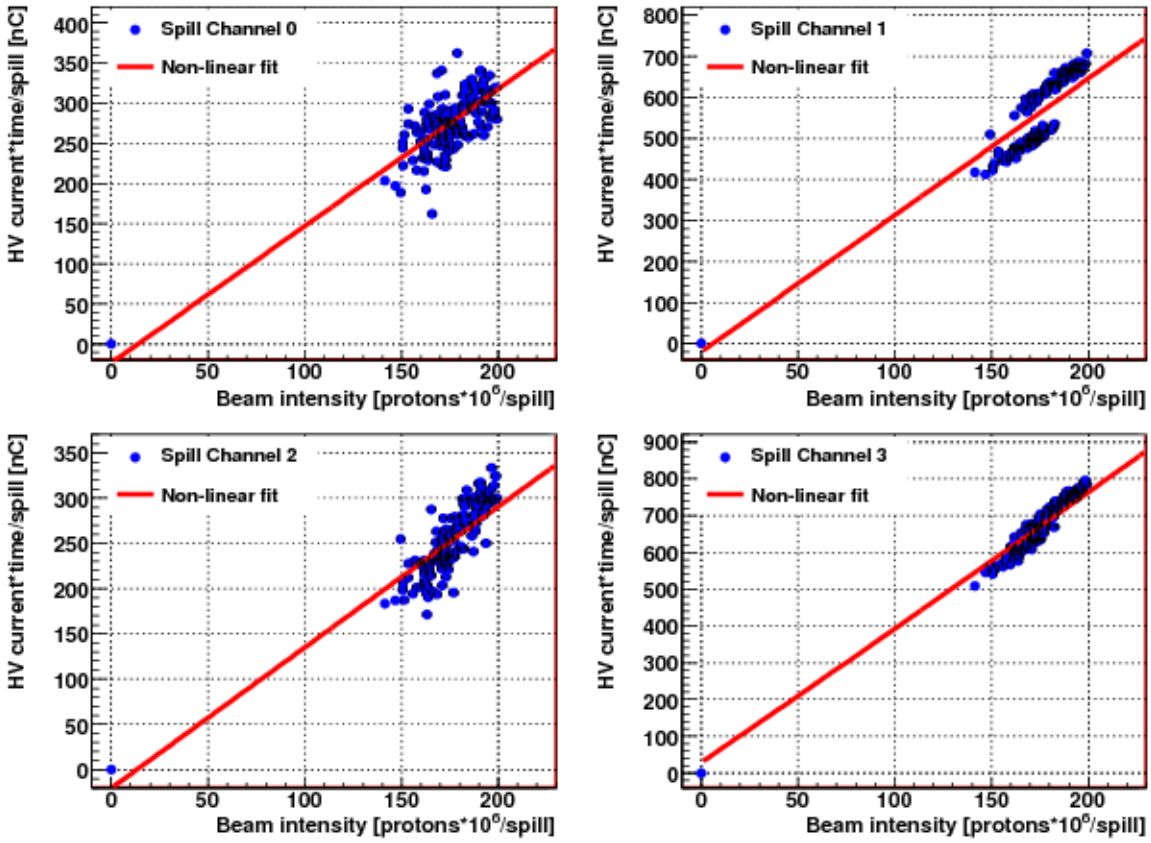

Figure A.7: *HV current vs. beam intensity zoomed in on Runs 219, 222-223 with non-linear fit and 1.25% uncertainty of the ionisation chamber data.*

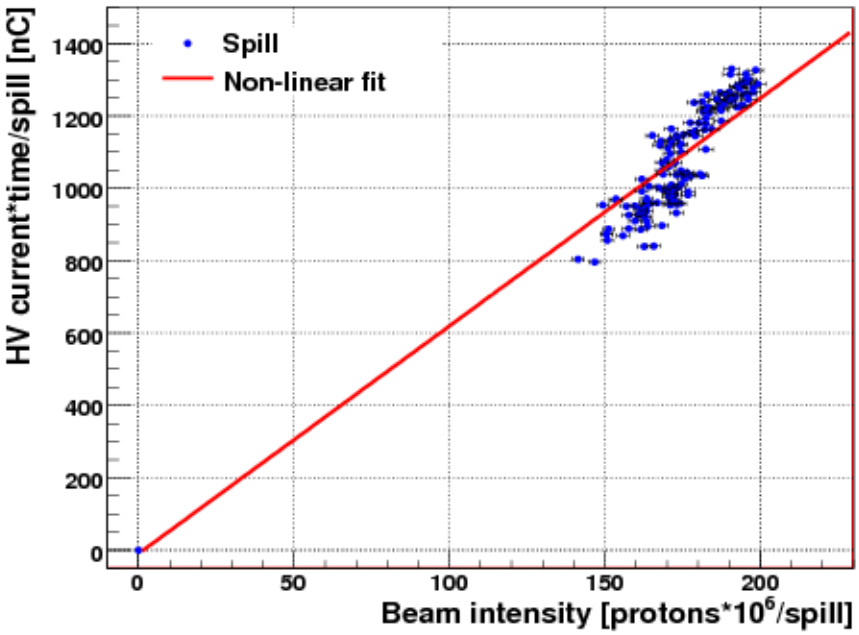

Figure A.8: *HV current summed over channels 0-2 vs. beam intensity zoomed in on Runs 219, 222-223 with non-linear fit and 1.25% uncertainty of the ionisation chamber data.*

During the third and fifth period, the voltage applied at the 100 µm side of the FCALchick was varied in the steps 10 V, 20 V, 40 V, 60 V, 80 V and 100 V. The HV current response of these voltage steps can be seen at channel 3 in the plots (the ADC of channel 3 was connected to channel 6 of the 100 µm side). For this reason these fits cannot be taken seriously. The fit parameters of the non-linear fit functions for the third, fourth and fifth period are summarised in Table A.2. Noticeable are the large χ^2s per degree of freedom with the used uncertainty on the ionisation chamber data of 1.25 %. Responsible for this are some spills located far away from the fit function (see plots). It was not possible to identify them as bad spills and to reject them using the algorithm described in Section 7.6. For this reason it had to be assumed that these spills are real measurements with such large fluctuations in the relation between the HV current and the beam intensity. For example in the fourth period at beam intensities between $4 \cdot 10^{10}$ p/spill and $1 \cdot 10^{11}$ p/spill some spills are located clearly below the fit function. In addition, channel 1 of Figure A.7 (fifth period) shows two steps in the measured HV current at nearly constant beam intensities. This could result from a small voltage drop in this channel, but it was not possible to identify a clear reason for these measurements like a beam position variation as described in Section 7.5 or something comparable.
Nevertheless, the non-linear fractions of these three periods are consistent with the first and second period at 95% confidence level, except the larger non-linear fraction of the third period. Its large uncertainty is caused by the small intensity range from $1 \cdot 10^9$ p/spill to $2.8 \cdot 10^9$ p/spill.
The third, fourth and fifth period show much larger χ^2s and are therefore less believable than the first and second period from a statistical point of view. For this reason the results of the first and second period were used to obtain the final result of this thesis.

From the fourth period at high intensities up to $1.3 \cdot 10^{11}$ p/spill it is observable that the non-linearity of the fit at the same beam intensity ($1 \cdot 10^9$ p/spill as given in the Tables 7.6 and A.2) is not increasing, when going to higher intensities. In contrast, the non-linear fraction is very small with 0.163% as well as its uncertainty of 0.002% (95% CL), because of the large intensity range. In addition, no significantly different behaviour of the FCALchick with 100 µm LAr gaps is visible from the HV current point of view, when using the data of channel 3.

Period	Channel	P_0	P_1	P_2	$\triangle P_2$
Third	0	0.18	1.26	$-0.09 \cdot 10^{-4}$	$0.03 \cdot 10^{-4}$
	1	0.37	2.04	$-0.10 \cdot 10^{-4}$	$0.01 \cdot 10^{-4}$
	2	0.52	1.00	$-0.01 \cdot 10^{-4}$	$0.02 \cdot 10^{-4}$
	3	−20.94	1.19	$2.77 \cdot 10^{-4}$	$0.02 \cdot 10^{-4}$
	Sum(0,1,2)	0.08	4.34	$-0.36 \cdot 10^{-4}$	$0.09 \cdot 10^{-4}$
Fourth	0	−0.03	3.00	$-0.31 \cdot 10^{-5}$	$0.00 \cdot 10^{-5}$
	1	0.45	5.98	$-1.00 \cdot 10^{-5}$	$0.00 \cdot 10^{-5}$
	2	0.01	2.79	$-0.27 \cdot 10^{-5}$	$0.00 \cdot 10^{-5}$
	3	−0.07	2.21	$-0.38 \cdot 10^{-5}$	$0.00 \cdot 10^{-5}$
	Sum(0,1,2)	0.02	11.94	$-1.95 \cdot 10^{-5}$	$0.01 \cdot 10^{-5}$
Fifth	0	−5.56	1.64	$0.64 \cdot 10^{-5}$	$0.03 \cdot 10^{-5}$
	1	−11.26	3.28	$0.22 \cdot 10^{-5}$	$0.04 \cdot 10^{-5}$
	2	−2.02	1.46	$0.51 \cdot 10^{-5}$	$0.03 \cdot 10^{-5}$
	3	256.1	1.83	$8.07 \cdot 10^{-5}$	$0.03 \cdot 10^{-5}$
	Sum(0,1,2)	−3.50	6.29	$1.84 \cdot 10^{-5}$	$0.07 \cdot 10^{-5}$

Period	Channel	$\chi^2(DoF)$	P_2/P_1	$(\triangle P_2)/P_1$	$P_2/P_1 \cdot 1000 \cdot$ $\cdot(p \cdot 10^6/spill)$
Third	0	2725(389)	$-0.07 \cdot 10^{-4}$	$0.02 \cdot 10^{-4}$	$0.74\% \pm 0.24\%$
	1	3276(390)	$-0.05 \cdot 10^{-4}$	$0.01 \cdot 10^{-4}$	$0.49\% \pm 0.06\%$
	2	3461(390)	$-0.01 \cdot 10^{-4}$	$0.02 \cdot 10^{-4}$	$0.15\% \pm 0.23\%$
	3	−(392)	$2.33 \cdot 10^{-4}$	$0.01 \cdot 10^{-4}$	$23.33\% \pm 0.13\%$
	Sum(0,1,2)	3030(389)	$-0.08 \cdot 10^{-4}$	$0.02 \cdot 10^{-4}$	$\mathbf{0.84\% \pm 0.20\%}$
Fourth	0	4447(511)	$-1.03 \cdot 10^{-6}$	$0.01 \cdot 10^{-6}$	$0.103\% \pm 0.001\%$
	1	8716(511)	$1.67 \cdot 10^{-6}$	$0.00 \cdot 10^{-6}$	$0.167\% \pm 0.000\%$
	2	2547(511)	$-0.96 \cdot 10^{-6}$	$0.01 \cdot 10^{-6}$	$0.096\% \pm 0.001\%$
	3	6583(511)	$-1.72 \cdot 10^{-6}$	$0.01 \cdot 10^{-6}$	$0.172\% \pm 0.001\%$
	Sum(0,1,2)	3632(511)	$-1.63 \cdot 10^{-6}$	$0.01 \cdot 10^{-6}$	$\mathbf{0.163\% \pm 0.001\%}$
Fifth	0	1681(518)	$0.39 \cdot 10^{-5}$	$0.02 \cdot 10^{-5}$	$0.39\% \pm 0.02\%$
	1	4741(520)	$0.07 \cdot 10^{-5}$	$0.01 \cdot 10^{-5}$	$0.07\% \pm 0.01\%$
	2	766(516)	$0.35 \cdot 10^{-5}$	$0.02 \cdot 10^{-5}$	$0.35\% \pm 0.02\%$
	3	−(517)	$4.41 \cdot 10^{-5}$	$0.01 \cdot 10^{-5}$	$4.41\% \pm 0.01\%$
	Sum(0,1,2)	1843(514)	$0.29 \cdot 10^{-5}$	$0.01 \cdot 10^{-5}$	$\mathbf{0.29\% \pm 0.01\%}$

Table A.2: *Fit parameters of non-linear fit for the third, fourth and fifth period with 1.25% uncertainty on ionisation chamber data.*

Bibliography

[1] Lhc beam parameters relevant for the peak luminosity . https://edms.cern.ch/file/445830/5/Vol_1_Chapter_2.pdf.

[2] Mecanismo de higgs ph . http://de.wikipedia.org/wiki/Bild:Mecanismo_de_Higgs_PH.png#filelinks.

[3] CERN ALICE. Alice technical proposal. Technical report, CDS cer-000214817, 1995.

[4] R. Barate et al. Search for the standard model Higgs boson at LEP. *Phys. Lett.*, B565:61–75, 2003.

[5] The Large Hadron Collider beauty experiment . http://lhcb.web.cern.ch/lhcb/.

[6] W Bonivento. Online luminosity monitoring with liquid argon calorimeters at atlas and d0. Technical Report ATL-LARG-2001-001, CERN, Geneva, Nov 2000. revised version number 1 submitted on 2000-12-22 10:49:45.

[7] S. S. Bulanov, V. A. Novikov, L. B. Okun, Alexandre N. Rozanov, and M. I. Vysotsky. Z lineshape versus 4th generation masses. *Phys. Atom. Nucl.*, 66:2169–2177, 2003.

[8] Peter Clarke. Z0 lineshape results from lep-1993. 1993.

[9] CMS. Cms physics technical design report: Volume 1 detector performance and software. Technical report, CERN-LHCC-2006-001, 2006.

[10] ATLAS Collaboration. Atlas liquid argon calorimeter. Technical report, CERN/LHCC 96-41, 1996.

[11] ATLAS Collaboration. Detector and physics performance. Technical report, CERN/LHC, 1999.

[12] L Davis, A Goldhaber, and M Nieto. *Phys. Rev. Lett. 35*, (1402), 1975.

[13] The ALEPH Collaboration et al. Precision electroweak measurements on the z resonance. *Phys.Rept. 427 (2006) 257*, B667(CERN-PH-EP/2005-041, SLAC-R-774).

[14] C. Amsler et al. (Particle Data Group). *Phys. Lett.*, B667, 2008.

[15] Peter W. Higgs. BROKEN SYMMETRIES AND THE MASSES OF GAUGE BOSONS. *Phys. Rev. Lett.*, 13:508–509, 1964.

[16] Peter W. Higgs. Spontaneous Symmetry Breakdown Without Massless Bosons. *Phys. Rev.*, 145:1156–1163, 1966.

[17] John Rutherfoord. LAr Endcap High Lumi Meeting . http://indico.cern.ch/getFile.py/access?contribId=16&resId=0materialId=slides&confId=11655.

[18] Michael Spira and Peter M Zerwas. Electroweak symmetry breaking and higgs physics. (hep-ph/9803257. CERN-TH-97-379. DESY-97-261):70 p, Dec 1997.

Danksagung

Zum Schluss möchte ich mich ganz herzlich bei allen bedanken, die mich während der Zeit dieser Diplomarbeit unterstützt haben. Dazu gehört natürlich die ATLAS Gruppe, in der immer eine grossartige und motivierende Atmosphäre geherrscht hat. Besonders erwähnen möchte ich dabei Andreas Ludwig, der stets ein guter Zimmergenosse war und ein offenes Ohr für meine Fragen hatte. Ausserdem danke ich Lydia Köhler, Albrecht Simon, Peter Steinbach, Markus Warsinski und Marek Schönherr für das hilfreiche Korrekturlesen der Arbeit. Natürlich hatten meine Betreuer Wolfgang Mader und Michael Kobel durch ihre permantente Unterstützung besonderen Anteil am Gelingen dieser Arbeit. Auch möchte ich dem Team aus dem Elektroniklabor Peter Eckstein, Horst Futterschneider und vor allem Andreas Glatte für ihr tolle Zusammenarbeit vor und während der Aufenthalte in Russland danken.
Zum Schluss auch vielen Dank an meine liebe Familie, die mir auch während des gesamten Studiums eine tolle Zeit ermöglicht hat.

Erklärung

Hiermit versichere ich, diese Arbeit eigenständig und ohne Hilfe anderer Hilfsmittel als die angegebenen angefertigt zu haben. Die aus fremden Quellen übernommenen Resultate sind als solche kenntlich gemacht.

Dresden, den 26.08.2008

Frank Seifert